Dissertation
submitted to the
Combined Faculty for Natural Sciences and for Mathematics
of the Ruperto-Carola University of Heidelberg, Germany
for the degree of
Doctor of Natural Sciences

presented by
Diplom Engineer-Physicist **Oleg Chkvorets**
born in Horlivka, Ukraine

Oral examination: 16.07.2008

Search for Double Beta Decay with HPGe Detectors at the Gran Sasso Underground Laboratory

Referees: **Prof. Dr. Karl-Tasso Knöpfle**

Prof. Dr. Bogdan Povh

Zusammenfassung

Der neutrinolose doppelte Betazerfall ($0\nu\beta\beta$) ist die einzige Methode, die Majoranaeigenschaft des Neutrinos nachzuweisen. Seine Zerfallsrate erlaubt es, die effektive Neutrinomasse zu bestimmen. Experimente zum neutrinolosen doppelten Betazerfall zeichnen sich durch lange Meßzeiten in unterirdischen Labors aus. Sie erfordern eine starke Reduktion der Umgebungsradioaktivität und eine hohe Langzeitstabilität. Diese Probleme stehen im Mittelpunkt der vorliegenden Arbeit, die im Zusammenhang mit den Experimenten Heidelberg-Moscow, Genius-Test-Facility und Gerda entstanden ist. Die Datennahme des Heidelberg-Moscow Experiments erstreckte sich über die Jahre 1990 bis 2003. Im Rahmen dieser Arbeit wird eine verbesserte Datenanalyse der Heidelberg-Moscow Daten präsentiert. Bei Genius-Test-Facility handelt es sich um einen Testaufbau, in dem geprüft wurde, ob nackte Germanium Detektoren in flüssigem Stickstoff betrieben werden können. Die Daten des ersten Jahres dieses Experiments werden diskutiert. Das Gerda Experiment wurde entwickelt, um die experimentelle Empfindlichkeit weiter zu verbessern, indem nackte Germanium Detektoren direkt in eine hochreine Kryoflüssigkeit eingebracht werden. Letztere dient sowohl als Kühlmedium, als auch zur Abschirmung gegen radioaktiven Untergrund. Hierzu wurde zunächst die Untergrundradioktivität am Ort des Gerda Experiments in der Halle A des Gran Sasso Untergroundlabors gemessen. Zudem wurden die angereicherten Detektoren der Experimente Heidelberg-Moscow und Igex im unterirdischen Detektorlabor der Gerda Kollaboration charakterisiert und die Langzeitstabilität eines nackten HPGe Detektors in flüssigem Argon untersucht. Dabei wurde erstmals eine untere Grenze für die Halbwertzeit des neutrinolosen doppelten Elektroneneinfangs in ^{36}Ar ermittelt: $1.85{\cdot}10^{18}$ a bei 68% statistischer Sicherheit.

Abstract

Neutrinoless double-beta ($0\nu\beta\beta$) decay is practically the only way to establish the Majorana nature of the neutrino mass and its decay rate provides a probe of an effective neutrino mass. Double beta experiments are long-running underground experiments with specific challenges concerning the background reduction and the long term stability. These problems are addressed in this work for the Heidelberg-Moscow, Genius-Test-Facility and Gerda experiments. The Heidelberg-Moscow (HdM) experiment collected data with enriched ^{76}Ge detectors from 1990 to 2003. An improved analysis of Heidelberg-Moscow data is presented, exploiting new calibration and spectral shape measurements with the HdM detectors. Genius-Test-Facility was a test-facility that verified the feasibility of using bare germanium detectors in liquid nitrogen. The first year results of this experiment are discussed. The Gerda experiment has been designed to further increase the sensitivity by operating bare germanium detectors in a high purity cryogenic liquid, which simultaneously serves as a shielding against background and as a cooling media. In the preparatory stage of Gerda, an external background gamma flux measurement was done at the experimental site in the Hall A of the Gran Sasso laboratory. The characterization of the enriched detectors from the Heidelberg-Moscow and Igex experiments was performed in the underground detector laboratory for the Gerda collaboration. Long term stability measurements of a bare HPGe detector in liquid argon were carried out. Based on these measurements, the first lower limit on the half-life of neutrinoless double electron capture of ^{36}Ar was established to be $1.85{\cdot}10^{18}$ y (68% C.L).

Contents

Chapter 1

Introduction

Existence of massive neutrinos and violation of the total lepton number will require a new physics, because the present Standard model of matter interaction assumes that neutrinos are massless and lepton number is strictly conserved. However, neutrino oscillation experiments confirm a non-vanishing neutrino mass, but without providing any information on the absolute mass scale. Neutrinoless double beta ($0\nu\beta\beta$) decay may be the most sensitive way to look for lepton number violation and to conclude the Dirac or Majorana nature of the neutrino mass, while yielding the absolute scale of the neutrino mass.

This thesis focuses on the experimental search for $0\nu\beta\beta$ decay with germanium detectors in the framework of the Heidelberg-Moscow (HdM) and Gerda (GERmanium Detectors Array) experiments. Both experiments are located in the Gran Sasso underground laboratory (LNGS) of INFN in Italy. The HdM experiment had searched for $0\nu\beta\beta$ decay using five Ge diodes enriched in ^{76}Ge. The HdM has collected data from 1990 to 2003. The HdM detectors were conventionally operated high purity germanium (HPGe) detectors enclosed in vacuum copper cryostats and cooled down via a cold finger with liquid nitrogen. A massive shield was used to reduce external gamma radiation. One of the main results presented in this thesis has lead to a further increase in the sensitivity of the HdM experiment using an improved data analysis based on investigation of detector calibration [14]. This analysis has some advantages with respect to the old procedure. The energy resolution of the sum spectrum is improved by 20%, increasing the sensitivity of the HdM experiment by up to 10%.

This thesis confirms previously obtained result [27, 24, 35, 36] that the HdM background is formed by the radioactive sources located mainly in the detectors' constructive materials: vacuum cryostats, detectors holders and electrical contacts. A significant reduction of the background is planned in the Gerda experiment [73], which will use a new technique, proposed by G. Heusser [18]. According to this novel technique, bare germanium detectors will be operated inside high purity liquid nitrogen or argon, which act both as a cooling medium and as shielding from external radiation (Fig. 1.1). Without the use of vacuum cryostats, the amount of numerous pieces of solid materials surrounding the detectors is significantly reduced. This tech-

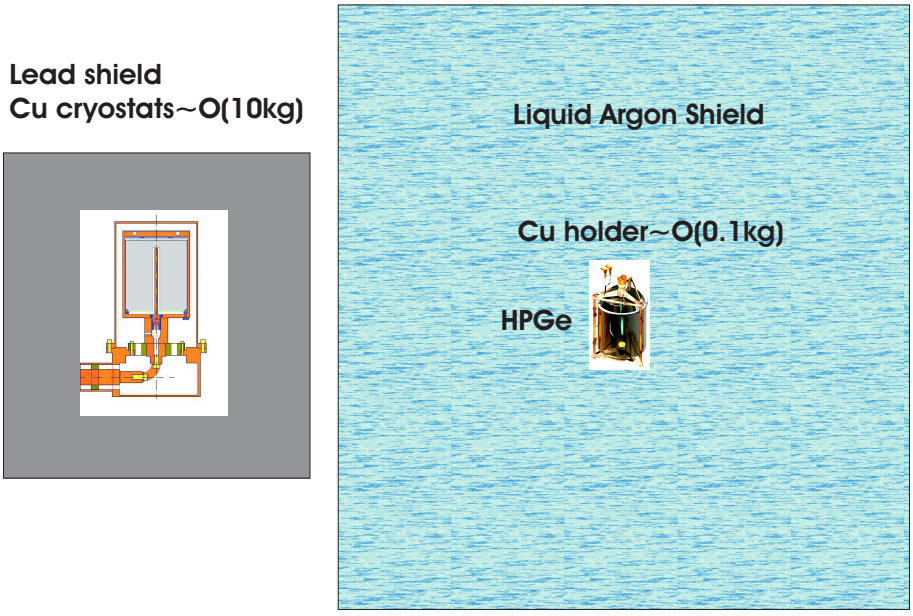

Figure 1.1: Old and new approaches for a ^{76}Ge double beta decay search.

nique was considered in the GENIUS (GErmanium in liquid NItrogen Underground Setup) and GEM proposals as well [19, 21]. A GENIUS test facility (GENIUS-TF)[20] had been commissioned at LNGS in May 2003 [52]. Four bare germanium detectors, with a total mass of about 10 kg had been operated in liquid nitrogen. During the first year of the GENIUS-TF operation, detector parameters remained stable [53], showing principal feasibility of the technique.
The following is an outline of this thesis. Chapter 2 presents an introduction to $0\nu\beta\beta$ decay and its potential. Also, the principle of detecting rare events like the $0\nu\beta\beta$ decay using HPGe detectors is discussed. Chapter 3 introduces the setup of the HdM experiment, its technical parameters and the details of calibration and data analysis. The improved analysis was used to evaluate the final HdM data set. The recent claim about $0\nu\beta\beta$ decay observation by H. V. Klapdor-Kleingrothaus et al. [14, 15] is reviewed in Chapter 4, exploiting new spectral shape measurements with the HdM detectors. In Chapter 5, the GENIUS-TF setup is described. The operation of bare HPGe detectors during the first year of measurements is summarized. In addition, the radon background sources and methods to suppress it are discussed. The measurements of the external gamma background on the GERDA experimental site in Hall A of LNGS are presented in Chapter 6. Chapter 7 describes characterization of the enriched detectors performed in the underground GERDA Detector Laboratory (GDL) at LNGS after the end of the HdM and IGEX experiments. The performance of these detectors before refurbishment for GERDA is given. Chapter 8 illustrates the operation of a bare HPGe germanium detector in the GDL test setup. Long term stability measurements of the HPGe detector with ^{60}Co were performed. The background measured for 10 days was used to derive a half-life limit for the

radiative neutrinoless double electron capture in ^{36}Ar isotope naturally occurring in liquid argon. For the first time the limit on the half-life of radiative neutrinoless double electron capture ($0\nu 2EC$) decay of ^{36}Ar was obtained.
This work has been carried out by the author in a four year period, during which the author was involved in the operation and analysis of the HEIDELBERG-MOSCOW, HDMS and GENIUS-TF experiments, and in preparatory experimental studies for the GERDA experiment for the Max-Planck-Institut für Kernphysik.

Chapter 2

Neutrinoless Double Beta Decay

2.1 Lepton number violation and the Majorana neutrino

Lepton number violation, which is the case if neutrinos are Majorana particles, creates a possibility to explain the excess of the matter over antimatter, thus explaining the overwhelming dominance of matter in the Universe. In a standard model of particle physics, neutrinos are strictly massless, the neutrinos and antineutrinos are different particles and the lepton number is conserved [1]. Experimental evidence states that the neutrino has a non-zero mass, as deduced from the neutrino flavor oscillations observed in atmospheric-SuperKamiokande, reactor-KamLAND and solar neutrino-GALLEX/GNO-SAGE-SNO experiments (For review see e.g.[3]). Neutrino oscillation experiments determine the mass squared differences but not the absolute mass. The nuclear neutrinoless double beta decay ($0\nu\beta\beta$) is a lepton number violating process (A, Z) $\rightarrow$ (A, Z+2) + $2e^-$. It can only exists if the neutrino is a massive Majorana ($\nu \equiv \bar{\nu}$) particle. For the non-standard $0\nu\beta\beta$ process to happen, the emitted neutrino in the first neutron decay must equal to its antineutrino and match the helicity of the neutrino absorbed by the second neutron (Fig. 2.1(a)).

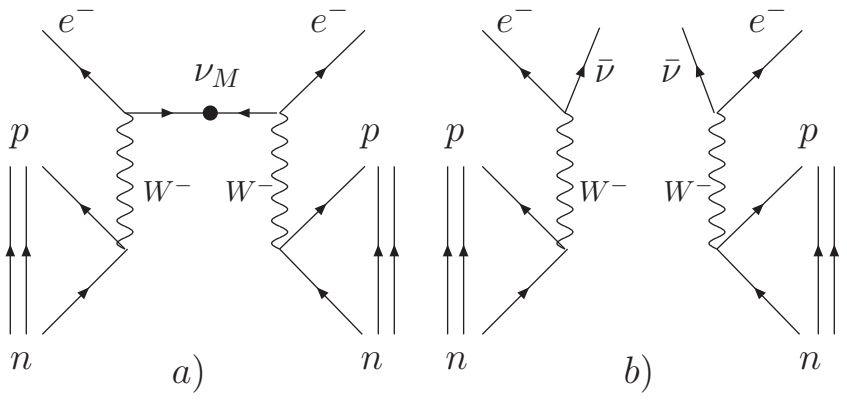

Figure 2.1: Feynman diagrams of neutrinoless (a) and two-neutrino (b) double beta decay.

The Standard Model allowed the two neutrino double beta decay ($2\nu\beta\beta$), (A, Z) $\rightarrow$ (A, Z+2) + $2e^-$ + $2\bar{\nu}$ (Fig. 2.1(b)) is a second order effect of weak interaction in the nucleus and was observed for many nuclei. The Schechter-Valle theorem [17] shows that in any gauge theory, whatever mechanism is responsible for the neutrinoless double beta decay, a massive Majorana neutrino is required. The neutrinoless decay half-life (assuming the light ν exchange mechanism) is expressed as [2]:

$$(T^{0\nu}_{1/2})^{-1} = G_{0\nu} \mid M^{0\nu} \mid^2 \langle m_\nu \rangle^2 \tag{2.1}$$

where, $M^{0\nu}$ is the nuclear matrix-element, $M^{0\nu} = M^{0\nu}_{GT} - (g_V/g_A)^2\, M^{0\nu}_F$, with $M^{0\nu}_{GT,F}$ the corresponding Gamow-Teller and Fermi contributions, $M^{0\nu}$ is in the range 3.3-5.7 [38], and $G_{0\nu}$ is an integrated kinematic factor $G_{0\nu} = 2.44 \cdot 10^{-26}[1/y]$ [2] for $0\nu\beta\beta$ decay of ^{76}Ge. The quantity $\langle m_\nu \rangle = \Sigma_j \lambda_j m_j U^2_{ej}$ is the effective neutrino mass parameter, where U_{ej} is a unitary matrix describing the mixing of neutrino mass eigenstates to electron neutrinos, λ_j a CP phase factor, and m_j the neutrino mass eigenvalue. The effective Majorana neutrino mass is than expressed as a function of the half-life of the ^{76}Ge $0\nu\beta\beta$ decay as:

$$\langle m_\nu \rangle = \frac{6.4 \cdot 10^{12}}{\mid M^{0\nu} \mid \cdot \sqrt{T^{0\nu}_{1/2}[y]}}[eV]. \tag{2.2}$$

The discovery of a $0\nu\beta\beta$ decay will tell that the Majorana neutrino has a mass equal or larger than $\langle m_\nu \rangle$. On the contrary, when only a lower limit of the half-life is obtained, one gets only an upper bound on $\langle m_\nu \rangle$, but not an upper bound on the mass of any neutrino. In fact, $\langle m_\nu \rangle_{exp}$ can be much smaller than the actual neutrino masses. The $\langle m_\nu \rangle$ bounds crucially depend on the nuclear model used to compute the $0\nu\beta\beta$ matrix element.

2.2 Search for double beta decay with Germanium detectors

Double beta decay of ^{76}Ge,

$$^{76}\mathrm{Ge} \rightarrow ^{76}\mathrm{Se} + 2\mathrm{e}^-(+2\bar{\nu}_\mathrm{e}), \tag{2.3}$$

bypassing ^{76}As is possible because the pairing energy makes a nucleus with an even number of neutrons and protons more tightly bound than its odd-odd neighbor ^{76}As (Fig. 2.2). Because double beta decay is the most rare process known, its experimental investigation requires a large amount of emitters and low-background detectors with capability of selecting the signal from the background reliably. Ge detectors provide excellent energy resolution, so the peak at the $Q_{\beta\beta}$ value at 2039 keV expected for $0\nu\beta\beta$ decay could be seen with a full width at half maximum (FWHM) of about 3 keV. This helps considerably in reducing background counts in a region

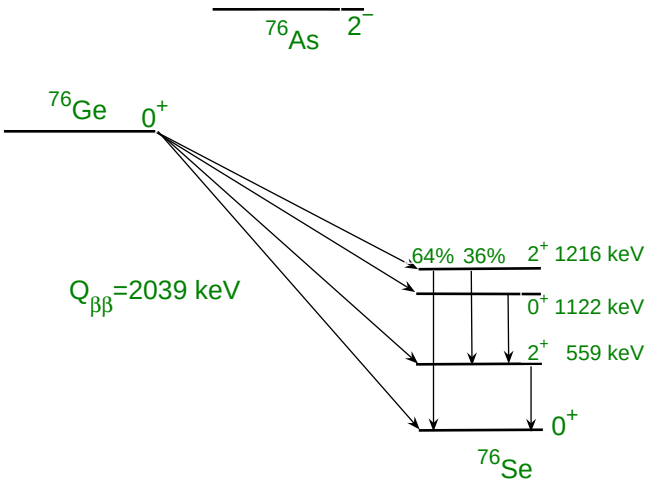

Figure 2.2: Lowest energy levels of isobar triplet A=76 with double beta decay of ^{76}Ge [28].

of interest around $Q_{\beta\beta}$. The material for HPGe detector production is supposed to be of highest purity (impurity level as low as $\sim 10^9$ atoms/cm^3). Germanium double beta decay experiments start with the cleanest source of double beta emitter material, which is also used as a detector at the same time. The experimental signatures of the $0\nu\beta\beta$ decay to the ground state is a peak at the $Q_{\beta\beta}$ value in the two-electron summed energy spectrum and a continuous $2\nu\beta\beta$ spectrum (Fig. 2.3). The $0\nu\beta\beta$ decay to the excited states of the ^{76}Se is suppressed by the kinematic phase space factor, which depends on the $Q_{\beta\beta}$ value as $\sim Q^5$. Despite such characteristic signal, the rarity of the process makes their identification very difficult. Probable signals have to be disentangled from background due to natural radioactivity, cosmogenic-induced activity and anthropogenic radioactivity, which deposit energy in the $0\nu\beta\beta$ region. The general approach followed to perform a $0\nu\beta\beta$ decay experiment is dictated by the expression of half-life:

$$T_{1/2} = ln2 \cdot \varepsilon_E \cdot \frac{N \cdot t}{S} \tag{2.4}$$

where ε_E is the detector efficiency, N is the number of decaying nuclei and S is the number of recorded peak counts during time t (or the upper limit of peak counts consistent with the observed background). In the case when S is the 1σ background fluctuation and the detector is made of the $\beta\beta$ source, the $0\nu\beta\beta$ decay experiment sensitivity at 68% C.L. can be derived from Eq. 2.4 using:

$$N = N_A \cdot \frac{a \cdot M}{A},$$

$$S = \sqrt{\Delta E \cdot B \cdot M \cdot t},$$

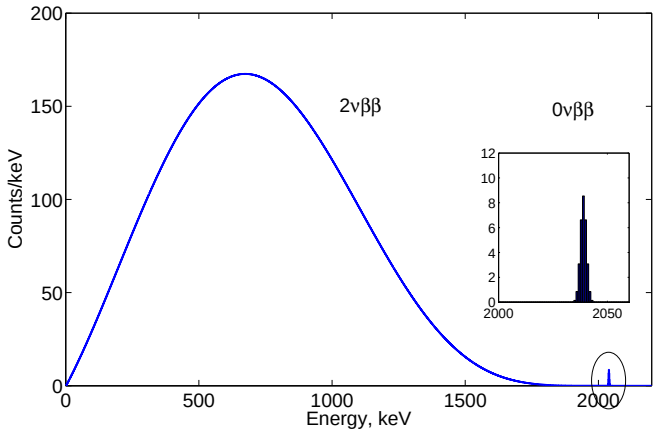

Figure 2.3: A calculated two-electron summed energy spectrum of double beta decay of ^{76}Ge to ground state. Number of counts in the continuous spectrum corresponds to $2\nu\beta\beta$ decay of ^{76}Ge with a half-life $T^{2\nu}_{1/2} = 1.7 \cdot 10^{21}$ y. The peak at Q-value corresponds to $0\nu\beta\beta$ decay with a half-life $T^{0\nu}_{1/2} = 1.2 \cdot 10^{25}$ y. The exposure is 72 kg y. A $0\nu\beta\beta$ peak in the inset has a typical resolution for HPGe detectors (3 keV FWHM at 2 MeV).

$$T^{0\nu}_{1/2}\,[y] \quad = \quad 4.17 \cdot 10^{26} \times \frac{\varepsilon_E \cdot a}{A}\sqrt{\frac{M \cdot t}{\Delta E \cdot B}}, \tag{2.5}$$

where $B\,[\mathrm{keV\,kg\,y}]^{-1}$ is the background index, M [kg] is the active mass of $\beta\beta$ emitters, N_A is the Avogadro number, $\Delta E\,[\mathrm{keV}]$ is the energy window around $Q_{\beta\beta}$ ($\Delta E = 3\sigma$), $t\,[\mathrm{y}]$ is the live-time of the measurement, a and $A\,[\mathrm{g/mol}]$ are respectively the isotopic abundance and the atomic mass of the isotope.

The use of germanium as both the source and detector of double beta decay has been suggested almost forty years ago by the Milan group, which has also carried out the first experiments [5]. Many experiments were performed since the first attempt with a consistently increased sensitivity, as summarized in Table 2.1. A major progress had been achieved in the ITEP-YePI experiment [13], which used germanium detectors enriched in ^{76}Ge for the first time. Two experiments had been operated recently to look for the $0\nu\beta\beta$ decay of ^{76}Ge, the IGEX and the HdM experiments. The IGEX Collaboration [16] operated a set of three detectors with a total mass of 6.3 kg in the Canfranc Underground Laboratory, Spain. The HdM Collaboration [25] used a set of five detectors with a total mass 11.5 kg at LNGS, Italy. Both experiments were designed to get the highest possible sensitivity (Eq. 2.5) to look for the $0\nu\beta\beta$ decay of the ^{76}Ge using a large amount of isotope, good energy resolution detectors and very low radioactive background conditions. In the next Chapter the HdM experiment is described in detail.

Experiment	Detector Type	^{76}Ge %	Exposure kg y	Background $[\mathrm{keV\,kg\,y}]^{-1}$	Sensitivity $T^{0\nu}_{1/2}$ [y] (68% C.L)	Ref.
Milan (1967)	Ge(Li)	7.8	0.0073	10^3	$3 \cdot 10^{20}$	[5]
S. Carolina-PNL (1983)	HPGe	7.8	0.3	108	$1.16 \cdot 10^{23}$	[6]
Guelf-Queens-Aptec (1984)	HPGe	7.8	0.2	39	$3.2 \cdot 10^{22}$	[7]
Milan (1984)	Ge(Li)	7.8	1.5	17	$1.2 \cdot 10^{23}$	[8]
Osaka (1986)	HPGe	7.8	0.28	6.0	$4.6 \cdot 10^{22}$	[9]
UCSB-LBL (1987)	HPGe	7.8	22.6	1.2	$2.2 \cdot 10^{24}$	[10]
Caltech-PSI-Neuchatel (1989)	HPGe	7.8	3.9	2.5	$2.7 \cdot 10^{23}$	[11]
Zaragoza-INPN-Bordeaux (1990)	HPGe	7.8	1.6	28	$4.8 \cdot 10^{22}$	[12]
ITEP-YePI (1991)	Ge(Li)	85	1.6	2.5	$1.8 \cdot 10^{24}$	[13]
IGEX (1999)	HPGe	86	10.1 (4.6 PSD*)	0.16 0.06	$1.6 \cdot 10^{25}$ $1.8 \cdot 10^{25}$	[16]
Heidelberg-Moscow (2003)	HPGe	86	71.7 (51.4 PSD)	0.17 0.07	$4.6 \cdot 10^{25}$ $6.1 \cdot 10^{25}$	[14]

Table 2.1: Experiments for search of neutrinoless double beta $0\nu\beta\beta$ decay with germanium detectors and their sensitivities for $0\nu\beta\beta$ decay. (*PSD-Pulse Shape Discrimination).

Chapter 3

Improved Analysis of the Data from the Heidelberg-Moscow (HdM) Experiment

The HdM experiment was proposed in 1987 [23] to look for neutrinoless double beta decay of ^{76}Ge at the Gran Sasso Underground Laboratory at LNGS. The experiment collected data from 1990 to 2003. In 2002 and 2004, evidence of neutrinoless double beta decay of ^{76}Ge was claimed by Klapdor-Kleingrothaus et al. [14, 15]. This chapter gives an overview of the experiment and describes the improved data analysis, which has led to an enhanced sensitivity of the experiment and subsequent publications [14, 15]. *A posteriori* analysis of the background is given in the next chapter.

3.1 HdM experiment overview

The experiment was carried out with five high-purity p-type germanium detectors enriched in the isotope ^{76}Ge to ∼86% [25]. The total active mass was 10.96 kg, resulting in a ^{76}Ge source strength of 125 mol. The HdM detectors were the first enriched high-purity Ge detectors ever produced. The energy resolution of the Ge detectors was ∼3 keV in the region of interest around the $Q_{\beta\beta}$ value, which assures zero background in the $0\nu\beta\beta$ line from the $2\nu\beta\beta$ decay. The $Q_{\beta\beta}$ value (2039.006±0.050 keV) has been determined recently with high precision [22]. The detection efficiency of Ge detectors for the $0\nu\beta\beta$ decay events was calculated to be 95%. The background index was 0.17 counts/kg y keV in the $0\nu\beta\beta$ decay region for the total exposure of 71.7 kg y.

3.2 HdM setup

The technical parameters of all the HdM detectors are given in Table 3.1. The degree of enrichment (86-88%) was verified by investigation of pieces of Ge after

Detector	Total Mass(*), [g]	Active Mass, [g]	Enrichment in ^{76}Ge, [%]
ANG1	968.7	920	85.9 ± 1.3
ANG2	2878.3	2758	86.6 ± 2.5
ANG3	2446.5	2324	88.3 ± 2.6
ANG4	2401.2	2295	86.3 ± 1.3
ANG5	2782.1	2666	85.6 ± 1.3

Table 3.1: Masses and enrichments of the five enriched ^{76}Ge detectors [25]. (*) The actual masses of the detectors were measured after dismounting from their cryostats in 2006.

crystal production using a mass spectrometer at MPI-K [29]. The experimental setup is shown in Figure 3.1. All detectors, except ANG4, were operated in a

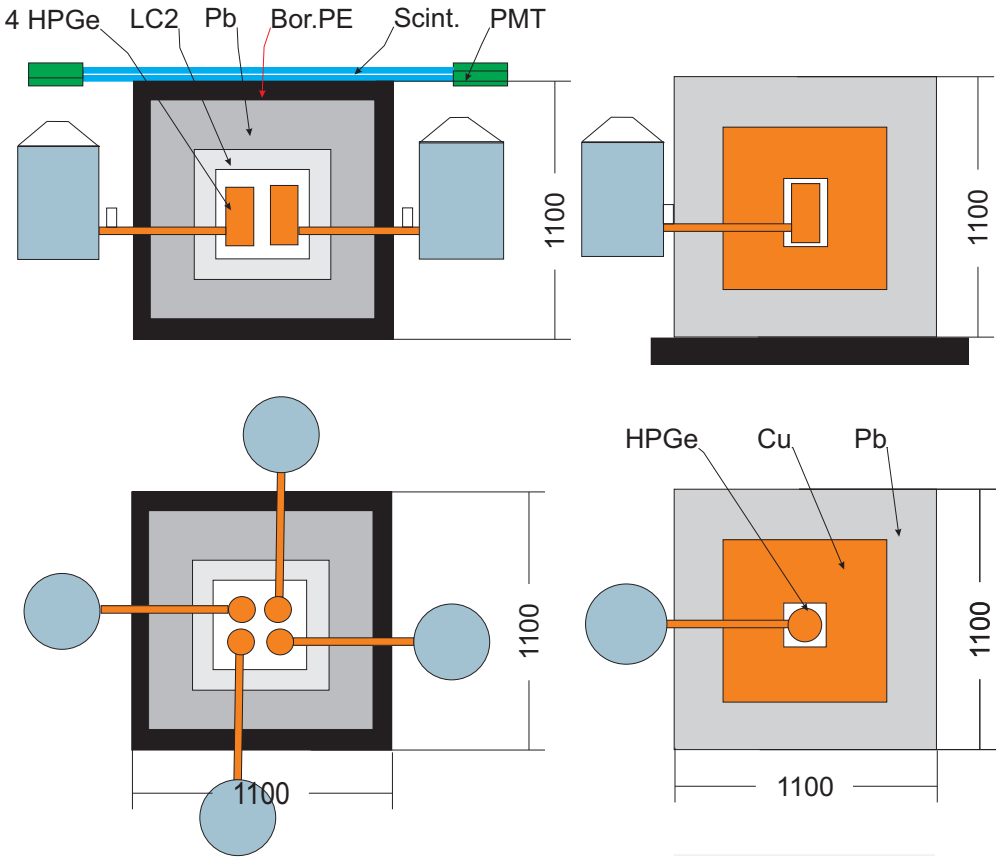

Figure 3.1: Schematic drawings of the HdM experiment setup. Four enriched detectors, ANG1, ANG2, ANG3 and ANG5, are installed in a common shield (left panel). ANG4 detector is installed in a separate shield made of electrolytic copper and lead (right panel).

common lead shield, which consisted of an inner 10 cm thick layer of low-activity LC2-grade lead followed by 20 cm of Boliden lead. The lead shield was enclosed in a

steel box, which was surrounded by 10 cm of boron-loaded polyethylene shielding to decrease the neutron flux from outside. Since 1995, an active anticoincidence muon veto was placed on top of the setup. Detector ANG4 was installed in a separate setup, which had an inner shielding of 27.5 cm electrolytic Cu and 20 cm of lead. The shield was enclosed in a steel box with a plate of boron-loaded polyethylene shielding below. No muon veto was implemented for this detector. The two setups were flushed with nitrogen in order to suppress the ^{222}Rn contamination. The setup was kept hermetically closed since February 1995. Before this time the shielding of the experiment was opened several times to add new detectors. Since November 1995, the data was acquired using a CAMAC system and a CETIA processor in event by event mode. The energy spectra from the preamplifiers (model 2002C) were recorded with 13 bit ADCs developed at MPI-K Heidelberg. The spectra from each detector were recorded in parallel using two ADCs with 8192 channels each, one ranging from the threshold up to about 3 MeV, and another one up to about 8 MeV. The timing signals from the preamplifiers of all detectors, except ANG1, were differentiated by ORTEC's Timing Filter Amplifiers (models TFA 474 and 579) and the pulse shapes were recorded with 250 MHz flash ADCs of type Analog Devices 9038 JE (in DL515 modules), with 8 bit resolution [34]. In the event by event mode, the event time, the high voltage applied on the detectors, the temperature in the detector cave, the computer room and the electronics crate, the information from the muon shield and the status of the DAQ were recorded. In addition, an operator was daily checking the high voltage of the detectors, the temperature, the nitrogen flow flushing the detector boxes, the muon anticoincidence signal, the leakage current of the detectors and the trigger rates.

3.3 Development of the experiment

For each detector, the exposure and the background index during the full live time of the experiment, divided into two periods, are presented in Table 3.2. From 1990

Detector	Live Time and Exposure				Date	Background	Pulse shape
	of all data		accepted for analysis		Start End	[counts/ [keV y kg] 2000 - 2100 [keV]	recording
	[days]	[kg d]	[days]	[kg d]			
ANG1	1237.0	1138.04	930.9	856.43	8/90 - 8/95	0.31	no
ANG2	1070.0	2951.06	997.2	2750.28	9/91 - 8/95	0.21	no
ANG3	834.7	1939.84	753.1	1750.20	9/92 - 8/95	0.20	no
ANG4	147.6	338.74	61.0	139.99	1/95 - 8/95	0.43	no
ANG5	48.0	127.97	-	-	12/94 - 8/95	0.23	no
After summing of all 5 detectors over period 1990 - 1995: Accepted exposure = **15.05 kg y**							
Full Setup, over period 1995 - 2003: Four detectors in common shielding, ANG4 detector separate							
ANG1	2123.90	1967.25	2090.61	1923.36	11/95 - 5/03	0.20	no
ANG2	1953.65	5427.94	1894.11	5223.96	11/95 - 5/03	0.11	yes
ANG3	2120.22	4960.83	2079.46	4832.67	11/95 - 5/03	0.17	yes
ANG4	2123.90	4907.44	1384.69	3177.86	11/95 - 5/03	0.21	yes
ANG5	2110.66	5665.46	2076.34	5535.52	11/95 - 5/03	0.17	yes
After summing of all 5 detectors over period 1995 - 2003 Accepted exposure = **56.655 kg y** Total exposure = **71.71 kgy**							

Table 3.2: Exposure and background index for the enriched detectors of the HEIDELBERG-MOSCOW experiment for the period from 1990 to 2003 [14]. The live time and exposure accepted for analysis are calculated according to Table 3.4.

to 1995 the setup was opened several times for installation of new detectors. A muon veto was not implemented and no individual event information was recorded.

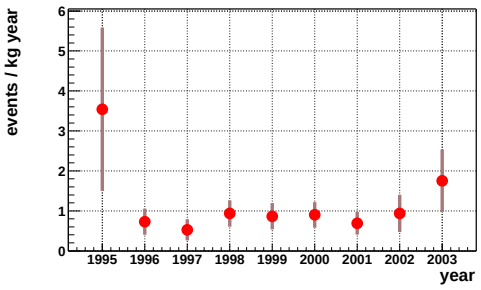

Figure 3.2: The time distribution of all events in the energy interval from 2036.5 to 2041.0 keV, for the period from November 1995 to May 2003 [15].

The time dependence of the measured rate of the energy interval from 2036.5 to 2041.0 keV is shown in Fig. 3.2. The arrival-time distribution of the events was analyzed. Figure 3.3 shows the arrival-time distribution of all events observed in the energy interval (2035.5 - 2042.5) keV as a function of time. The events distribution is consistent with a uniform one, according to the Kolmogorov-Smirnov distribution test. It demonstrates that the arrival-time distribution is not affected by technical operations during the measurement, such as the calibration procedure (introducing the thorium source into the detector chamber through a thin tube), refilling of liquid nitrogen, etc.

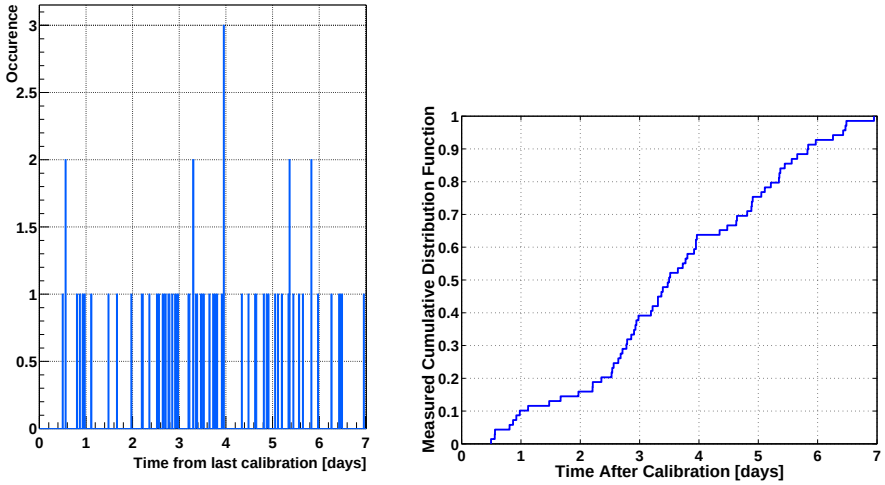

Figure 3.3: Left: arrival time for all 70 events in the interval 2035.5 - 2042.5 keV as function of time relative to the last time of calibration for the period 1995 - 2003. The acquisition was turned off during the first six hours after each calibration for a liquid nitrogen filling. The corresponding cumulative distribution (right) is consistent with a uniform one at 87% C.L., according to the Kolmogorov-Smirnov test [14].

3.4 Energy calibration

A precise energy calibration of all detectors, before summing the individual runs and summing the spectra of all detectors, is important in order to achieve a good final energy resolution, and therefore an optimal sensitivity.

3.4.1 Calibration procedure

To control the energy scale stability of the experiment, calibrations were performed weekly with a ^{228}Th (110 kBq in 2001) source for the detectors ANG1,2,3,5 and with ^{152}Eu (10 kBq) + ^{228}Th (7 kBq in 2001) sources for ANG4. The sources were mounted on steel wires and were inserted into the setup approximately 15 cm away from the detectors trough teflon tubes. The calibrations lasted 15 minutes for the four detectors setup and 45 minutes for the ANG4 setup. Only energy spectra were collected during the calibration, no individual event information was recorded.

3.4.2 Method of energy calibration

After completion of the experiment, the linearity of the electronics of the HdM detectors was studied with a ^{226}Ra source. It was observed that the integral nonlinearity is not negligible. Figure 3.4 presents the residual from a linear energy calibration with the ^{226}Ra source as a function of energy for each detector. Figure 3.5 presents the energy resolution (FWHM) as a function of energy of the γ-peaks measured with a ^{226}Ra and a ^{232}Th source. The fact that ^{228}Th does not have many spectral lines and that the electronics are not linear limit the energy calibration accuracy in the range of interest around the $Q_{\beta\beta}$ value. There are only two peaks in the ^{228}Th spectrum above 2000 keV, the γ-line at 2614.5 keV and its single escape peak at 2103.5 keV. The next line is at 1620 keV, which is too far to make proper correction for linearity. In order to minimize the errors introduced by the nonlinearity, the low and the high energy parts of the spectra were calibrated separately. For the energy above 1640 keV, the ^{228}Th lines at 2103.5 and 2614.5 keV were used. For the low-energy part of the spectra, the ^{228}Th lines at 583 and 1620 keV were chosen. The combination of these linear calibrations successfully reproduced the energies of other known lines in the spectrum. In order to check this calibration method, the individual calibration spectra were relocated to the same energy scale before being summed. The relocation method is explained in detail at the end of this section. The peak positions and energy resolution of the 2103.5 and 2614.5 keV calibration lines are presented in Table 3.3.

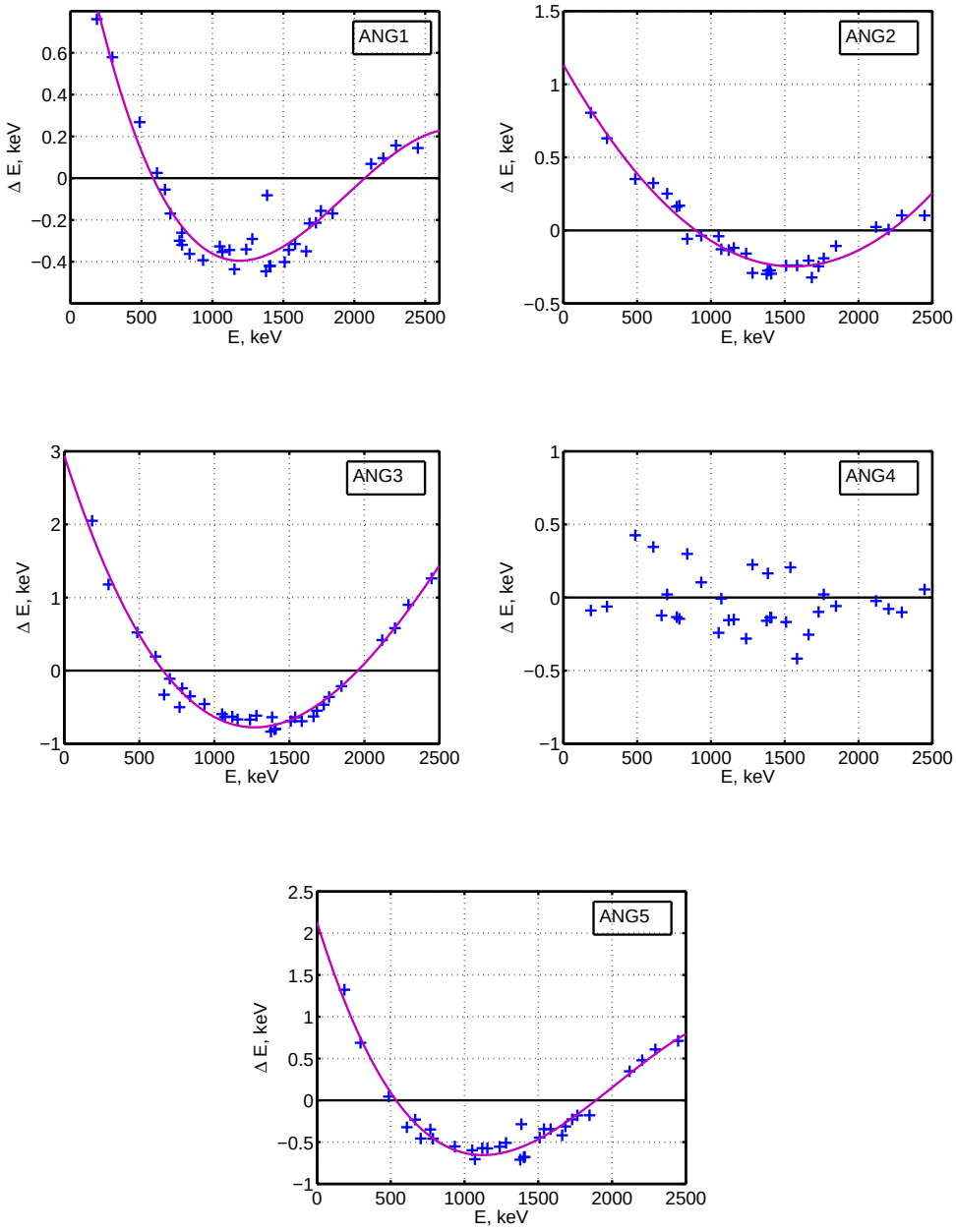

Figure 3.4: Residuals ΔE of the linear calibration with a ^{226}Ra source as a function of the energy for the five HdM detectors. Measurements were performed in November 2003. The cubic fits of the data are shown.

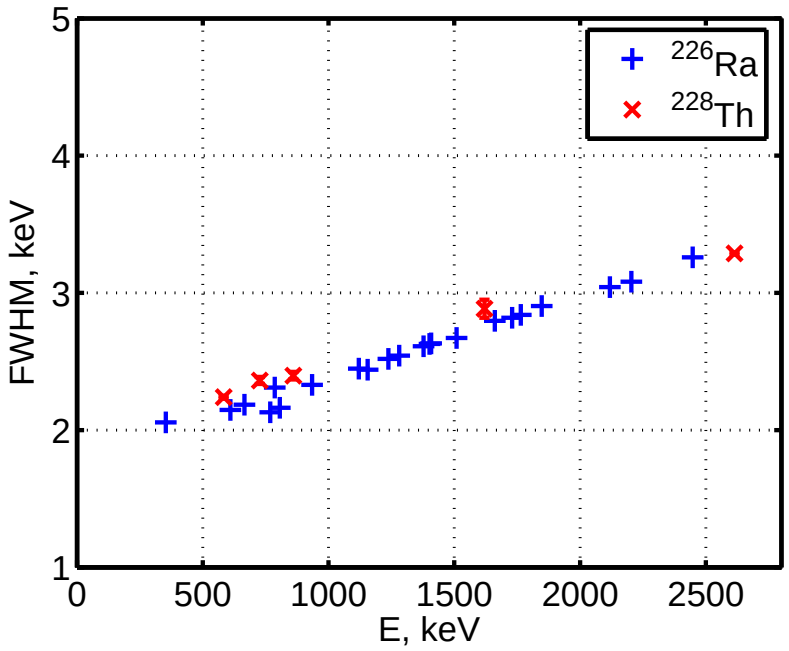

Figure 3.5: Energy resolution (FWHM) as a function of energy of the γ-peaks in the ^{226}Ra spectrum measured in November 2003 and in the ^{228}Th calibration spectrum, measured in 1999 (maximum error of FWHM is 0.05 keV). No resolution degradation was observed in November 2003.

Calibration period	Detector	Single escape (SE) ^{228}Th E_0=2103.5 keV		^{228}Th E_0=2614.53 keV	
		E_{peak} [keV]	FWHM [keV]	E_{peak} [keV]	FWHM [keV]
One of the weekly spectra	ANG1	2103.36	3.65	2614.40	2.96
	ANG2	2103.58	3.85	2614.46	3.43
	ANG3	2103.35	3.65	2614.66	3.00
	ANG4	2103.49	4.47	2614.61	3.48
	ANG5	2103.59	3.82	2614.52	3.36
After summing over the period 1995-2003	ANG1	2103.53	3.63	2614.52	3.00
	ANG2	2103.53	3.93	2614.53	3.40
	ANG3	2103.53	3.69	2614.52	3.04
	ANG4	2103.52	4.55	2614.53	3.98
	ANG5	2103.54	3.95	2614.54	3.38
After summing all 5 detectors over the period 1995-2003					
		2103.53	3.86	2614.53	3.27

Table 3.3: Positions (error ±0.05 keV) and energy resolutions (error ±0.05 keV) of two most important calibration lines measured over the period from 1995 to 2003. The summed spectrum shows that the calibration method does not introduce broadening of the peaks [14].

One can see that the positions and the energy resolution of the peaks are not deteriorated by this calibration method. The single escape (SE) peak at 2103.5 keV has generally a broader resolution compared to the full-energy peak. This is a known effect, arising because the positron and the atomic electron are not at rest at the moment of annihilation. The resulting net momentum of the particles increases the statistical uncertainty of energy, leading to the broadening of the peak (see, e.g. [39]), but it does not affect the peak position at 2103.5 keV. The slightly worse resolution of the SE peak does not degrade the energy calibration, but instead provides the advantage of having a calibration line close in energy to the $0\nu\beta\beta$ $Q_{\beta\beta}$ value.

Method of spectra relocation

Relocation of multichannel spectra is necessary in order to compare or add different spectra. The relocation of a multichannel spectrum into new energy bins E_k is performed as follows [42]: First, the energies E_j for all channels j of the original spectrum are calculated with a known calibration equation ($E_j = f_{cal}(j)$). Second, if the energy interval [E_j,E_{j+1}] is fully contained in a new bin [E_k,E_{k+1}], then the full

content of channel j is added to bin k. Otherwise, the content is distributed between bins proportionally to the fraction of energy in each covered bin. As an example, a schematic diagram of the applied method is shown in Figure 3.6. The fraction of

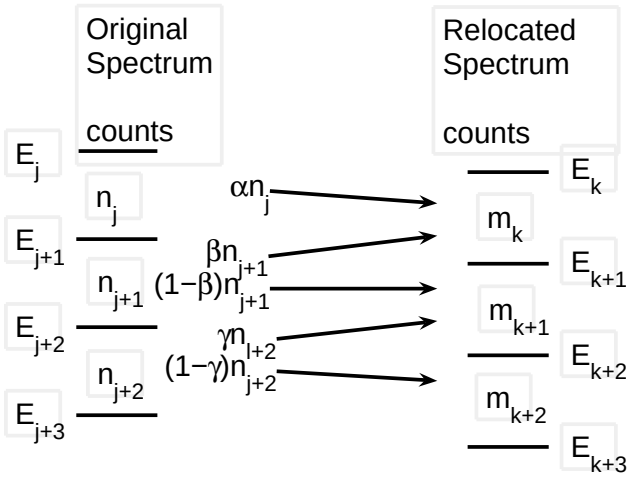

Figure 3.6: Scheme of the distribution of multichannel spectrum [42].

counts from channel $j+1$ to be added to the new bin k is $\beta = \frac{E_{k+1}-E_{j+1}}{E_{j+2}-E_{j+1}}$ and the fraction of counts to be added to the following bin $k+1$ is $(1-\beta)$. The content of the new bin k, $m_k = \alpha n_j + \beta n_{j+1}$, is not necessarily an integer number. In general, it does not obey a Poisson distribution because the variance $\sigma^2_{m_k} = \alpha^2 n_j + \beta^2 n_{j+1}$ is not equal to m_k.
The MATLAB implementation of the algorithm [43] was used for re-binning of all HdM calibration spectra.

3.4.3 Energy resolution and the accuracy of energy calibration of the sum spectrum

The energy resolution obtained with the combined spectrum over the 13 years of data acquisition of the HdM experiment is presented in Figure 3.7. At the $Q_{\beta\beta}$ value,

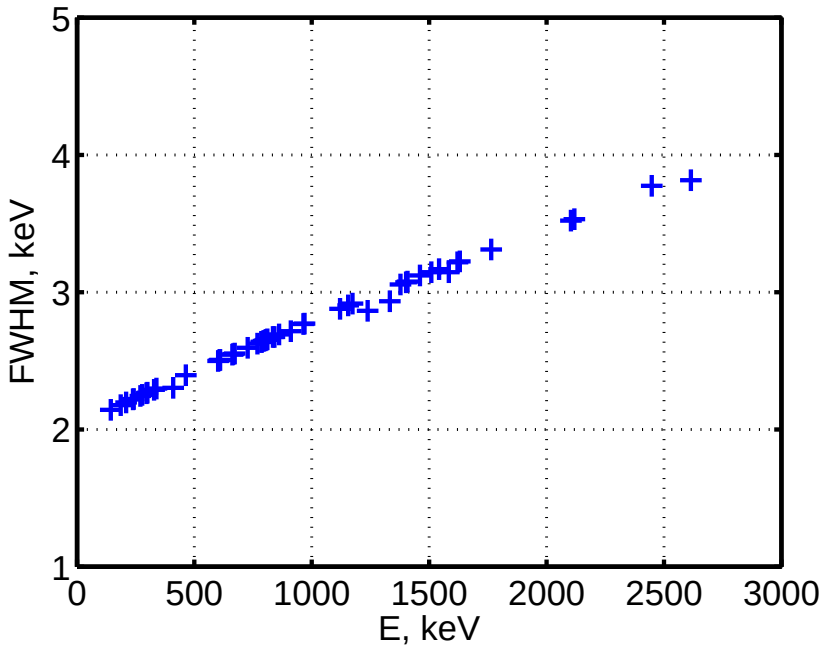

Figure 3.7: Energy resolution (FWHM) as a function of energy of the γ-peaks in the sum spectrum (1990 - 2003). Maximum error of FWHM is 0.1 keV

the interpolated energy resolution is found to be 3.49±0.03 keV, which is better than 4.23±0.14 keV presented in an earlier analysis [26]. The 20% improvement in the energy resolution of the sum spectrum, leading to a 10% increase in the sensitivity of the experiment, is a consequence of the refined summing procedure which was used for the individual 9570 data sets. Figure 3.8 shows the residuals ΔE of energy of the γ-peaks in the sum spectrum from 1990 to 2003. The energy calibration accuracy is better than 0.1 keV in the range 100-3000 keV.

An optimal bin width

The histogram's bin width controls the tradeoff between presenting a spectrum with too much or too little details. Gilmore and Hemingway [40] and Knoll [39] recommend four bins for FWHM of germanium spectra. In the case of the HdM spectrum, FWHM is 3.46 keV at 2039 keV, thus 1 keV bin width is optimal and convenient. Scott's reference rule [41] for optimal bin width is $w = 3.49 \cdot \sigma / \sqrt[3]{n}$, where σ is an estimate of the standard deviation and n is the number of counts in ROI. For σ=1.48 keV and n=100 the bin width is 1.1 keV, which is consistent with 1 keV bins.

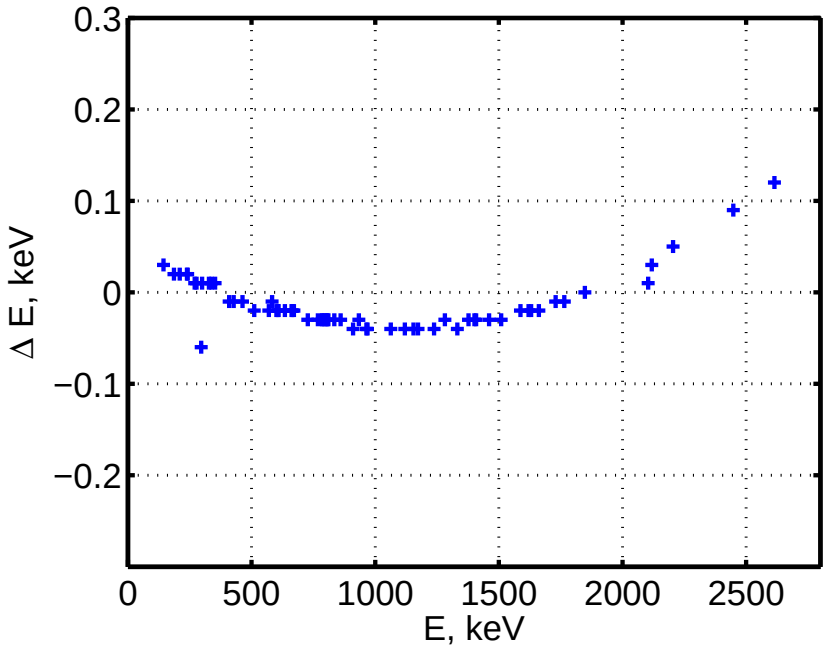

Figure 3.8: ΔE residuals from the reference values of the γ-peaks positions in the HdM spectrum (1990 - 2003). The maximum error for each point is ±0.1 keV.

3.5 Event selection in the summed spectrum

For the data collected in the first phase of the experiment (1990 - 1995), no information about individual events was recorded. Therefore, only a summed spectrum over this period with an exposure of 15.05 kg.y is used for the present analysis. In total 2142 runs (10 513 data sets for the five detectors) were taken since 1995. The duration of each run is on average one day. The first 200 days of operation of each detector, corresponding to about three half-lives of the ^{56}Co cosmogenic contamination ($T_{1/2}$=77.27 days), are excluded. In addition, 792 data sets, ∼7.5% of all data sets, were found to be corrupted because of an electronic problem, and have been rejected. To check the quality of each event, the 'Energy over Integral' (EoI) value was calculated as the ratio of the deposited energy measured by the ADC and the integral of the current pulse measured by the Flash ADC in the timing channel. Both values are proportional, unless the ADC or Flash ADC fails. The raw data sets and events considered for further analysis are only those which satisfy the following conditions:

1. no coincidences with another Ge detector and/or muon veto;

2. the deviation from the average count rate of each detector is within $\pm 5\sigma$;

3. the deviation from the average EoI value of each detector is within $\pm 3\sigma$;

Table 3.4 summarizes the data sets and events remaining after the applied cuts. Starting from 951 044 events, 786 941 events remain for analysis.

	Data Sets	Events
Full measurement	10 513	951 044
Corrupted data sets	792	92 553
Run Count Rate $> \pm 5\sigma$	151	32 922
Muon veto coincidence *		3 672
Ge - Ge coincidence		23 563
EoI selection $> \pm 3\sigma$		13 158
Data accepted	9 570	786 941

Table 3.4: Events and data sets accepted for the analysis of the HEIDELBERG-MOSCOW experiment for the period from 1995 to 2003.(*) Some muon veto events coincide with Ge - Ge coincidences [14].

In [50], the presence of anomalous peaks in the HdM data in the low-energy range (500 - 700 keV) was discussed. The peaks at 550 keV and 640 keV were observed in the spectrum of the ANG4 detector, but they had disappeared after application of the EoI cut, as demonstrated in Figure 3.9(left). The EoI data selection rejects

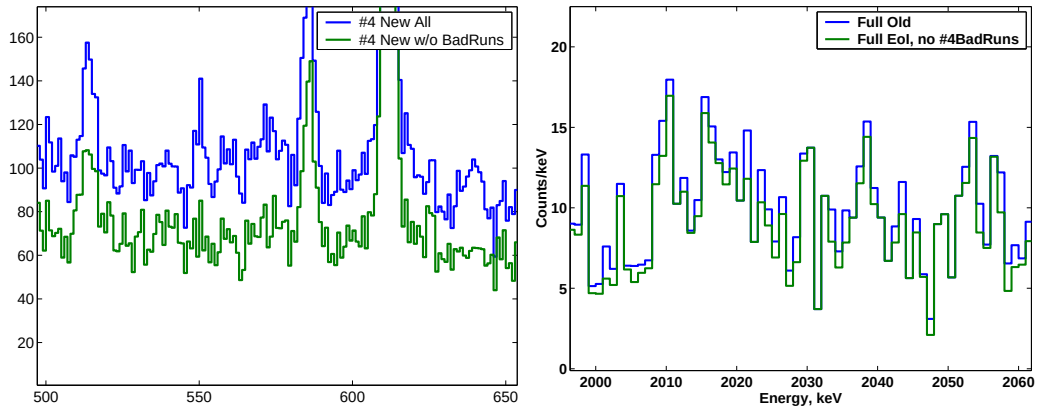

Figure 3.9: Left: the peaks at 550 keV and 640 keV in the low-energy range (500-700 keV) of the ANG4 detector disappear after applying the EoI cut and removing corrupted data sets. Right: the effect of these cuts in the sum spectrum around the $Q_{\beta\beta}$ value.

particulary the events which have an energy below the ADC threshold. The effect of these cuts in the region of interest around the $Q_{\beta\beta}$ value is also shown in Figure 3.9. One can see that, after applying the EoI cut, the structure of this part of the spectrum remains unchanged.

3.6 Identification of peaks in the sum spectrum

The total sum spectrum measured over the full energy range with all five detectors for the period from August 1990 to May 2003 is shown in Figure 3.10. The back-

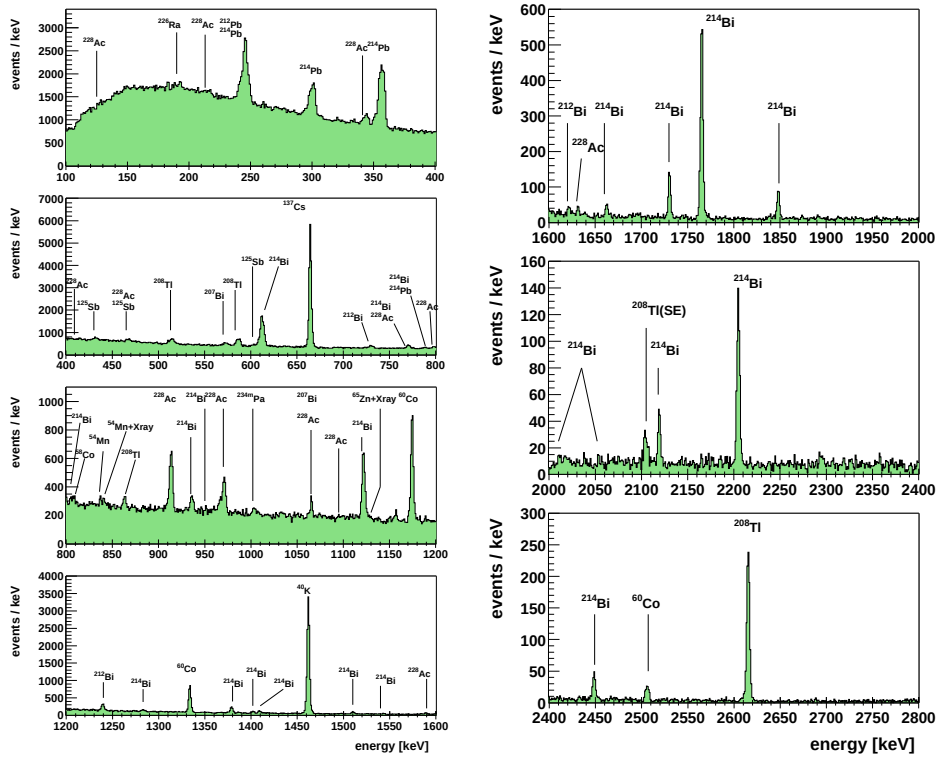

Figure 3.10: The total sum spectrum measured over the full energy range of all five detectors for the period from August 1990 to May 2003 [14].

ground identified by the measured γ lines in the spectrum consists of primordial activities (^{238}U, ^{232}Th and ^{40}K), anthropogenic radioactivity (^{137}Cs, ^{125}Sb, ^{207}Bi) and cosmogenic isotopes produced by cosmic ray activation (^{54}Mn, ^{58}Co, ^{60}Co). Figure 3.11 presents the comparison of the spectra collected with the low-energy (0-3 MeV) and the wide-energy (0-8 MeV) ADCs. The two spectra collected simultaneously coincide up to ∼3 MeV, showing good consistency. The intensities of the background peaks are determined from the spectrum. The background sources can be located using the measured and simulated relative peak intensities of the γ lines. The external α and β radiation does not contribute to the background because it cannot penetrate the 0.7 mm external dead layer of the p-type diodes. The detectors ANG1, ANG2 and ANG3 show negligible α-peaks but detectors ANG4 and ANG5 are contaminated with ^{210}Pb (see Fig. 3.12). This contamination, identified by α-peaks at 5245 keV from the daughter of ^{210}Pb (^{210}Po), is most likely located on the surface of the inner contact of the detectors. The energy of the ^{214}Po α particles (5304 keV) decreases by 64 keV as they pass through the 0.3 μm boron implantation

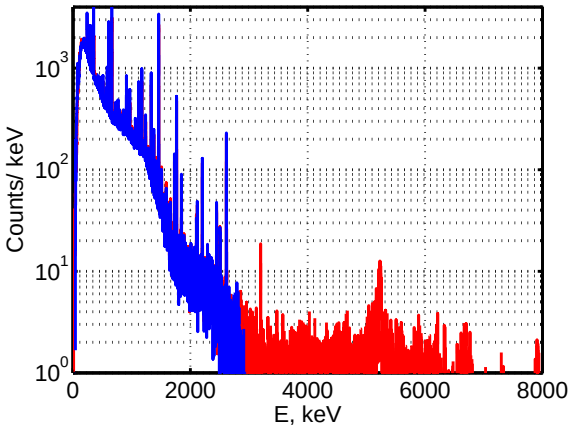

Figure 3.11: Comparison of the summed spectra collected in two energy ranges: 0 - 3 MeV and 0 - 8 MeV [14].

contact in the boreholes of the diodes.

The most significant background contribution in the region of interest comes from the Compton continuum of the 2614 keV gamma line of ^{208}Tl. Other contributions to HdM background come from ^{238}U and ^{226}Ra decay chain, mainly from ^{214}Bi, and cosmogenic contribution from summation of ^{60}Co. Table 3.6 lists all the spectral lines present in the HdM background spectrum. All nuclei contributing to the background in the region of interest have been commented. Gamma lines from ^{228}Ac, ^{212}Pb, ^{212}Bi and ^{208}Tl are present in the background. The parent long-lived nucleus of this chain is ^{232}Th or ^{228}Ra. In the high energy part of the spectra of ANG3, ANG4 and ANG5 (Fig. 3.12), a peak at 3198 keV is identified as a summation peak from the gamma-ray cascade 583.2+2614.5=3197.7 keV. The presence of this true coincidence summation peak indicates that the sources are very close to the detectors (within 1 cm). It is believed that this ^{232}Th contamination is located on the detector holders.

No secular equilibrium of ^{238}U with its daughter is observed. The 1001.9 keV gamma line in the HdM spectrum can be attributed to the ^{234m}Pa decay. The intensity of this gamma line is 250 ± 45 counts and the main contribution comes from the ANG3 and ANG5 detectors. Therefore, it shows a contamination of these detectors with ^{238}U. The relative intensities of the ^{214}Bi lines indicate that the ^{226}Ra contamination is located minimum 5 cm away from the diodes, probably in the copper cryostats or inner surface of the shield.

The 1173.2 and 1332.5 keV lines and their summation peak at 2505.7 keV from ^{60}Co are visible in the spectra of all detectors. The relative intensities of the summation peaks show that the holders of ANG1, ANG2 and ANG5 and the cryostats of ANG3 and ANG4 are contaminated with ^{60}Co. The method for localization of sources using relative intensity of γ-lines is described in Chapter 4.

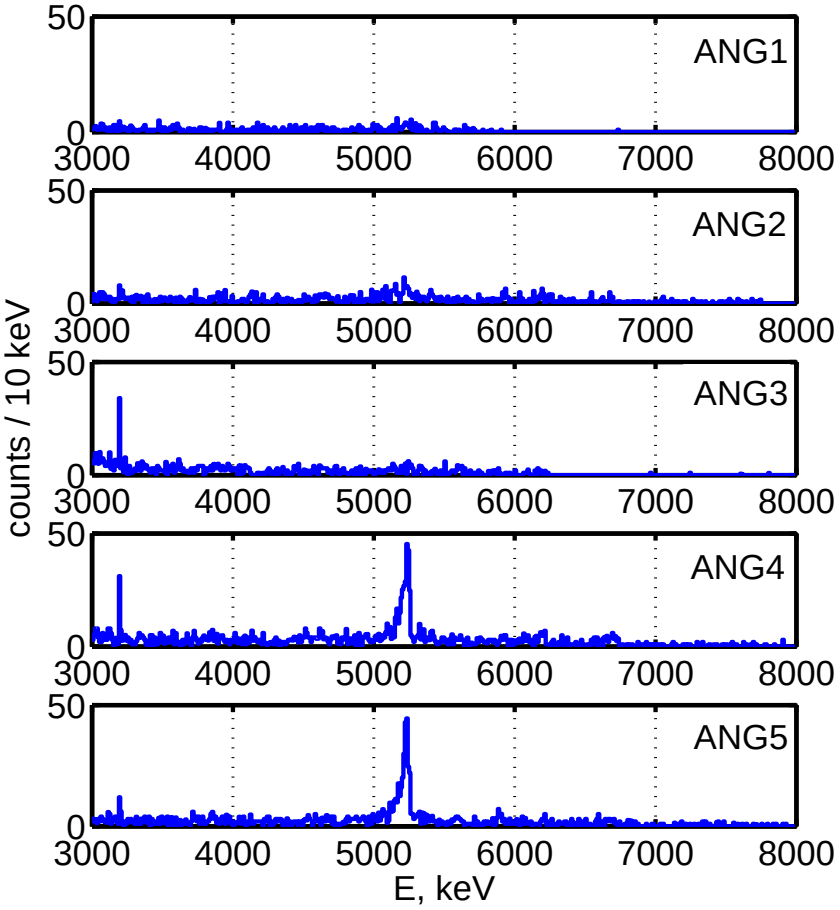

Figure 3.12: The high-energy part of the HdM detector spectra showing the α-peaks. The peaks from ^{210}Po, the daughter of ^{210}Pb, are clearly seen in ANG4 and ANG5 [14, 35].

Nuclide	E_γ [keV]	Peak Area	FWHM [keV]
RA-226	186.0	1152 ± 180	2.18
AC-228	209.4	451 ± 180	2.20
PB-212	238.6	6419 ± 197	2.22
PB-214	241.9	2831 ± 215	2.22
AC-228	270.3	170 ± 68	2.24
TL-208	277.4	169 ± 86	2.25
PB-214	296.1	4910 ± 184	2.26
PB-212	300.1	276 ± 159	2.27
AC-228	328.1	315 ± 113	2.29
AC-228	338.4	1302 ± 144	2.30
PB-214	352.6	9948 ± 343	2.62
AC-228	409.6	252 ± 213	2.30
SB-125	428.1	1113 ± 228	3.29
AC-228+ SB-125	463.5	850 ± 132	2.40
TL-208	511.2	2143 ± 236	3.55
BI-207	570.3	867 ± 151	2.74
TL-208	583.1	2566 ± 228	2.77
SB-125	600.8	450 ± 87	2.50
SB-125	606.8	589 ± 87	2.50
BI-214	609.3	7552 ± 96	2.51
SB-125	635.2	389 ± 179	1.98
CS-137	661.6	20201 ± 164	2.55
BI-214	665.5	289 ± 187	2.55
SB-125	671.7	135 ± 82	2.55
BI-212	727.2	579 ± 88	2.59
BI-214	768.4	769 ± 86	2.63
BI-212+ PB-214	785.4	242 ± 82	2.64
PB-214	786.0	176 ± 82	2.64
AC-228	794.8	660 ± 168	2.64
	801.8	178 ± 83	2.65
BI-214	806.2	275 ± 77	2.65
CO-58	810.8	171 ± 75	2.66
MN-54	834.8	420 ± 106	2.67
AC-228	840.8	200 ± 80	2.67
TL-208	860.5	449 ± 78	2.69
AC-228	910.8	2135 ± 115	2.72
BI-214	933.9	630 ± 131	3.15

Table 3.5: Background peaks in the measured sum spectrum for all five detectors in the energy range 140-2800 keV, for 71.7 kg y exposure (1990 - 2003), their energies (error ±0.1 keV), intensities and widths (error ±0.05 keV).

Nuclide	E_γ [keV]	Peak Area	FWHM [keV]
AC-228	964.6	458 ± 86	2.77
AC-228	968.9	1259 ± 82	2.77
PA-234m	1001.3	250 ± 78	3.77
BI-207	1063.3	634 ± 98	3.39
BI-214	1120.3	1926 ± 86	2.88
BI-214	1155.2	250 ± 62	2.90
CO-60	1173.2	3955 ± 88	2.92
BI-214	1238.1	807 ± 89	2.86
BI-214	1281.5	274 ± 66	3.54
CO-60	1332.3	3690 ± 90	2.93
BI-214	1377.7	675 ± 50	3.06
BI-214	1401.5	220 ± 42	3.07
BI-214	1408.0	292 ± 45	3.08
K-40	1460.8	13010 ± 134	3.12
BI-214	1509.2	261 ± 38	3.15
BI-214	1542.2	105 ± 32	3.17
BI-214	1583.4	50 ± 37	3.15
AC-228	1587.6	157 ± 42	3.71
BI-212	1620.6	127 ± 26	3.22
AC-228	1630.4	75 ± 27	3.22
BI-214	1661.8	163 ± 34	3.88
BI-214	1729.9	491 ± 40	3.05
BI-214	1764.5	2204 ± 51	3.31
BI-214	1847.7	324 ± 30	3.21
SE(2614)	2103.6	134 ± 21	3.52
BI-214	2118.5	185 ± 21	3.53
BI-214	2204.3	579 ± 33	3.89
BI-214	2448.0	193 ± 15	3.77
ΣCO-60	2505.8	156 ± 14	4.73
TL-208	2614.5	1184 ± 36	3.82
ΣTL-208 *	3198.0	80 ± 9	4.48
PO-210 α *	5245	454±22	53

Table 3.5: (Continued). The energy range 1900 - 2100 keV is analyzed separately in the Section 3.7 and Chapter 4. (*) The summation peak from ^{208}Tl and the ^{210}Po α-peak are measured with exposure 56.6 kg y (1995-2003). (SE-single escape peak, Σ - summation peak.)

3.7 Analysis of the spectrum around $Q_{\beta\beta}$

3.7.1 Method of fitting

The least squares method with the Levenberg-Marquardt algorithm has been used to analyze the spectra. The Levenberg-Marquardt method [44] is one of the most developed and tested minimization algorithms, finding fits most directly and efficiently [45]. It is also reasonably insensitive to the starting values of the parameters. A nonlinear fit in the range 2000 - 2060 keV was performed. The following procedure was used: The histogram N_i, where i is the bin number, corresponds to a spectrum with bin energy E_i. The spectrum is fitted using n Gaussians $G(E_i, E_{\circ j}, \sigma_j)$, where n is the number of lines to fit, $E_{\circ j}$ and σ_j are the estimated centroid and width of the Gaussian j:

$$G(E_i, E_{\circ j}, \sigma_j) = \frac{1}{\sigma_j \sqrt{2\pi}} \exp\Big[-\frac{(E_i - E_{\circ j})^2}{2\sigma_j^2}\Big]. \tag{3.1}$$

Different background models $B(E_i)$ were used to fit the data: simulated background (linear with fixed slope)[27], linear and constant background. The fitting function $M(E_i)$ is a sum of Gaussians and background models:

$$M(E_i) = \sum_j^n S_j \cdot G(E_i, E_{\circ j}, \sigma_j) + b \cdot B(E_i), \tag{3.2}$$

where S_j are the estimated peak intensities and b is the background index. The peak intensities, the mean centroids, the widths and the background index are found by minimizing the norm of errors:

$$S_j, E_{\circ j}, \sigma_j, b = \arg\min \sum_i^m [M(E_i) - N(E_i)]^2, \tag{3.3}$$

where m is the number of bins in the analyzed part of the spectrum. Following the suggestion of the Particle Data Group [46], the number of events in the measured spectrum was compared to the number of events given by the fit. Because these numbers are identical on a percent level, no normalization is required. This method has advantages over others of providing an estimate of the full error matrix. The MATLAB Statistical Toolbox [49] provides a function for calculating the confidence interval of the parameters. It uses the residuals of the fit and the Jacobian matrix J_{ij} of M_i around the solution of Eq. 3.3 to obtain the error of the parameters. The confidence intervals calculated by the MATLAB statistical function were tested with a MC simulation. 100 000 spectra were simulated with a Poisson-distributed background and a Gaussian-shaped peak of given intensity. An analysis of the true number of counts inside the calculated confidence interval was performed. Table 3.6 shows the results of this confidence test. For example, peaks with 30 counts on a background of 10 events per bin were analyzed with 100 000 simulated spectra. In 99 979 cases, the true value of the peaks was within the 4σ calculated confidence interval (compare to the expected value of 99994 cases for 4σ). It means that the calculated confidence interval is underestimated by $\sim 0.3\ \sigma$.

B	S = 10				S = 20				S = 30			
	1σ	2σ	3σ	4σ	1σ	2σ	3σ	4σ	1σ	2σ	3σ	4σ
2	66505	93781	99183	99932	63967	93176	99219	99952	62094	92191	99121	99932
7	66879	91683	98476	99900	67618	94733	99498	99961	66332	94443	99539	99967
10	64962	90029	98380	99918	68210	94921	99455	99933	67352	94784	99554	99979
Expected:												
	68269	95449	99730	99994	68269	95449	99730	99994	68269	95449	99730	99994

Table 3.6: Results of the simulations of 100 000 spectra giving the number of cases where the true number of counts in the peak is found in the calculated confidence interval. The spectra have a Poisson-distributed background and a Gaussian-shaped peak of a given intensity. The simulations were performed for different backgrounds (B), peak areas (S) and confidence levels. The least squares method, using the Levenberg-Marquardt algorithm implemented in the MATLAB function [49], was used [14].

3.7.2 Fitting results

Figure 3.13 compares the fit with the measured spectrum in the range around the $Q_{\beta\beta}$ value (2000 - 2060 keV). The peak positions, their intensities and the back-

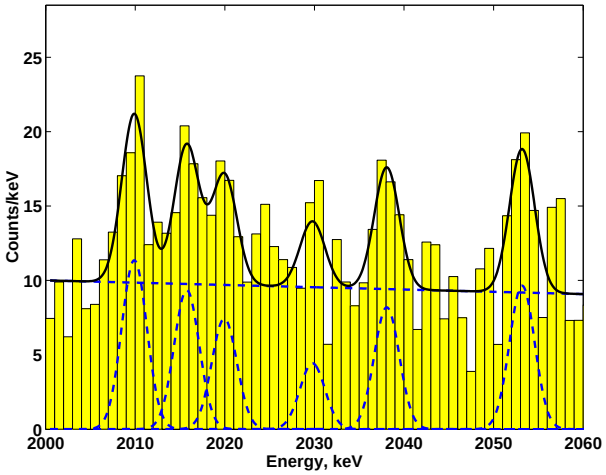

Figure 3.13: The total sum spectrum of all five detectors (in total 10.96 kg enriched in ^{76}Ge), from November 1990 to May 2003 (71.7 kg y) in the 2000 - 2060 keV range and its fit (solid line) with fixed peak widths, but free centroids [14].

ground are given simultaneously by the fit. The positions and the intensities of the peaks are fitted but the peak widths are fixed. Table 3.7 gives the intensities and the positions of the spectrum peaks in the region of interest. The signal at $Q_{\beta\beta}$ in the full spectrum at $\sim$ 2039 keV reaches a 4.2 σ confidence level for the period 1990-2003. The intensities of the 2022 and 2053 keV ^{214}Bi lines are higher than

Line [keV]	Detectors ANG1-5 1990-2003, 71.7 kg y, [14]		Expected and Measured Intensity with a ^{226}Ra source		
	Fit Energy, [keV]	Fit Intensity, [counts]	Rel. Intensity, [%], TOI* [28]	Expected TOI, [counts]	Measured ^{226}Ra, [counts]
2010.7	2009.9±0.3	39.9±6.9	0.047 ± 0.003	5.6 ± 0.4	10.9±0.3
2016.7	2015.7±0.4	32.8±7.1	0	0	13.4±0.3
2021.8	2019.9±0.5	26.1±7.1	0.020 ± 0.003	2.4 ± 0.3	2.6±0.3
2030	2029.8±0.8	15.5±6.9	–	–	–
2039.0	2038.1±0.4	28.75±6.9	–	–	–
2052.9	2053.2±0.4	33.9 ±6.8	0.069± 0.005	8.2± 0.6	8.0±0.3
2204.2	2204.3±0.1	579 ±33	5.08±0.4		

Table 3.7: Peaks of the measured spectra (1990-2003) in the 2000-2060 keV range, and their non-linear least squares fit with unconstrained intensities and peak positions. The energies and intensities from the fit, and their 1σ errors are provided [14]. The expected intensities of the weak ^{214}Bi lines are calculated using the intensity of the 2204 keV (5.08%) line in the HdM spectrum (579±33 counts). All peaks measured with the ^{226}Ra source are normalized to the 2204 keV peak area in the HdM spectrum. The 2030 keV line has not been identified. These measurements are discussed in the next Chapter. (*)TOI: Table of Isotopes, TSC: true coincidence summing.

expected relative to the intensity of a strong ^{214}Bi line at 2204 keV. The table of isotopes [28] gives relative intensities of 5.08±0.04% and 0.069±0.005%, for the ^{214}Bi lines 2204.2 and 2052.9 keV respectively. The detection efficiency for photons in the region 2000–2060 keV and the detection efficiency for 2204 keV photons are equal within a few percent. The intensity of the 2204 keV line, 579±33 counts (Tab. 3.6), gives an expected count of 8.2±0.6 in the 2053 keV peak. It is four times smaller than the number of counts obtained from the presented fit (33.9±6.8 counts). In order to understand the discrepancy in the line intensities from the spectrum, fits were performed using wider energy intervals. Figure 3.14 shows the same spectrum as in Figure 3.13 but the data are fitted over energy windows of 60, 80 and 100 keV width.

The peak intensities and the background level depend on the energy windows used for fitting. An empirical model was created based on measurements with sources and simulated spectra to investigate the shape of the spectrum and to optimize the fitted energy interval. This empirical model is presented in the next Chapter.

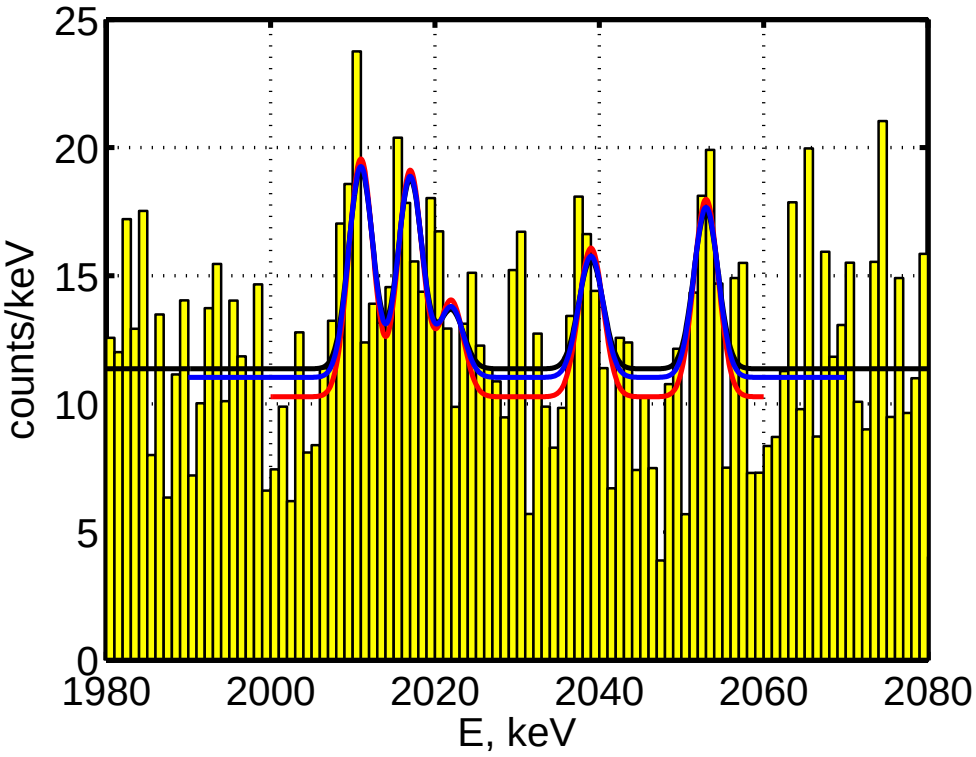

Figure 3.14: Fits of the HdM spectrum for three energy windows: 2000-2060 keV, 1990-2070 keV and 1980-2080 keV. The spectrum is fitted with fixed peak positions [28] and fixed peak widths (3.48 keV FWHM) defined by the energy calibration. The fitted background depends on the energy interval.

Line	Energy window		
E, [keV]	2000-2060 keV	1990-2070 keV	1980-2080 keV
2010	34.5± 8.2	31.5 ± 8.4	29.4 ± 8.7
2017	32.9 ± 8.2	30.0 ± 8.4	28.0 ± 8.6
2022	14.0 ± 8.2	11.0 ± 8.4	9.0 ± 8.7
2039	21.6 ± 8.3	18.5 ± 8.4	16.4 ± 8.7
2053	28.7 ± 8.3	25.6 ± 8.4	23.4 ± 8.7
B [counts/keV]	10.3 ± 0.6	10.9 ± 0.5	11.3 ± 0.4

Table 3.8: Intensities of the peaks in the region of interest around $Q_{\beta\beta}$ obtained from fit using different energy windows.

3.8 Conclusions

The improved analysis of the HdM raw data collected during 1990–2003 was performed, based on the investigation of the calibration curves of the HdM experiment. The better quality of the energy calibration and the energy resolution of the summed spectrum allows to fit the spectrum with accurate peak positions and widths. Because the energy resolution determines the sensitivity of the experiment, a 20% improvement in the energy resolution leads to a 10% increase in sensitivity. This has lead to publications [14, 15].
The sum spectrum was analyzed and the γ and α peaks were identified and their intensities are presented. The fits of the region around the $Q_{\beta\beta}$ value show that the resulting peak intensities depend on the width of the analyzed energy window. For an optimization of the fitted energy interval a model of the HdM background was proposed.

Chapter 4

A posteriori Background Evaluation for the HdM Experiment

The HdM background around the $Q_{\beta\beta}$ value consists of contributions from the Compton scattering of the ^{208}Tl, ^{214}Bi and ^{60}Co γ-rays as well as the continuum from neutrons and muons. An interpretation of the HdM background was done, based on measurements with sources using the HdM detectors after their handover to the GERDA collaboration in 2004. ^{232}Th, ^{226}Ra and ^{60}Co sources were placed at various locations, with different thicknesses of lead absorber between the source and the detector. The goal was to reproduce the proper line shapes and the relative intensities observed in the HdM background. The resulting spectra together with the contributions of ^{137}Cs, ^{40}K, ^{210}Pb and the calculated shape of $2\nu\beta\beta$ at lower energies were normalized and used to fit the HdM background spectrum.

4.1 Using peak ratios for the localization of background sources

The shape of the spectrum is highly dependent on the position of the source, and the amount of absorber between the source and the detector. Different peak intensity ratios result from different combinations of distance and absorber thickness. The true coincidence summing (TCS) effect, which happens when more than one photon is emitted in a nuclear de-excitation, can help to resolve these combinations.
There is a certain probability that both photons simultaneously deposit their full energy in the same germanium crystal. Because detection efficiency is inversely proportional to squared distance, TCS probability depends strongly on the distance between the source and the detector, and on the thickness of absorbing material.
The intensity ratio between a TCS summation peak and a single γ-peak depends on the distance between the source and the detector. The decay of ^{214}Bi (decay daughter of ^{226}Ra) emits different combinations of photons (Fig. 4.1(Top)). The 1994 keV,

2010.7 keV and 2016.7 keV peaks in the spectrum can originate from TCS with the 609.3 keV photon (emission probability = 46.1%) with the 1385.3 keV photon (probability = 0.757%), the 1401.5 keV photon (probability = 1.27%) and the 1408.0 keV photon (probability = 2.15%), respectively [28]. The ratio of intensities between the summation peak at 2016.7 keV and a major peak at 2204.2 keV (probability = 5.08%) decreases with distance.
Single γ-peak intensity ratios do not depend on distance, but on the thickness of absorber. The ratio of the intensity of the 609.3 keV and 2204.2 keV ^{214}Bi lines decreases with increasing absorber thickness, and therefore can be used to determine the amount of material between the source and the detector. This value leads to the distance between the source and the detector using TCS.
The same method was used to localize the ^{208}Tl and ^{60}Co contamination. For ^{208}Tl, the summation peak at 3197 keV and γ-lines at 2614.5 keV (probability=99%) and 583.4 keV (probability= 85.5%) were used. The summation peak at 2505.7 keV from 1173.2 and 1332.5 keV lines was used to localize ^{60}Co sources. The localization of ^{60}Co was performed by using MC simulations, while the ^{232}Th and ^{226}Ra contaminations were localized by comparison with source measurements.

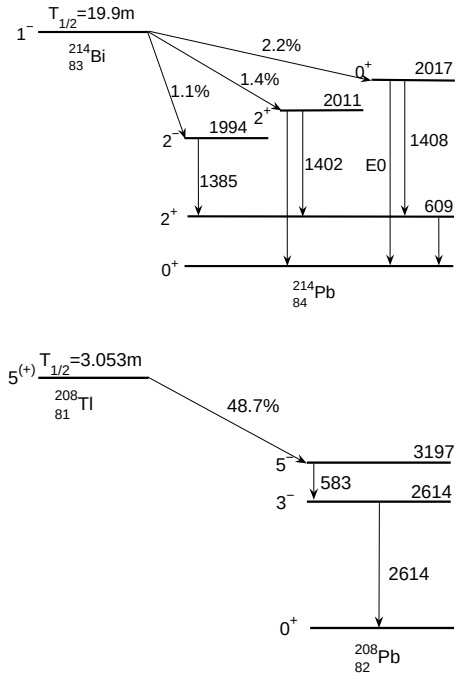

Figure 4.1: Reduced decay scheme of ^{214}Bi and ^{208}Tl showing the relevant levels for the true coincidence summing effect in germanium detectors [28].

4.2 *A posteriori* spectral shape measurements with sources

Spectra were measured in 2005-2006 for different positions of the ^{226}Ra and ^{232}Th sources using the ANG3 enriched detector (2.44 kg). It has an external diameter of 7.85 cm and a length of 9.35 cm. The distance between the top of crystal and the copper cap is 2.85 cm. The detector setup with the lead absorber and the position of the source are shown in Fig. 4.2. The spectra were measured with a standard

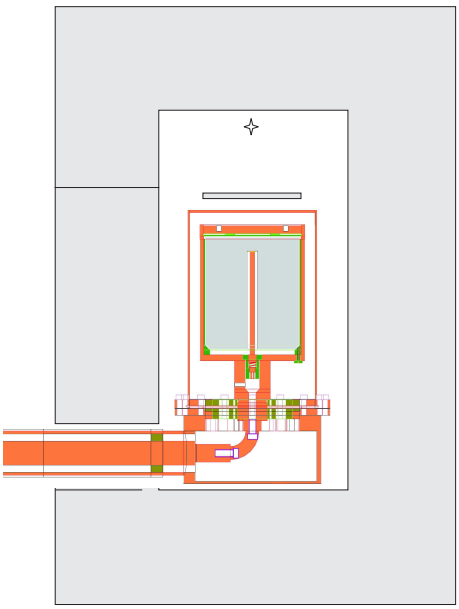

Figure 4.2: Schematic view of the ANG3 detector used in the spectral shape measurements, the source and the lead absorber. The setup is shielded with 10 cm of lead (gray area).

ORTEC spectroscopy amplifier and a multichannel analyzer. The energy resolution was ∼3keV at 1332 keV. To reduce the external background, the detector was surrounded by 10 cm of lead shield. Consequently, the background contribution during the measurements was not higher than 1% of the total count rate measured with the sources. To avoid random coincidences, the count rates were not higher than 1000 counts per second. Two ^{226}Ra sources, both enclosed in stainless steel containers with 0.5 mm walls, were used. One of the sources, with an activity of 936 Bq, was used for the measurements close to the detector (0-5 cm). The second source, with an activity of 95.2 kBq, was used for measurements far from the detector cap (10-20 cm) and with a thick lead absorber. The activity of the ^{232}Th source was 17 kBq. The sources were measured at 0, 1, 2, 3, 5, 10, 15, and 20 cm from the detector cap. At each position a 3, 6, and 9 mm thick lead absorber was used.
The TCS effect for the ^{214}Bi lines in the region of interest is shown in Fig. 4.3. The ^{226}Ra spectra are normalized to the area of the 2204 keV peak. The peaks at 2022 and 2053 keV are less affected by TCS than the peaks at 1994, 2010 and 2017 keV. The intensities of the measured 2022 and 2053 keV peaks are in agreement with

TOI[28] (Tab. 3.7). Without any absorber, the summing line intensities depend

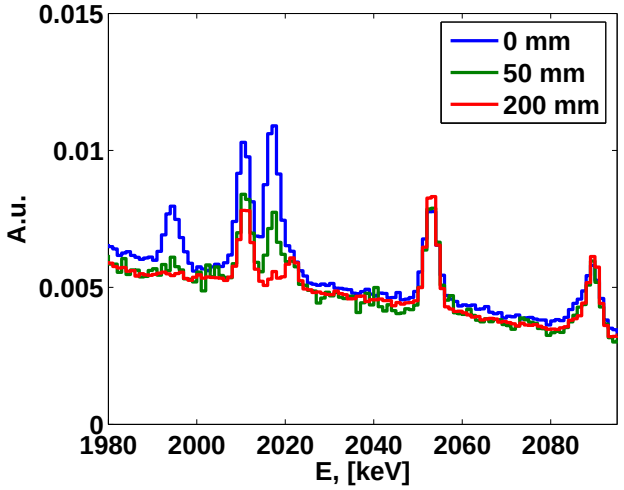

Figure 4.3: Spectrum shapes for three positions of the ^{226}Ra source (0 mm, 50 mm and 200 mm from the top of the detector copper cap). The spectra are normalized to the area of the 2204 keV peak. The peaks at 1994 keV and 2017 keV are not present in the spectrum at 200 mm, but become stronger when the source is closer to the detector. The peak at 2053 keV is practically not affected by TCS.

only on the inverse squared distance between the source and the detector. In reality, the source is distributed in the detector construction materials. To find the effective absorbtion material thickness, the ratios of the major gamma lines of ^{226}Ra and ^{208}Tl as a function of the absorber thickness were measured. These ratios are approximately constant (within 5%) for all measured distances from the detector, but depend on the absorber thickness (Fig. 4.4 and 4.5). From the measured ratios of the 609 and 2204 keV peaks of the ^{214}Bi decay and the 583 and 2614 keV peaks of the ^{208}Tl decay, the absorber thickness between the source and the cryostat was estimated. Using these additional absorber thicknesses and the relative intensities of the summation peaks (Tab. 4.1), the source locations were found, as was shown in section 3.6.

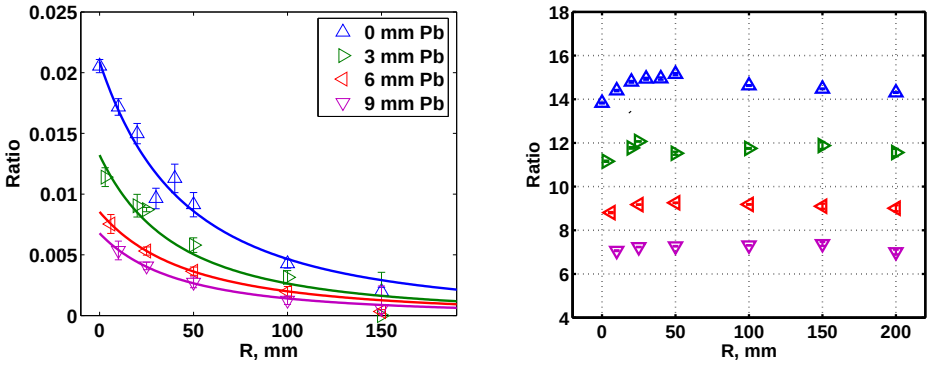

Figure 4.4: Left: Ratios of the summation peak at 2016 keV to the γ-line at 2204 keV vs. distance of the source to the detector and thickness of the lead absorber. Right: Ratios of 609 keV line to 2204 keV line vs. distance of the source to detector and thickness of the lead absorber.

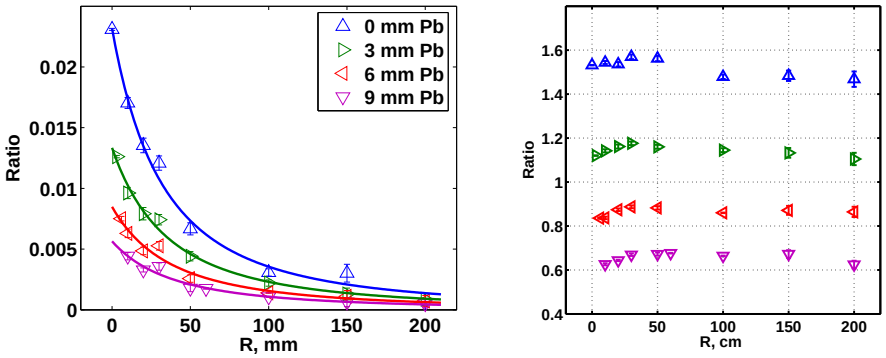

Figure 4.5: Left: Ratios of the summation peak at 3197 keV to the γ-line at 2614 keV vs. distance of the source to the detector and thickness of the lead absorber. Right: Ratios of 583 keV line to 2614 keV line vs. distance of the source to detector and thickness of the lead absorber.

Isotope	E, [keV]	ANG1 [counts]	ANG2 [counts]	ANG3 [counts]	ANG4 [counts]	ANG5 [counts]
^{232}Th	583	220±18	260±23	549±28	303±24	350±27
	2614	86±9	154±13	308±18	154±13	242±16
	3197	3±2	4±2	32±5	28±5	10±3
^{214}Bi	609	809±30	1450±41	1561±43	1290±40	1643±45
	2204	39±6	118±11	105±11	81±9	148±13
	2016	1±3	9±3	4±3	2±3	9±4
^{60}Co	1332	233±16	713±28	454±23	398±22	653±27
	2505	5±2	42±7	17±5	14±4	35±6

Table 4.1: The HdM background peak intensities used for source localization. The exposure is 56.6 kg y, during the period of 1995 - 2003.

4.3 HdM background model

Eight spectral shapes were included in the model matrix M:

- ^{226}Ra spectral shape, measured at 5 cm from the detector;
- ^{232}Th spectral shape, measured at 0 cm from the detector;
- ^{60}Co spectral shape, simulated in the holders of the detectors;
- ^{210}Pb spectral shape, simulated in the HdM lead shield [36];
- ^{40}K spectral shape, simulated in the HdM setup;
- ^{137}Cs spectral shape, simulated in the ANG5 cryostat;
- muons' and neutrons' contribution to the continuum, calculated from the fit of the simulation [36] and [60];
- calculated shape of the $2\nu\beta\beta$.

The contribution C_j of each of the N spectral shapes to the measured spectrum S_i is an approximate solution of a system of n linear equations:

$$\sum_{j=1}^{N} M_{ij} \cdot C_j \simeq S_i^{meas}, (i = 1..n), \tag{4.1}$$

where n is the number of channels. It was solved using a least squares method in the energy interval from 250 keV to 2800 keV. The sum of all components S^{model} is expressed as:

$$S_i^{model} = \sum_{j=1}^{N} M_{ij} \cdot C_j, \tag{4.2}$$

and is shown in Figure 4.6 together with each contribution. The total counts from each contribution in the background model are summarized in Table 4.2. The intensity of the major peaks in the HdM and model spectra are compared in Table 4.3. The calculated ^{214}Bi, ^{60}Co, ^{40}K and ^{137}Cs peak intensities are in agreement with the HdM spectrum. The intensity of the 2614 keV ^{208}Tl line is higher in the model spectrum. According to Figure 4.5, the ratio of the measured intensities of the ^{208}Tl lines (Tab. 4.1), suggests that the location of the ^{232}Th contamination is closer to the diodes, probably on the holder.

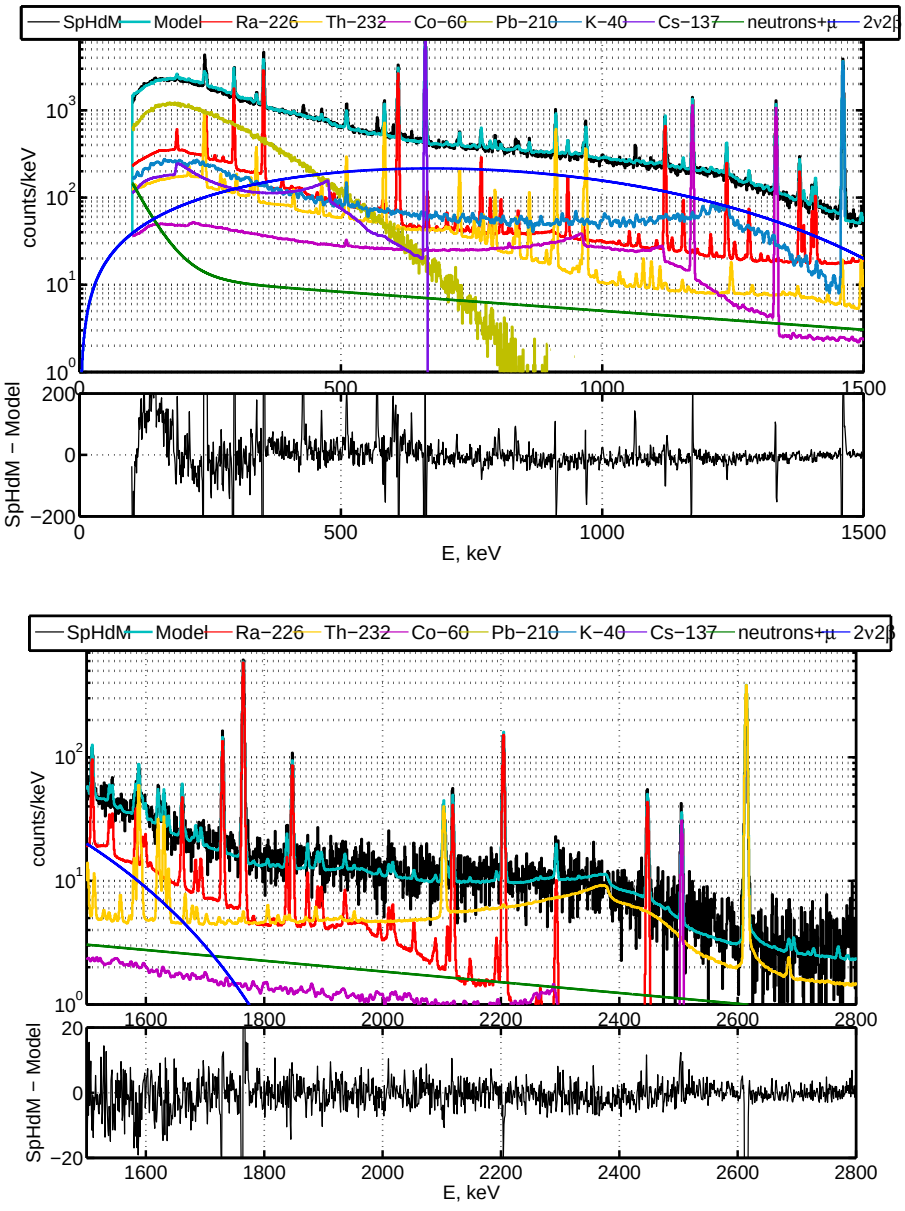

Figure 4.6: The HdM spectrum, its model and its components.

Source	Counts
^{226}Ra	164060 ±2378
^{232}Th	90390 ±12959
^{60}Co	43960 ± 949
^{210}Pb	268910±2832
^{40}K	132930 ±1578
^{137}Cs	83820±676
Neutrons+muons	16660±2123
$2\nu\beta\beta$	193250 ± 2822
Σ Model	993980
Σ HdM	982580

Table 4.2: Major contributions to the HdM spectrum calculated with a linear least squares method (Eq. 4.1).

Isotope	E [keV]	HdM spectrum	Model spectrum
^{137}Cs	662	20201±164	21220±150
^{40}K	1461	13010±134	12900±120
^{60}Co	1332	3690±90	3782±66
Σ^{60}Co	2505	156±14	111±12
^{214}Bi	1764	2204±51	2220±48
^{214}Bi	2204	579±33	600±25
^{214}Bi	2447	193±15	187±15
^{208}Tl	583	2566±58	2438±68
^{208}Tl	2614	1184±36	1590±40

Table 4.3: Comparison of the major peaks in the measured HdM spectrum and in the model spectrum (Eq. 4.2).

Σ Bkg. [cts/keV]	^{214}Bi [cts/keV]	^{208}Tl [cts/keV]	^{60}Co [cts/keV]	Neutrons+muons [cts/keV]
11.9	3.0	5.2	1.2	2.5
100%	25%	44%	10%	21%

Table 4.4: Composition of the background model at 2039 keV.

The histograms of the normalized residuals $\frac{S^{meas}-S^{model}}{\sqrt{S^{model}}}$, between the HdM spectrum and the model spectrum, were fitted with Gaussian for three energy ranges (Fig. 4.7). The distributions' standard deviations are equal to one (within error) and their mean values are slightly below zero, in agreement with the ∼1% excess of total counts in the model spectrum over HdM, as seen in Table 4.2. The deviation from the Gaussian at tails is related to the slightly different peak widths in the model and in the HdM spectrum.

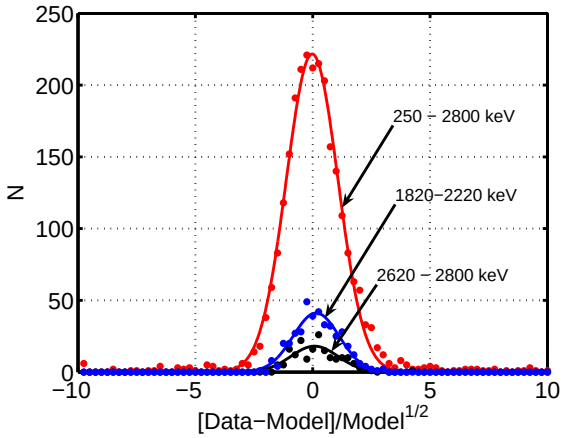

Figure 4.7: Distributions of the normalized residuals between the HdM spectrum and the model spectrum, fitted with Gaussian for three energy ranges.

The least squares fit, obtained for the full spectrum in the range 250 - 2800 keV, was examined at smaller energy intervals around the $Q_{\beta\beta}$ value to check probable local deviations. The region of interest around $Q_{\beta\beta}$ of the HdM spectrum was tested using several energy intervals ΔE. The χ^2 value was calculated according to Eq. 4.3:

$$\chi^2(\alpha \cdot S_Q^{model}) = \sum_{i \in \Delta E} \frac{(S_i^{meas} - \alpha \cdot S_i^{model})^2}{S_i^{meas}}, \tag{4.3}$$

where α is a scale parameter. All the five tested energy intervals, including 2000 - 2060 keV, give the same value of the mean background at the $Q_{\beta\beta}$ value: 11.9±0.5 counts/keV (68% c.l.) as shown in Figure 4.8.
The components of the model background in the region near 2039 keV are shown in Table 4.4. The neutron and muon contributions to the background are 21% of the total background at the $Q_{\beta\beta}$ value, 57% of this contribution was from the ANG4

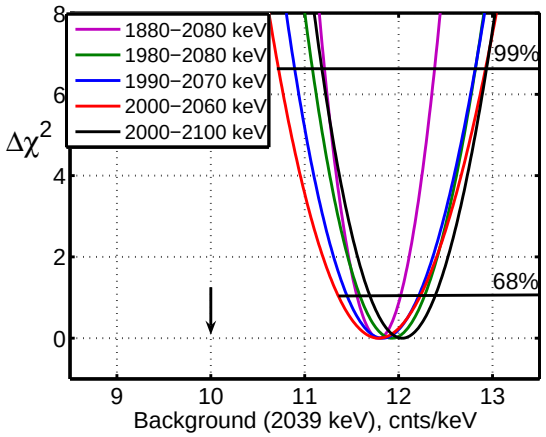

Figure 4.8: χ^2 as a function of the scaled model background for the five energy windows (Eq. 4.3). The arrow shows the background value obtained with an unconstrained fit (Fig. 3.13) in the 2000-2060 keV energy interval.

detector, which operated without a muon veto.

4.4 HdM fit results in the region of $Q_{\beta\beta}$

Given the accurate calibration of energy and energy resolution, the fit of the HdM spectrum was performed using the presented background model. An estimation of lower and upper limits on the signal in each bin was performed using the ADMA program [48], according to Feldman-Cousins [47]. Table 4.5 presents the HdM spectrum in the energy interval 2000-2060 keV (71.7 kg y). The fourth and fifth columns show the 68.27% C.L. intervals for a Poisson signal, assuming the mean background of the presented model (11.8±0.5 Cts/keV at $Q_{\beta\beta}$).

E [keV]	HdM spectrum [cts/keV]	Model spectrum [cts/keV]	LL	UL
1980	12.6	13.0	0.0	4.3
1981	12.0	12.8	0.0	3.5
1982	17.2	12.7	1.1	9.1
1983	12.9	12.8	0.0	4.5
1984	17.5	12.8	1.6	10.0
1985	8.0	12.7	0.0	6.4
1986	13.5	12.7	0.0	5.6
1987	6.3	12.7	0.0	0.3
1988	11.2	12.8	0.0	2.3
1989	14.0	12.8	0.0	5.5
1990	7.2	12.7	0.0	0.5
1991	10.0	12.9	0.0	1.5
1992	13.7	13.3	0.0	5.0
1993	15.5	13.8	0.1	7.0
1994	10.1	13.9	0.0	1.0
1995	14.0	13.6	0.0	4.7
1996	11.9	13.2	0.0	3.2
1997	11.0	12.9	0.0	2.1
1998	14.7	12.6	0.3	6.7
1999	6.6	12.3	0.0	0.5
2000	7.4	12.5	0.0	0.9
2001	9.9	12.4	0.0	2.2
2002	6.2	12.2	0.0	4.2
2003	12.8	12.2	0.0	5.4
2004	8.1	12.2	0.0	9.9
2005	8.4	12.3	0.0	9.9
2006	11.4	12.5	0.0	3.0
2007	13.2	12.7	0.0	5.4
2008	17.0	13.5	1.5	9.9
2009	18.6	14.5	3.0	11.9
2010	23.8	15.1	7.4	17.4
2011	12.4	14.8	0.0	4.4
2012	13.9	13.9	0.1	6.4
2013	13.2	13.3	0.0	5.4
2014	14.6	13.1	0.6	7.4
2015	20.4	14.4	3.9	18.4
2016	17.8	15.5	2.2	10.9
2017	15.6	15.7	1.0	8.9
2018	14.4	14.6	0.1	6.4
2019	18.0	13.5	2.2	10.9
2020	16.7	13.0	1.5	9.9
2021	12.9	12.9	0.0	5.4
2022	9.9	12.6	0.0	2.2
2023	13.1	12.3	0.0	5.4
2024	15.1	12.2	0.0	5.4
2025	12.3	12.0	0.0	4.4
2026	11.4	12.0	0.0	3.0
2027	10.9	12.0	0.0	3.0
2028	9.5	12.1	0.0	2.2
2029	15.2	12.0	0.6	7.4

E [keV]	HdM spectrum [cts/keV]	Model spectrum [cts/keV]	LL	UL
2030	16.7	12.1	1.5	9.9
2031	5.7	11.8	0.0	0.4
2032	12.7	11.9	0.0	5.4
2033	9.9	11.8	0.0	2.2
2034	8.3	11.8	0.0	9.9
2035	9.8	11.8	0.0	2.2
2036	13.4	11.9	0.0	5.4
2037	18.1	11.9	2.2	10.9
2038	16.6	11.9	1.5	9.9
2039	14.4	11.8	0.1	6.4
2040	11.4	11.7	0.0	3.0
2041	6.7	11.8	0.0	0.6
2042	12.6	11.8	0.0	5.4
2043	12.4	11.8	0.0	4.4
2044	7.4	11.9	0.0	0.6
2045	10.3	11.9	0.0	2.2
2046	7.5	11.7	0.0	0.6
2047	3.9	11.7	0.0	0.2
2048	10.8	11.7	0.0	3.0
2049	12.2	11.8	0.0	4.4
2050	5.7	12.3	0.0	0.4
2051	14.3	13.0	0.1	6.4
2052	18.1	13.6	2.2	10.9
2053	19.9	13.6	3.9	13.4
2054	14.7	12.8	0.6	7.4
2055	7.5	12.2	0.0	1.0
2056	14.9	11.8	0.6	7.4
2057	15.5	11.7	1.0	8.9
2058	7.3	11.5	0.0	0.6
2059	7.3	11.4	0.0	0.6
2060	8.4	11.4	0.0	1.0
2061	8.7	11.4	0.0	1.8
2062	11.3	11.4	0.0	3.4
2063	17.9	11.3	2.6	11.5
2064	9.8	11.3	0.0	2.6
2065	20.0	11.6	4.2	13.7
2066	8.7	11.3	0.0	1.9
2067	15.9	11.3	1.3	9.5
2068	11.8	11.3	0.0	5.0
2069	13.1	11.2	0.0	6.1
2070	15.5	11.2	0.9	8.1
2071	10.1	11.2	0.0	2.7
2072	9.0	11.3	0.0	1.9
2073	15.5	11.2	1.3	9.6
2074	21.0	11.3	5.0	15.0
2075	9.5	11.3	0.0	2.6
2076	14.9	11.1	0.9	8.2
2077	9.6	11.2	0.0	2.7
2078	11.0	11.2	0.0	3.6
2079	15.9	11.0	1.5	9.8

Table 4.5: The HdM spectrum (71.7 kg y) in the energy interval 1980-2080 keV. The last two columns show the 68.27% C.L. interval for a Poisson signal, with an assumed model background (11.8±0.5 cts/keV at $Q_{\beta\beta}$), which is shown in the third column. Confidence intervals are calculated according to Feldman-Cousins [47, 48]. The starting energy of each 1-keV bin is given.

The total number of counts in the range 2000–2060 keV of the HdM and the model spectra are 759 and 766 counts respectively. The intensity of the peaks, found in the 2000 – 2060 keV region are presented in Table 4.6. The calculated

E [keV]	S_{FC} [counts]	S_{LSQ} [counts]	S_{model} [counts]
2010	26±14	29±9	10.9±0.3
2016	22±15	28±9	13.4±0.3
2022	12±9	9±9	2.6±0.3
2030	9±8	8±9	0
2038	15±12	16±9	0
2053	22±16	23±9	8.0±0.3

Table 4.6: The peak intensities in the region of interest around $Q_{\beta\beta}$ for the weak ^{214}Bi lines and the line at 2039 keV. The second column is the estimation by the Feldman-Cousins method and the third column is the least squares fit in the 1980–2080 keV energy range.

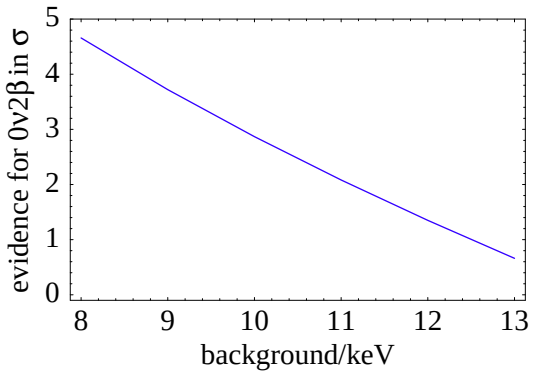

Figure 4.9: The confidence level of the $0\nu\beta\beta$ peak as a function of the background at $Q_{\beta\beta}$ [57].

intensities of the weak ^{214}Bi lines at 2022 and 2053 keV (Tab. 3.7) are consistent with the measured values at 68% C.L.. The significance of the $0\nu\beta\beta$ peak is 1.3σ. This value is in agreement with the independent estimation of the expected statistical significance of the $0\nu\beta\beta$ signal at the assumed HdM background, made by Strumia and Vissani [57] shown in Figure 4.9.

4.5 Limits on the half-life of $0\nu\beta\beta$ decay of ^{76}Ge and the effective neutrino mass

As shown in the previous section, the $\sim 1\sigma$ signal found around the $Q_{\beta\beta}$ value can be classified as $0\nu\beta\beta$ with quite low significance. The half-life of the ^{76}Ge $0\nu\beta\beta$ decay can be determined using Eq. 2.4 and the 2039 keV peak intensity S_{FC} from Table 4.7. The half-life of the neutrinoless double beta decay and the effective neutrino

Method	E_{peak} [keV]	Peak area [counts]
$S_{Feldman-Cousins}$	2039.0	15±12
S_{Fit}	2038.1±1.3	13.0±8.5

Table 4.7: The 2039 keV peak intensity determined with Feldman-Cousins and LSQ methods using background 11.9±0.5 counts/keV.

mass are derived using Eqs.2.4 and 2.2 and presented in Table 4.8. The sensitivity of the HdM experiment for 71.7 kg y, calculated with Eq. 2.5 is $4.6{\cdot}10^{25}$ y (68%C.L.).

Period 1990 ÷ 2003			
Exposure [kg y]	Background, [cts/(keV kg y)]	$T^{0\nu}_{1/2}$ $[y]$ (68% C.L. interval)	$\langle m_{\beta\beta}\rangle$ [eV] (68% C.L. interval)
71.7	0.17	$2.2 \cdot 10^{25}$ $(0.4 - 4.0) \cdot 10^{25}$	0.32 (0.19 - 0.45)

Table 4.8: Half-life of the ^{76}Ge neutrinoless double beta decay and the effective neutrino mass, calculated with the nuclear matrix element (M=4.2) of [37].

4.6 Conclusions

The background model of the HdM spectrum was developed using measurements with sources and MC simulations, which accounts for contributions from ^{226}Ra, ^{232}Th, ^{60}Co and also neutrons with muons. The model deviation from the HdM spectrum is 1% within the 250-2800 keV energy interval. The background continuum in the region of interest around the $Q_{\beta\beta}$ value was determined using the model. The obtained value of the background is (11.8±0.5) counts/keV, which is higher than the background used in publication [14]: (10.0±0.3) counts/keV. The model is still not accounting for all data. However, the fit of the HdM spectrum with the model background gives a better agreement of the ^{214}Bi line intensities. The intensity of the ∼2039 keV peak, (15±12) counts, is less significant than the published value [14] obtained before the model was developed.
The corresponding half-life of the $0\nu\beta\beta$ decay is $2.2 \cdot 10^{25}$ y and the 68% C.L. interval is $(0.4 - 4.0) \cdot 10^{25}$ y. The sensitivity of the HdM experiment for $0\nu\beta\beta$ decay is

$4.6 \cdot 10^{25}$ y (68%, C.L.). The effective neutrino mass is 0.32 eV within the interval (0.19-0.45) eV at 68% C.L., calculated using the nuclear matrix element of [37].

Chapter 5

The GENIUS-TF Setup – Installation of Four HPGe Detectors and Background Measurements

A novel technique to use germanium detectors without a conventional cryostat was proposed by G. Heuser [18] to achieve extreme background reduction. The idea was to operate bare germanium diodes in high purity liquid nitrogen, which serves as cooling medium and clean shielding simultaneously. GENIUS-TF, a test-facility for the GENIUS project [19], was based on this idea. The first spectroscopy measurements with a germanium detector immersed directly in liquid nitrogen were performed in 1997 at MPI-K. According to the GENIUS-TF proposal [20], 16 bare HPGe detectors with a total mass of ∼40 kg would be operated in liquid nitrogen. Finally, the GENIUS-TF setup has run a total of six HPGe detectors during three years (2003–2006) [52, 53, 54, 55].
In this chapter the experimental work concerning the installation of the detector setup and the first year results of GENIUS-TF measurements are presented. An analysis of the GENIUS-TF background after the completion of the external shielding and careful investigation of its origin will also be given.

5.1 The GENIUS-TF setup

The first four GENIUS-TF detectors were produced in 2002 by ORTEC (USA) and then shipped to Germany. To minimize cosmogenic activation they were transported to LNGS to be stored underground until their installation. The diodes were equipped by ORTEC with the ultra-low mass high voltage and signal contacts (∼3 g each) made from stainless steel wire, gold and teflon (Fig. 5.1(left)). The depth of the core of the detectors was reduced to provide lower detector capacity and, consequently,

lower noise. Therefore, a very low threshold, estimated by ORTEC to be around 0.5-0.7 keV, could be achieved. Some characteristics of the 4 detectors, as stated by the manufacturer, are listed in Table 5.1.

On May 5, 2003 the four bare Ge detectors were installed under dust reduced

Detector	GTF1	GTF2	GTF3	GTF4
Serial No.	P41045A	P41044A	P41032A	P41112A
Mass, g	2580	2447	2367	3128
Diameter, mm	87.4	85.3	89.4	85.0
Length, mm	77.2	86.5	71.5	104.5
Core depth, mm	44.1	45.5	38.7	64.6
Operating voltage, V	3000	2600	3200	2500
Depletion voltage, V	1000	700	3100	2000
Leakage current, pA	30	76	85	244
FWHM @ 1.33 MeV, keV	2.0	3.1	1.8	2.0
FWHM @ 122 keV, keV	0.72	0.94	0.80	0.76

Table 5.1: Parameters provided by ORTEC for the four GENIUS-TF HPGe-detectors [58]. The energy resolution and the leakage current were measured with the diodes installed in a vacuum cryostat.

atmosphere into the GENIUS-TF setup. The detectors were positioned in a holder made from high-purity teflon (PA5), as shown in Fig. 5.1 (right). The detector holder is surrounded by a shield made of zone refined poly-crystalline germanium bricks (40 bricks with total mass of 212 kg). The thickness of the germanium shield is 10 cm on all sides and 5 cm on the top and the bottom of the detectors holder. The germanium shield is kept in a thin wall (1 mm) box of high-purity electrolytic copper of the size of $50 \times 50 \times 50$ cm^3, which is filled with $\sim$70 l of liquid nitrogen. The copper box is thermally shielded by 20 cm of special low-radioactivity styrofoam, followed by a shield made out of electrolytic copper (10 cm, 15 tons) and low-radioactivity (Boliden) lead (20 cm, 35 tons). The schematic drawing of the setup is shown in Fig. 5.2. It was partially shielded against neutrons with 20 cm Boron-polyethylene plates on the bottom. The upper part of the shield was completed in November 2003.

The liquid nitrogen, which is in direct contact with the detectors must have a very high purity. It was produced by the BOREXINO nitrogen purification plant - Low Temperature Adsorber (LTA) [59]. Liquid nitrogen of technical quality (99.99% purity) is directly purified in the liquid phase by an adsorber column system filled with about 2 kg of activated carbon. The pure liquid nitrogen was transported from the production plant to the GENIUS-TF building by two 200 l dewars. The filling of the copper container with nitrogen was performed using a filling system made of thermally isolated teflon tubes. The tube leading to the copper dewar was equipped with a valve which was kept closed between the fillings. Due to the evaporation of the liquid nitrogen inside the copper box, GENIUS-TF had to be refilled every two days. The liquid nitrogen level in the detector chamber was

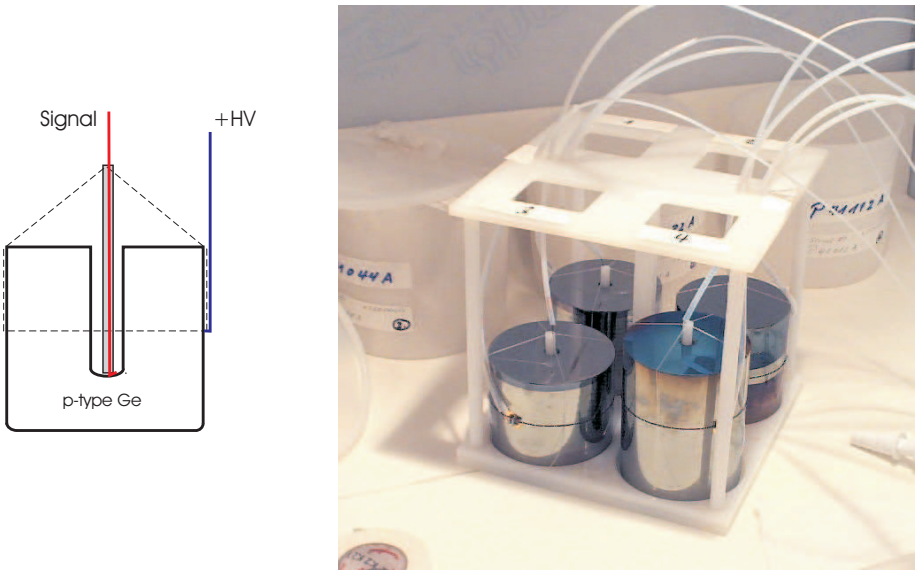

Figure 5.1: The HV and signal cables are connected on the side and central contacts of the diodes, respectively (left). The four first GENIUS-TF bare diodes mounted in the PTFE detector holder (right) [52].

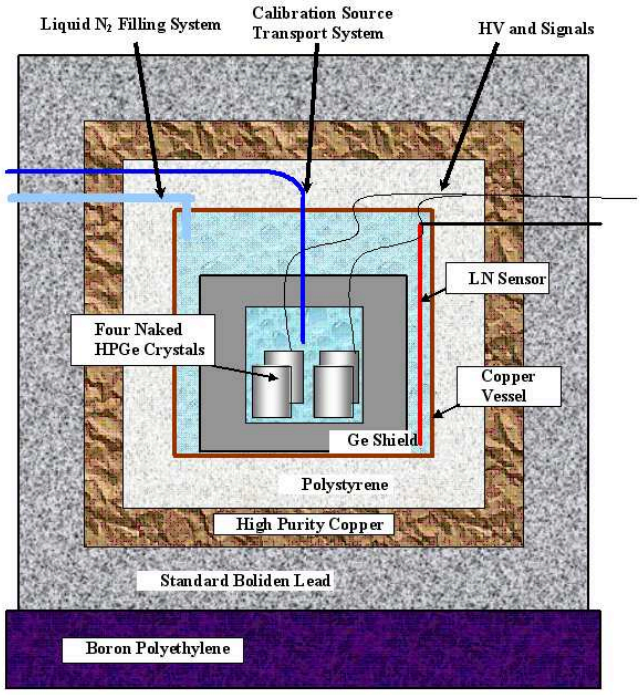

Figure 5.2: Schematic drawing of the GENIUS-TF setup showing the the external and the internal shield as well as the bare germanium detectors in liquid nitrogen [52].

measured by a capacitive sensor. It consists of two 40-cm long isolated coaxial tubes made out of pure copper. The electrical capacity of the sensor depends on the liquid nitrogen filling level. For the capacity measurements the electronics were installed and set according to calibration tests. However, the operation of the capacitive sensor introduces significant noise to the detector electronics, so it was switched off during spectrometry measurements.
The infrared (IR) radiation coming from the upper unshielded part of the setup penetrates through the styrofoam and is partially absorbed by the upper lid of the copper box and the germanium shield. The IR radiation which reaches the diodes creates a significant leakage current when a reverse bias is applied. To reduce the IR radiation in the setup, a copper sheet was temporarily placed over the styrofoam. Then it was possible to apply the operational voltage to the detectors. The copper sheet was removed only after the completion of the setup shield a few month later.
The read out system consisted of a linear amplifier, a Struck Flash ADC (model SIS3301) with a sampling rate of up to 100 MHz and 12-bit resolution and a VME computer [51]. A standard ORTEC MCA was also used for test measurements. The detector calibrations were performed with a ^{133}Ba γ-source with an activity of 401 kBq. The source was fixed on a steel wire inside a teflon tube closed at both ends. The source was introduced into the center of the detector array using a cylinder magnet. Figure 5.3 (top) shows the first spectrum measured with a ^{60}Co source positioned outside the setup, on top of the styrofoam, and with the ^{133}Ba source inside the setup. An increase of the signal noise was noticed when the source was inserted inside the setup, probably because of electro-magnetic pick-ups on the long source wire. The measured energy resolution at 1.33 MeV of ^{60}Co was 7.4 keV with the ^{133}Ba source inserted in the setup, and it improved to 5.1 keV when the ^{133}Ba source was removed. To reduce the noise, the wire was cut and the source was attached to a thin teflon tube. After this modification, the source had to be inserted into the setup manually, because the teflon tube became rigid in liquid nitrogen and the magnet force was not strong enough to pull the source out of the setup. The teflon tube was kept closed between the calibrations but radon contamination of the setup could occurred during calibration measurements.

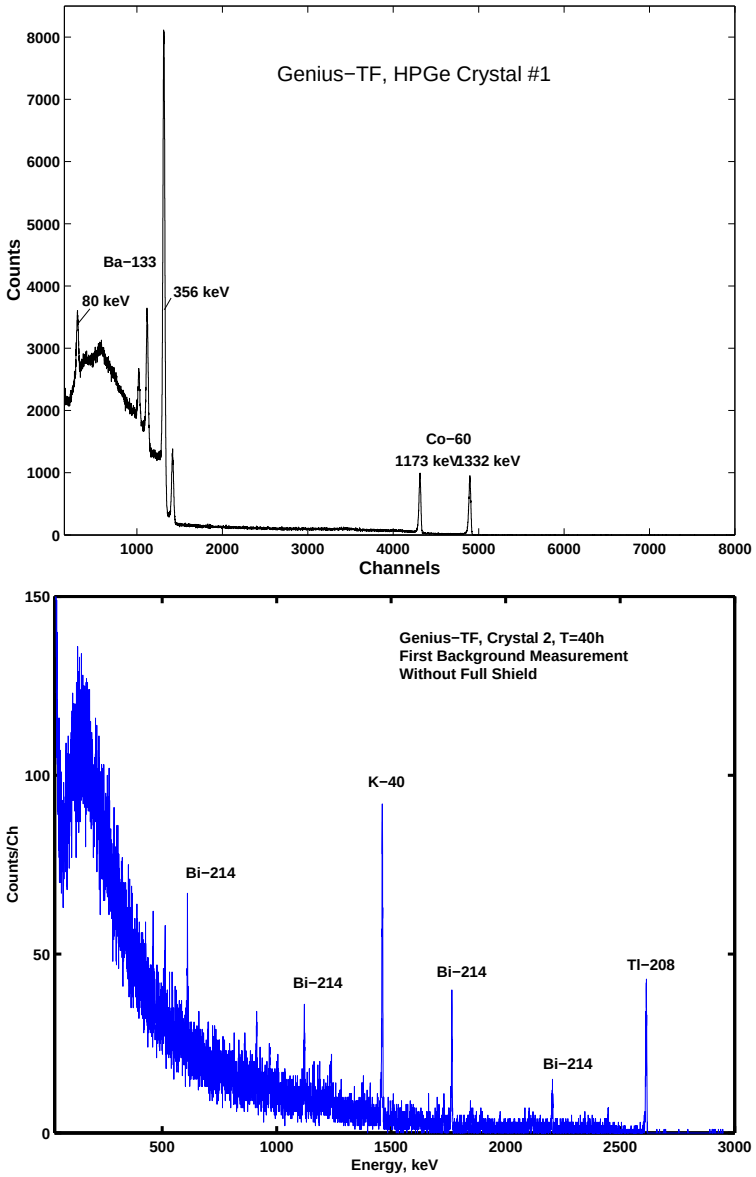

Figure 5.3: Top: first spectrum measured with detector GTF1. The ^{60}Co source is outside, and the ^{133}Ba source is inside the setup. Bottom: first background spectrum measured with detector GTF2 over 40 hours without the full shielding of the setup [52].

5.2 ^{222}Rn contamination

In November 2003 the external shielding of GENIUS-TF was completed using the lead shield from the decommissioned Heidelberg-Moscow experiment. The external radiation was suppressed by $\sim 10^5$ times, while the detector count rates decreased by only a factor of 100. The background was dominated by the internal radioactive impurities in the setup. In Fig. 5.4 a spectrum of the background (live-time = 46

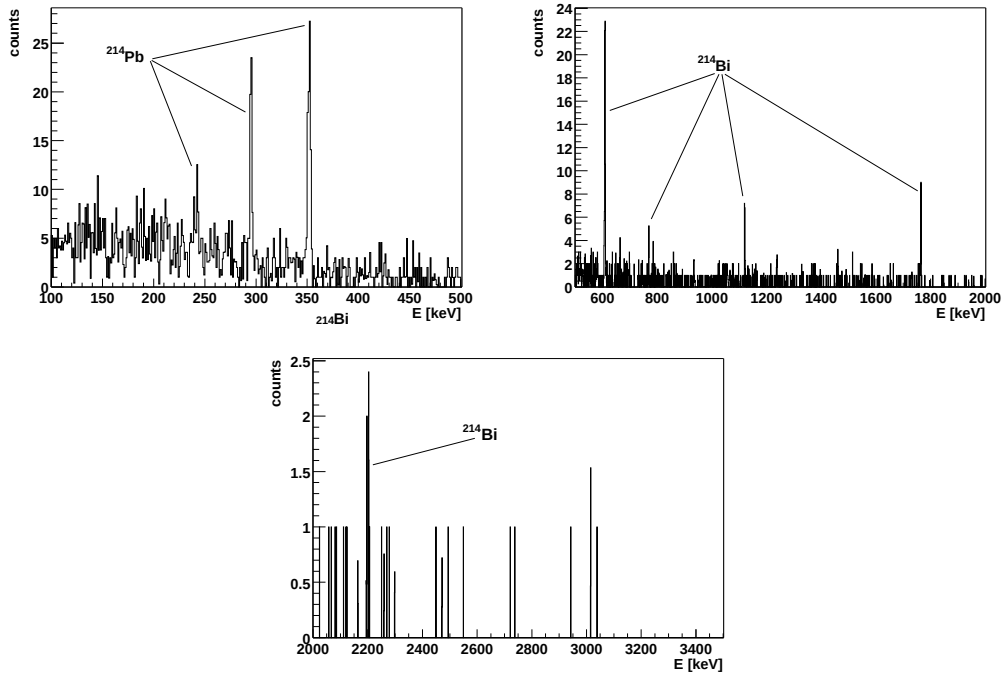

Figure 5.4: Background spectrum measured with GTF2 detector a few days after the completion of the external shielding. Only peaks from ^{214}Pb and ^{214}Bi isotopes (daughters of ^{222}Rn) are visible [53].

hours) measured with the GTF2 detector a few days after the completion of the external shielding is shown. The peaks from the gamma-lines of two isotopes, ^{214}Pb and ^{214}Bi, are presented. It suggests that the peaks originate from the decay of ^{222}Rn, introduced inside the GENIUS-TF setup with liquid nitrogen fillings. ^{222}Rn is the only gaseous component of the ^{238}U decay chain (Tab. 5.2) and, as a noble gas, it has a high diffusion ability. Radon emanates from the rock and the concrete inside the Gran Sasso Laboratory. A high concentration of radon in the Gran Sasso air (20-100 Bq/m^3, [69]) was observed. The liquid nitrogen produced by the BOREXINO-purification plant is especially treated to reduce the radon content by about two orders of magnitude. The radon-content of unpurified nitrogen has been measured to be around 0.1 - 0.3 mBq/m^3 of gas at STP. After the purification, the concentration is reduced to $< 1\mu$Bq/m^3 at STP [59]. The background produced

by a concentration of radon in liquid nitrogen equivalent to 0.5 μBq/m^3 at STP for the four GENIUS-TF detectors setup was simulated and is shown in Fig. 5.5. The number of counts in the strongest peak from ^{214}Pb at 351.9 keV is calculated

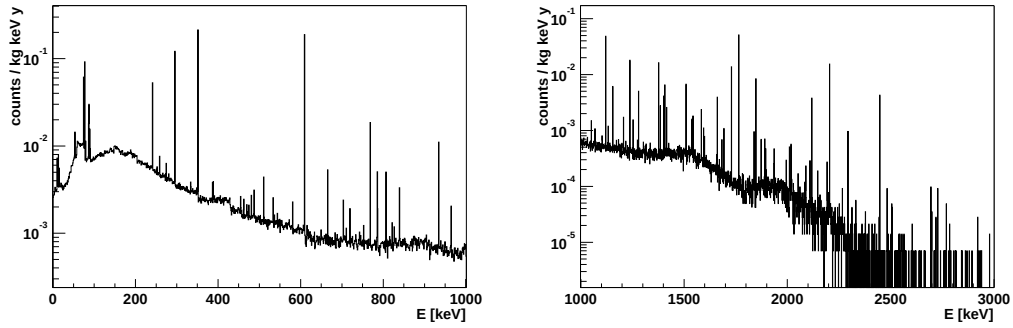

Figure 5.5: GEANT4 simulation of the background in GENIUS-TF setup produced by a radon concentration of 0.5 μBq/m^3 in nitrogen at STP [56].

to be 0.16 counts/(kg y). In the measured spectrum of Fig. 5.4, the count-rate in the 351.9 keV peak is 42 $\pm$ 5 counts/day or $\sim$6·10^3 counts/(kg y). This count rate corresponds to a radon concentration of 20 mBq/m^3. To understand the origin of this contamination, the intensity of the radon background with time was studied. In Fig. 5.6, the number of counts per day observed in the 351.9 keV peak is plotted as a function of time. It was noted that the number of counts from the radon

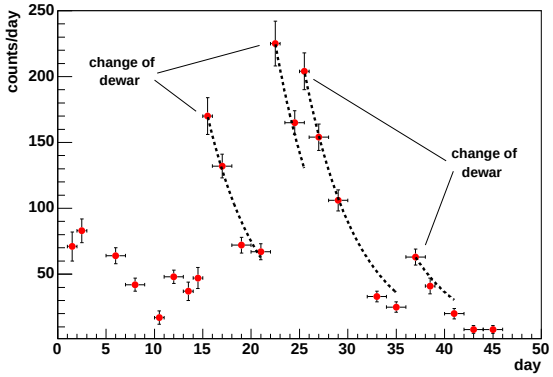

Figure 5.6: Number of counts per day observed in the 351.9 keV peak from ^{214}Pb as a function of time. The dotted lines are fits of the data with the exponents $\exp(-t/\tau)$, where τ = 5.5 d is the ^{222}Rn mean life-time. The measurements were performed with GTF2 detector [53].

daughters was not constant but it increased strongly when the refilling dewar was changed. The GENIUS-TF setup was refilled every two days with liquid nitrogen. One dewar of liquid nitrogen was enough for 3-4 fillings. When the current dewar

Nuclide	Decay mode	Half life	Q [MeV]	Decay products
238U	α	4.468109 y	4.270	234Th
234Th	β-	24.10 d	0.273	234Pa
234Pa	β-	6.70 h	2.197	234U
234U	α	245500 y	4.859	230Th
230Th	α	75380 y	4.770	226Ra
226Ra	α	1602 y	4.871	222Rn
222Rn	α	3.8235 d	5.590	218Po
218Po	α 99.98%	3.10 min	6.115	214Pb
	β- 0.02%		0.265	218At
218At	α 99.90%	1.5 s	6.874	214Bi
	β- 0.10%		2.883	218Rn
218Rn	α	35 ms	7.263	214Po
214Pb	β-	26.8 min	1.024	214Bi
214Bi	β- 99.98%	19.9 min	3.272	214Po
	α 0.02%		5.617	210Tl
214Po	α	0.1643 ms	7.883	210Pb
210Tl	β-	1.30 min	5.484	210Pb
210Pb	β-	22.3 y	0.064	210Bi
210Bi	β- 99.99987%	5.013 d	1.426	210Po
	α 0.00013%		5.982	206Tl
210Po	α	138.376 d	5.407	206Pb
206Tl	β-	4.199 min	1.533	206Pb
206Pb	stable			

Table 5.2: Uranium-238 decay chain [28].

was empty, it had to be disconnected from the filling tubes and replaced. Following the change of the refilling dewar, the number of counts in the radon peaks decreased exponentially as a function of $\sim e^{-t/\tau}$, where t is the number of days after the dewar change and $\tau = 5.5\,\mathrm{d}$ is the mean ^{222}Rn lifetime (Fig. 5.6). No jumps in the count rates were observed after the fillings without change of the dewar. Therefore, the sharp increases in the count-rate could be explained by the radon entering the tubes during the change of the dewar. The air has a high content of ^{222}Rn and this radon could be introduced in the inner copper dewar when the valve was open. To avoid such contamination the tubes were flushed with high-purity gaseous nitrogen before connecting the new dewar. This procedure allowed to reduce the radon content by an order of magnitude. A fit of the 351.9 keV peak from ^{214}Pb in the sum spectrum

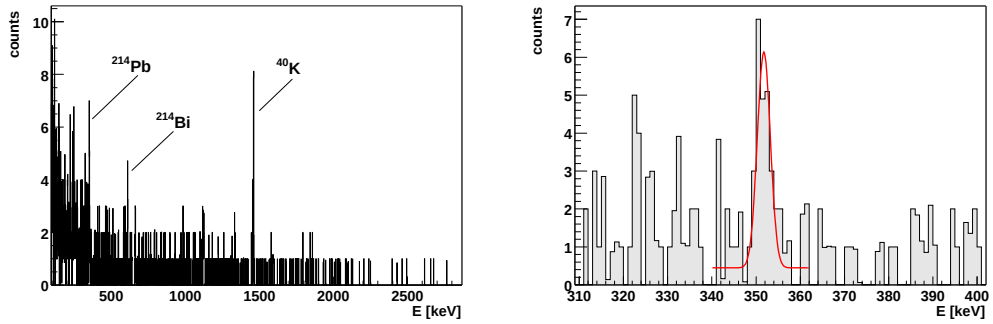

Figure 5.7: Left: sum spectrum of the detector GTF2 from six GENIUS-TF runs. The corresponding lifetime is 8.5 days. Right: fit of the 351.9 keV line from ^{214}Pb in the same sum spectrum [53].

of Fig. 5.7 (right) gives a count-rate of 2.7 ± 0.6 counts/d, averaged over 8.5 days. This count-rate correspond to an initial ^{222}Rn concentration of $\simeq$2.4 mBq/m^3 of gas at STP. A reduction of this rather high level of specific activity can be obtained with an appropriate isolation of the setup from the external air with a radon tight cover, a constant flushing with gaseous nitrogen, an improved filling procedure and an improved calibration system.

5.3 Stability of the GENIUS-TF detectors parameters

The background and calibration measurements presented here were performed during the first year of GENIUS-TF operation. The energy resolutions were determined from the measured spectra collected from May 2003 to May 2004. They were obtained from the strongest lines in the background and the calibration spectra (^{214}Pb-352 keV, ^{40}K-1461 keV, ^{133}Ba-356 keV, ^{60}Co-1332 keV). The long-term stability of the detector energy resolution for these energies is shown in Table 5.3. The bias voltage of the detectors was set to the one recommended by ORTEC, unless the leakage current had increased above 1 nA. In that case, HV was set at 100–200 V below the nominal value. The GTF3 detector bias was initially set to 200 V below depletion voltage, but in April 2004 the detector worked at nominal bias of 3200 V. The resolution of the current measurements of the HV unit ampere meter was 1 nA. Detector GTF1 was temporary disconnected from the DAQ because of high microphonic noise caused probably by the vibrations of its cables in liquid nitrogen. This noise created high trigger rate in the Struck Flash ADC, increasing the DAQ dead time for the other detectors. The microphonic noise is mostly attributed to the detector contacts and the electronic wiring. The variation of the energy resolution of the detectors during the first year of operation were caused mostly by microphonic noise. The first year of GENIUS-TF had demonstrated the possibility of long term operation of bare HPGe detectors in liquid nitrogen without any irreversible deterioration in energy resolution.

	GTF1	GTF2	GTF3	GTF4	E,(keV)
Operating bias [V]	3000	2600	3200	2500	
Depletion bias [V]	1000	700	3100	2000	
FWHM [keV] at ORTEC	2.0	3.1	1.8	2.0	
Date	Actual diodes bias [V]				
05/07/03	2800	2601	3000	2401	
05/07/03	7.2	Off	Off	Off	356
05/07/03	7.4	Off	Off	Off	1332
05/09/03	5.1	4.6	4.9	4.5	1332
05/13/03	7.5	4.2	3.8	5.3	1460
07/26/03	3.8	5.3	6.1	5.4	356
07/26/03	6.0	9.2	11.7	11.8	1332
07/28/03	3.1	5.0	5.2	4.6	356
07/28/03	5.3	8.3	9.7	7.9	1332
07/30/03	5.2	8.2	5.6	7.6	1460
11/27/03	3.0	2.3	5.5	2.4	356
	Actual diodes bias [V]				
12/10/03	2404	2603	2879	2301	
12/10/03	Off	2.4	2.5	2.3	356
12/21/03	Off	2.4	2.7	2.4	352
12/31/03	Off	2.5	2.7	2.4	352
01/02/04	Off	2.6	2.8	2.4	352
01/11/04	Off	3.5	2.3	2.1	356
02/10/04	Off	3.2	Off	3.0	356
02/25/04	Off	2.3	Off	Off	356
03/07/04	3.2	2.0	2.0	2.0	356
03/11/04	5.2	2.8	2.6	2.3	352
04/04/04	2.8	4.0	4.7	2.4	352
	Actual diodes bias [V]				
04/06/04	2600	2220	2879	2301	
04/15/04	4.1	4.0	5.0	2.6	352
04/15/04	4.7	4.7	5.7	3.8	1332
04/26/04	5.5	3.0	4.0	2.3	352
	Actual diodes bias [V]				
05/04/04	2600	2220	3200	2500	
05/19/04	4.4	4.0	3.3	2.7	352

Table 5.3: Energy resolution (FWHM [keV]) of the four GENIUS-TF detectors as a function of time during the first year of GENIUS-TF operation.

5.4 Summary and outlook for GERDA

The GENIUS-TF setup with four HPGe detectors immersed in liquid nitrogen has been presented. The presented work covers the first year of operation from the detectors assembly on May 5 2003, to June 2004 at the Gran Sasso underground laboratory. First measurements showed high sensitivity of the diodes and of the electronics to the environmental interferences: vibrations in liquid nitrogen, electromagnetic pickups and infrared radiation. Special measures were performed to reduce these interferences and an energy resolution of $\sim$4 keV was achieved. The results and analysis of the GENIUS-TF background after the complete assembly of the external shielding were presented. The contribution to the background coming from the ^{222}Rn decay chain was identified. The high background from ^{222}Rn is caused by radon coming from the laboratory air inside the setup during the filling procedure. To eliminate radon influx additional flushing lines, a radon tight copper box and high quality valves were proposed to be installed.
The four first GENIUS-TF detectors were biased at their initial HV during the first year of the GENIUS-TF operation. Their energy resolution did not irreversibly deteriorate, but was highly affected by the microphonic noise. These measurements show principal feasibility of using bare germanium detectors in cryogenic liquids serving as a shield from external radiation. An irreversible deterioration of the GENIUS-TF detectors operating in liquid nitrogen over three years was observed in [54, 55]. This could be attributed to the probable improper handling during the warm-up temperature cycles.

Chapter 6

Measurements of the γ Flux on the GERDA Site at LNGS

6.1 Introduction

The necessary GERDA shielding depends on the intensity of the external radiation. Therefore, the γ-ray flux at the experimental site had to be determined. The GERDA experiment is located underground in Hall A of LNGS, under 1400 m of rock. The rock coverage results in a cosmic ray flux reduction on the order of one million but the uranium, thorium and potassium content in the mountain rock also produce gamma radiation. The concentrations of ^{238}U, ^{232}Th and ^{40}K in the rock and the concrete at LNGS have been measured by the Milan group in 1985 [67]. The authors concluded that the normal rock has very low activity, but there are infiltrations of black marnatic rock which contains much larger radioactivity. These infiltrations are now hidden under a concrete layer of 5-30 cm thickness covering the laboratory walls.
To find a possible anisotropy or local anomalies at the GERDA site, the angular distribution of the gamma flux was first measured in 2004 using an HPGe detector with a collimator. During the 2005-2006 reconstruction of LNGS, the Hall A floor was covered with a new concrete of 30 cm thickness and a layer of waterproof resin. Measurements showed that the activity of the new concrete is higher than the normal LNGS rock by one order of magnitude. Therefore, new γ-ray flux measurements at the site of the GERDA experiment were performed again in 2007. The following sections describe the experimental setups, the calibration procedure and the results of the γ-ray flux measurements.

6.2 Methods of flux determination

The flux of photons Φ is the number of photons per unit time passing through a unit surface area perpendicular to the trajectory of the photons. The full-energy peak count rate N of the detector irradiated with a photon flux $\Phi(E, \theta, \varphi)$ at a given

energy E (Fig. 6.1) is given by:

$$N(E) = \int_{\Omega} \varepsilon(E, \theta, \varphi)\, A_{\perp}(\theta, \varphi)\, \frac{d\Phi(E, \theta, \varphi)}{d\Omega}\, d\Omega \tag{6.1}$$

where $\varepsilon(E, \theta, \varphi)$, the intrinsic efficiency, is the ratio of the counts in the full energy peak to the number of photons hitting the detector surface, $A_{\perp}$ is the projected area of the detector perpendicular to the (θ, φ) direction, and Ω is the solid angle. The detector response (S) is the full energy peak count rate per unit flux at a given photon energy: $S(E, \theta, \varphi) \equiv \varepsilon(E, \theta, \varphi)\, A_{\perp}(\theta, \varphi)$. In general, the flux Φ cannot be obtained by solving the integral equation 6.1. However, if the detector has an isotropic response $S(E, \theta, \varphi) = S(E)$, then the integral is simplified to the product of the detector response and the integral flux, which then equals to:

$$\Phi(E) = \frac{N(E)}{S(E)}. \tag{6.2}$$

The HPGe detector used for the present γ-flux measurements possesses a nearly isotropic response over a wide range of energies, validating the application of the equation 6.2, as will be shown in the section 6.4. The isotropic response of the detector allows a significant simplification of the total flux determination.

The flux can also be calculated using a source distribution. Assuming a uniform

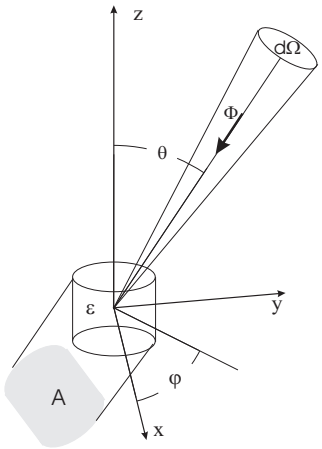

Figure 6.1: Diagram showing the projected area of the detector perpendicular to the flux Φ in the (θ,φ) direction.

volume distribution of the γ-source with intensity n_{γ} $[\gamma/sm^3]$ in the material surrounding a convex cavity (Fig. 6.2) and neglecting absorption inside the cavity, a simple analytical expression of the flux can be derived. The unscattered photon flux $d\Phi$ inside the cavity, at a distance R from the volume element $dV = R^2\, dR\, d\,\Omega$ emitting $n_{\gamma}\, dV$ photons, can be expressed as:

$$d\Phi = \frac{n_{\gamma}\, dV}{4\pi\, R^2} e^{-\mu_E\,(R - R_0)},\ R > R_0. \tag{6.3}$$

The absorption and scattering of the photons are accounted for by the exponential

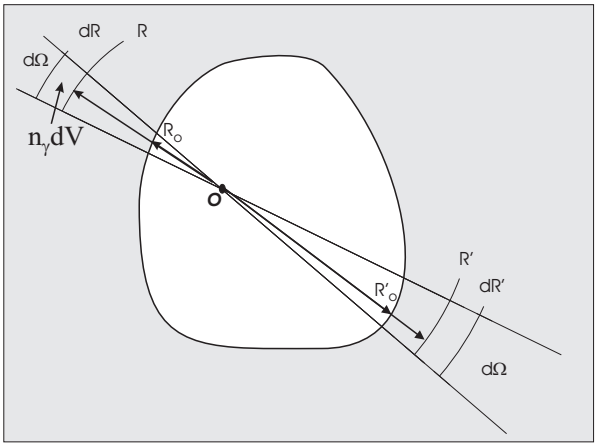

Figure 6.2: Geometry used for the calculation of the flux inside a cavity in a uniform infinite medium with a specific γ-activity (n_γ) and an attenuation coefficient μ_E (equation 6.3)

term $e^{-\mu_E\,(R-R_0)}$, where μ_E is the attenuation coefficient for photons with energy E and R_0 is the distance from the point O to the surface in the $d\Omega$ solid angle direction. The total flux with energy E is given by the integration of the equation 6.3 over $R > R_0$ and a 4π solid angle as follows:

$$\begin{aligned}\Phi &= \int_\Omega \int_{R_0}^{\infty} \frac{n_\gamma}{4\pi\, R^2} e^{-\mu_E\,(R-R_0)}\, R^2\, dR\, d\Omega \\ &= \int_\Omega \frac{n_\gamma\, d\Omega}{4\pi} \int_{R_0}^{\infty} e^{-\mu_E (R-R_0)}\, dR = \frac{n_\gamma}{\mu_E}. \end{aligned} \tag{6.4}$$

In this idealized model the flux is defined by the emitted photon density and the absorption in the surrounding media. The flux is isotropic and uniform inside the cavity. Most of the unscattered photons originate in the surface layer of material with a thickness in the order of μ_E^{-1}(μ_E=10 1/m for E_γ=2.6 MeV in LNGS rock). For example, the thorium activity in the first 10 cm of rock walls produces 63% of the 2.6 MeV photon flux.
The use of equation 6.4 is justified if the flux is isotropic. Flux isotropy measurement at the GERDA site was performed in 2004 using an HPGe detector with a collimator, described in the next section.

6.3 Detector system for *in-situ* γ-flux measurements

For both measurements (2004/2007) a $114\,cm^3$ closed-end coaxial intrinsic germanium detector with a resolution of 2.0 keV FWHM at 1332 keV was used. The diode is housed in an aluminum cap of 7.0 cm outside diameter, which also contains the necessary signal processing electronics. The detector capsule is attached to a electro-mechanical cryogenic cooler. The cryogenic cooler allows measurements without interruptions caused by liquid nitrogen refilling for one month of measurements. For the first measurement in 2004 a collimator was used. The copper collimator was made of inner parts of a shielding from a low-background spectrometer (Fig. 6.3). The parameters of the detector and the collimator are presented in Table 6.1.

Detector Type	ORTEC HPGe 'PopTop' with cryo-cooling
Relative Efficiency	30%
Energy Resolution	2.0 keV FWHM at 1332 keV
Crystal Diameter and Length	50 mm; 58 mm
Collimator Material	Copper
Collimator Dimensions	$20 \times 20 \times 30\ cm^3$
Collimator Well diameter	8 cm
Wall thickness	min. 6 cm, max. 10 cm
Subtended solid angle	1.2 sr

Table 6.1: The HPGe detector and collimator parameters.

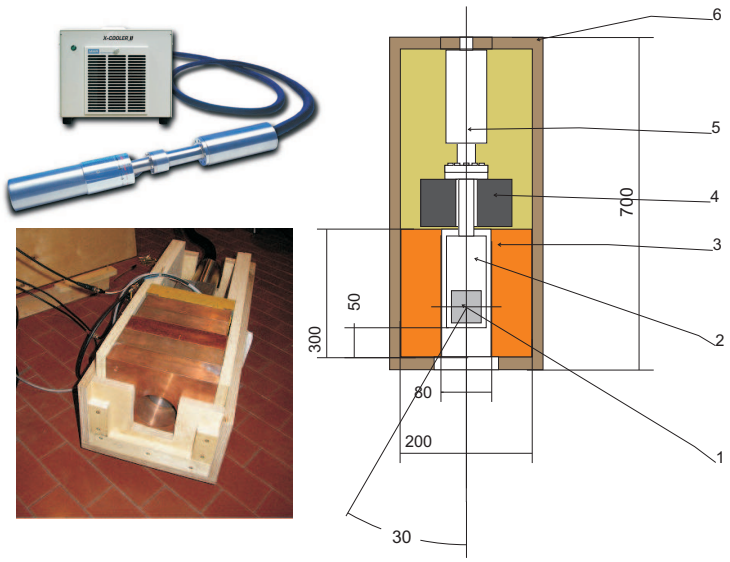

Figure 6.3: The photographs show the HPGe detector connected to the cryogenic cooler (left top), and the Cu collimator assembly (left bottom). Right: diagram of the setup for γ-flux anisotropy measurements with a germanium detector using a collimator: 1) HPGe diode, 2) ORTEC PopTop capsule, 3) copper collimator with a 30° half opening, 4) lead shield, 5) heat exchanger with tubes connected to external portable cryo-cooling system, 6) case.

6.4 The detector system response to γ-radiation

The response of the detector was calculated with Monte-Carlo (MC) simulations. The use of simulations was validated by performing measurements with point-like sources (^{60}Co and ^{226}Ra). The simulations and measurements agree to within 3%, as shown in Fig. 6.4. The MC simulation of the detector response to the parallel photon flux with energies ranging from 350 to 2614 keV was performed using EGSnrc code. The angular response was determined for a detector without (Fig. 6.5) and with (Fig. 6.6) a collimator. As Figure 6.5 shows, for the HPGe detector used in

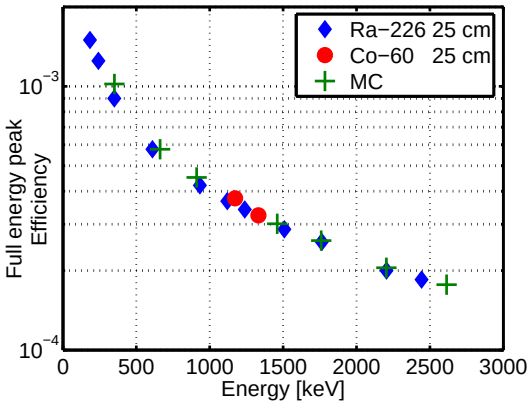

Figure 6.4: Measured and simulated full energy peak efficiencies of the HPGe detector as a function of energy. The ^{226}Ra and ^{60}Co sources were located 25 cm away from the cap of the detector.

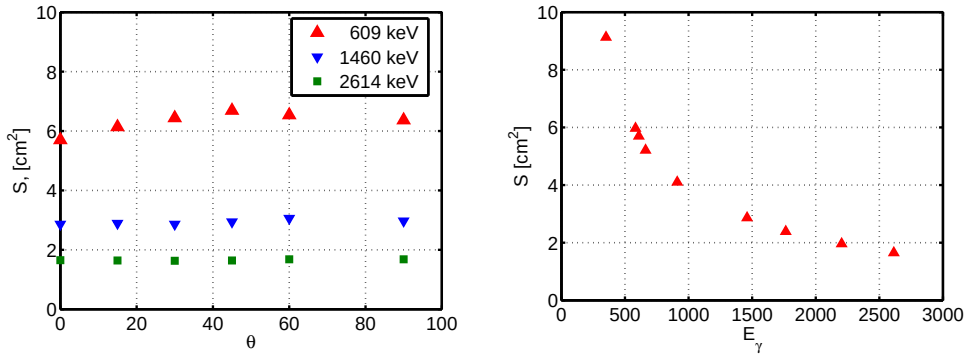

Figure 6.5: Left: Angular response of the HPGe detector without a collimator for a parallel flux of photons determined by MC simulations. Right: Response of the HPGe detector without a collimator as a function of photon energy.

these measurements the response practically does not depend on the direction of the incoming flux. The response varies by 2% for 2614 keV photons coming from all directions. For lower energies (below 500 keV), the variations are mainly defined by the geometrical factor $A_\perp$, which ranges from 20 cm^2 at the front of the detector

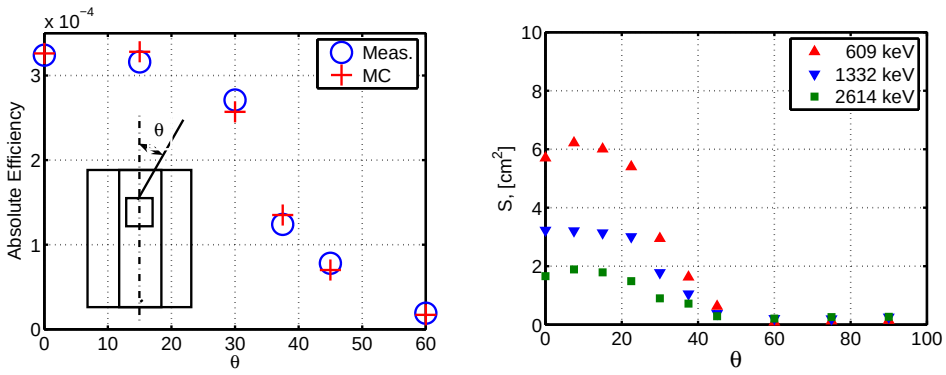

Figure 6.6: Left: Angular dependence of the HPGe detector efficiency with a collimator for 1332 keV photons from ^{60}Co at 25 cm from the cap. Right: Angular response of the HPGe detector with the copper collimator for parallel flux of photons from MC simulations.

to 35 cm^2 at the side, while the intrinsic efficiency remains the same for low energy photons. It is seen in Fig. 6.6 that the simulation with the collimator is also in good agreement with the angular measurements using the ^{60}Co source.

6.5 Measurements in Hall A and results

First *in-situ* measurements of the gamma flux in Hall A at LNGS were done in 2004. The general underground plan of LNGS is presented in Fig. 6.7 [66]. Directional measurements in Hall A were performed by pointing the collimated HPGe detector to the walls, the vaulting and the floor. Each direction was measured for one day. The directional measurements with a collimator were followed by measurements of the background to account for the flux from outside of the collimator opening. The side contribution to the flux was measured by closing the collimator opening with a 10 cm thick copper cylinder. The background was measured for each direction of the collimator. The measured intensities of the background peaks were subtracted from the peak intensities measured with an open collimator. Then, a 15 days long measurement was done without a collimator to determine the total flux. The spectrum is shown in Fig. 6.9. The floor of Hall A in 2004 was partly covered with the massive magnet parts of the OPERA experiment, which was under construction (Fig. 6.8). In 2007 the flux measurements were repeated without a collimator, using the same detector as in 2004. In both cases the detector was placed on a 2.5 m tall scaffold as shown in Fig. 6.8.
The peak intensities and the calculated fluxes (Eq. 6.2) are presented in Table 6.2. The 2614 keV photon total flux is (362±12) m^{-2}s^{-1}. As shown in Table 6.2, the flux of the photons from the ceiling is two times higher than the flux from the walls and the floor. The γ-flux from the direction of the Large Volume Detector (LVD) experiment was greatly suppressed. In 2007, the intensity of the γ-flux from thorium was 20% higher than it was in 2004. However, this difference could be explained by

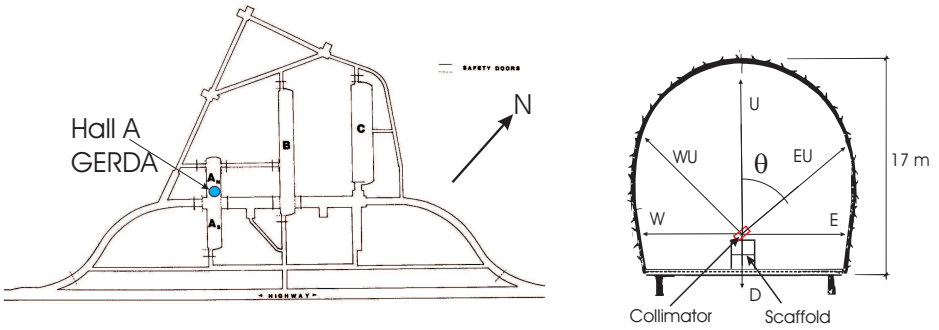

Figure 6.7: Left: floorplan of the LNGS underground laboratory. The location of GERDA in Hall A indicated. Right: the detector for the γ-flux measurements was positioned on a scaffold $\sim$2.5 m above the ground. The angular distribution of the γ-flux was measured with the collimator pointing into the indicated directions, and also to the north and to the south (direction assignments are: W-west, WU-West-Up, etc., θ=0 in zenith).

the absorption in the massive iron parts of the OPERA experiment stored there in 2004. A 662 keV photon flux from anthropogenic ^{137}Cs was measured in 2004 but this flux was undetectable in 2007, probably because of the new layer of concrete on the floor.

Figure 6.8: Setups for the flux measurements in Hall A in 2004 (left) and 2007 (right). In 2004 the massive parts of the OPERA experiment were stored at the same location as GERDA. In 2007 the flux measurements were performed when the bottom plate of the GERDA water tank was installed.

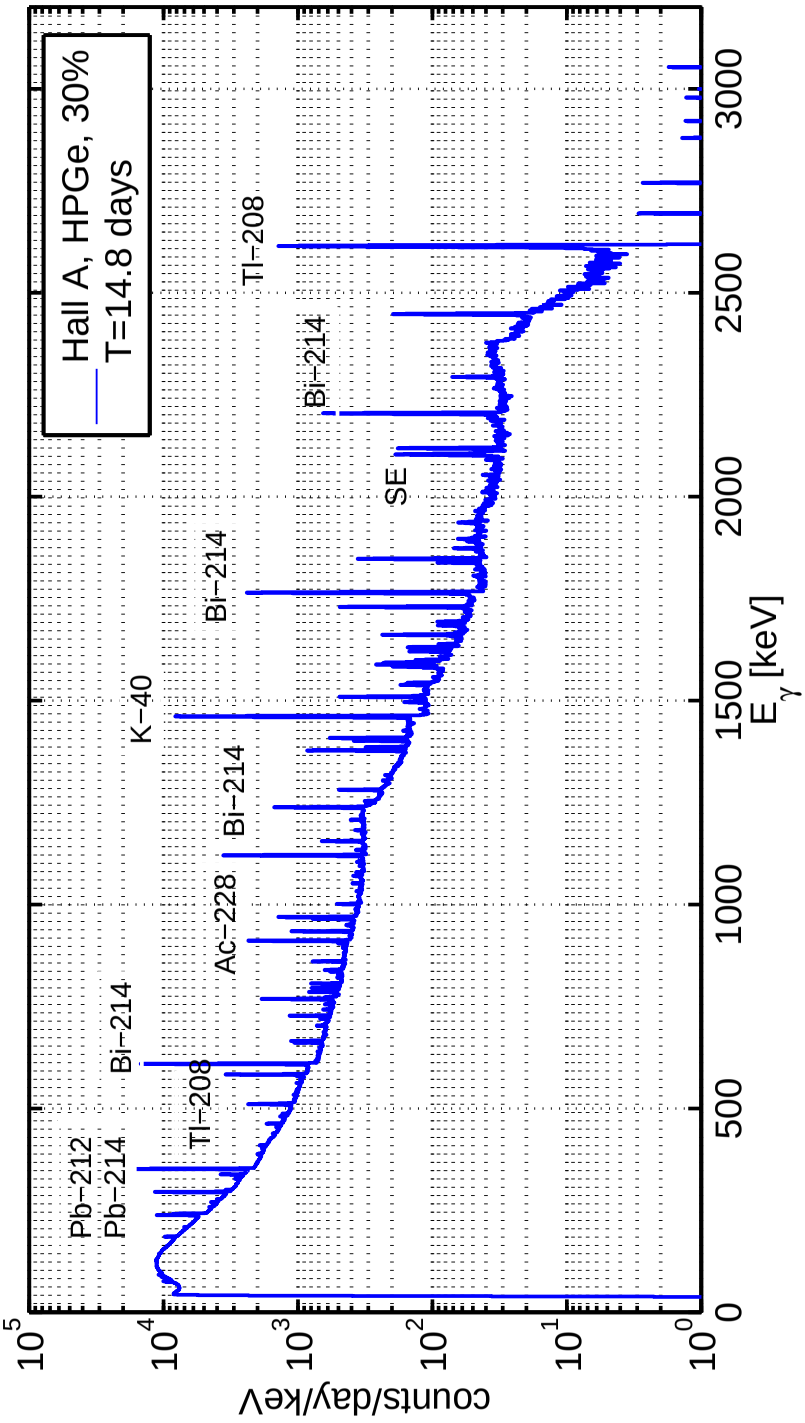

Figure 6.9: HPGe energy spectrum measured without collimation in Hall A of LNGS in 2004.

Nuclide		Tl-208		Ac228	Bi-214			Pb-214	K-40	Cs-137
E_γ, keV		2614	583	911	2204	1764	609	351	1460	662
Det. response, S, [cm^2]		1.65±0.05	6.0±0.3	4.1±0.2	2.0±0.1	2.4±0.1	5.7±0.3	9.1±0.5	2.9±0.1	5.2±0.3
Count rate, $[10^{-3}s^{-1}]$										
August, 2004	N	46.5±0.3	57.5±0.5	46±1	20.1±0.4	70±1	301±1	319±2	234±1	8.6±0.6
Flux, [γ/m^2 s]	Φ	284 ±10	96±7	112±6	101±7	292±20	528±37	351±16	807±45	17±2
Count rate, $[10^{-3}s^{-1}]$										
November, 2007	N	59.8±0.9	64.7±1.2	56±1	23.9±0.6	83±1	311±2	318±3	267±1	<0.4
Flux [γ/m^2 s]	Φ	362 ±12	108±8	137±7	120±8	346±24	546±40	349±16	921±50	<1
South, CRESST	N	3.0±0.4	4.3±0.9	1.4±0.8	1.7±0.3	6.3±0.5	22±3	40±1	13±1	6.4±0.6
θ=90, $\Omega = 1.2$ sr	Φ	18±3	7±2	3±2	9±2	26±2	39±5	44±1	45±3	12±1
North, LVD	N	0.6±0.8	1.4±1.4	1.1±1.5	0.2±0.4	2.0±0.7	11±2	17±4	2.7±1.0	4.2±0.8
θ=90, $\Omega = 1.2$ sr	Φ	4±5	2±2	3±4	1±2	9±3	19±4	19±5	9±4	8±2
East	N	2.5±0.4	3.6±1.1	2.4±1.1	2.4±0.4	8.5±0.6	46±1	47±2	13±1	<0.6
θ=90, $\Omega = 1.2$ sr	Φ	15±3	6±2	6±2	12±2	36±3	81±2	52±2	46±4	<2
West	N	3.5±0.5	6.1±1.3	3.6±1.0	2.5±0.4	10.0±0.7	49±2	70±2	19±1	4.6±0.7
θ=90, $\Omega = 1.2$ sr	Φ	21±3	10±2	9±2	12±2	42±3	86±4	77±2	66±4	9±1
East-Up,	N	3.6±0.6	4.2±1.8	2.7±1.3	2.8±0.7	5.9±0.8	30±2	34±3	24±1	3±1
θ=45, $\Omega = 1.2$ sr	Φ	22±4	7±3	7±3	14±4	25±4	53±4	37±4	84±5	7±2
West-Up	N	6.0±0.5	7.6±2.0	2.3±1.5	2.9±0.5	9.0±0.6	30±3	55±1	27±1	<0.6
θ=45, $\Omega = 1.2$ sr	Φ	36±4	13±3	6±4	15±3	38±3	53±4	60±1	94±5	<2
Up,	N	8.1±0.6	13.0±1.6	9.3±1.4	2.3±0.6	9.0±0.9	38±3	45±3	30±2	<0.7
θ=0, $\Omega = 1.2$ sr	Φ	49±4	22±3	23±4	12±3	38±4	67±4	49±3	105±8	<2
Down,	N	4.5±0.5	9.4±1.5	4.3±1.2	1.7±0.5	5.7±0.7	26±2	38±3	26±1	<0.6
θ=180, $\Omega = 1.2$ sr	Φ	27±3	16±3	11±3	9±2	24±3	46±4	42±3	91±4	<2

Table 6.2: The full energy peak count rates $N, [10^{-3}s^{-1}]$ of the major gamma rays and their fluxes Φ, $[m^2\,s]^{-1}$ in Hall A as measured in 2004 and 2007. The directional measurements were performed in 2004. Intensity and flux are given with 1σ error.

6.6 Calculation of the flux from the natural radioactivity in Hall A

The concentrations of ^{238}U, ^{232}Th and ^{40}K in the Hall A rock samples have been measured by the Milano group [67] in 1985. The authors concluded that the normal rock has very low activity (an order of magnitude lower than granite rock from the Alps). Infiltrations of black marnatic rocks have much higher activity, as shown in Table 6.3. The high activity areas constitute, however, only one percent of the total surface of the Hall A walls. The contamination of concrete at the GERDA site was measured before the beginning of GERDA construction.

The flux can now be determined independently using equation 6.4 for an idealized

	^{232}Th [Bq/kg]	^{238}U [Bq/kg]	^{40}K [Bq/kg]
Hall A normal rock	$\lesssim$0.5	$\lesssim$8	$\lesssim$5
Hall A infiltration rock (average)	8.7±0.4	91±23	248±16
Hall A concrete	10±1	8±1	90±10
Hall B rock	0.25±0.08	5.2±1.3	5.1±1.3
Hall C rock	0.27±0.10	8.2±1.7	2.9±1.4

Table 6.3: Activity of rock and concrete in the Gran Sasso tunnel [67, 68].

case of a uniform source distribution using the measured contamination concentration. The flux Φ is expressed as:

$$\Phi = \frac{n_\gamma}{\mu_E} = \frac{\eta\, A/\rho}{\mu_E} \tag{6.5}$$

where A [Bq g^{-1}] is the specific activity, η is the number of photons per decay and μ_E [cm^{-1}] is the attenuation coefficient for photons with energy E (μ_E=0.1 cm^{-1} for E$_\gamma$=2.6 MeV in LNGS rock). The density ρ of the LNGS rock is 2.7 g cm^{-3} and the density of the concrete is 2.3–2.5 g cm^{-3} [70]. The average activity of the surrounding material was calculated as a mean of the normal rock and the new concrete activity. The resulting flux is presented in Table 6.4. The calculated fluxes are similar to those

Parent Nuclide	Th-232		U-238			K-40
Average Activity	5 Bq/kg		8 Bq/kg			45 Bq/kg
Nuclide	Tl-208		Bi-214		Pb-214	K-40
E_γ, keV	2614	583	2204	609	351	1460
Calculated flux, $[m^2\, s]^{-1}$	450	190	100	470	300	1000
Measured flux, (Tab. 6.2)	362 ±12	108±8	120±8	546±40	349±16	921±50

Table 6.4: Calculated and measured in 2007 fluxes of photons from natural radioactivity in Hall A.

obtained from direct measurements, but the accuracy of the calculated flux is limited by the high variability and uncertainty of the natural contamination in the rock.

6.7 Contribution of scattered photons to the total flux

The analysis of the count rate of full energy peaks has yielded so far the flux of just the unscattered photons. The total γ-flux, which includes also scattered photons continuum was determined with a Monte-Carlo simulation. The photons were simulated uniformly in the 0.5 m concrete slab, and the flux was determined at 5 m from the slab in the air. The EGSnrc simulation code [83] was used. The spectra of the flux for photons with an initial energy of 609, 1460 and 2614 keV are shown in Fig. 6.10. The fraction of unscattered photons in the total flux is about 30%. The scattered photons with energies above 2039 keV contribute to the continuum background around the $Q_{\beta\beta}$ value of neutrinoless double beta decay of ^{76}Ge. Their fraction is about 5% of the total primary flux. The fraction of the scattered photons will change inside the GERDA shield as was shown with the detailed MC calculations of the full GERDA setup [71, 72].

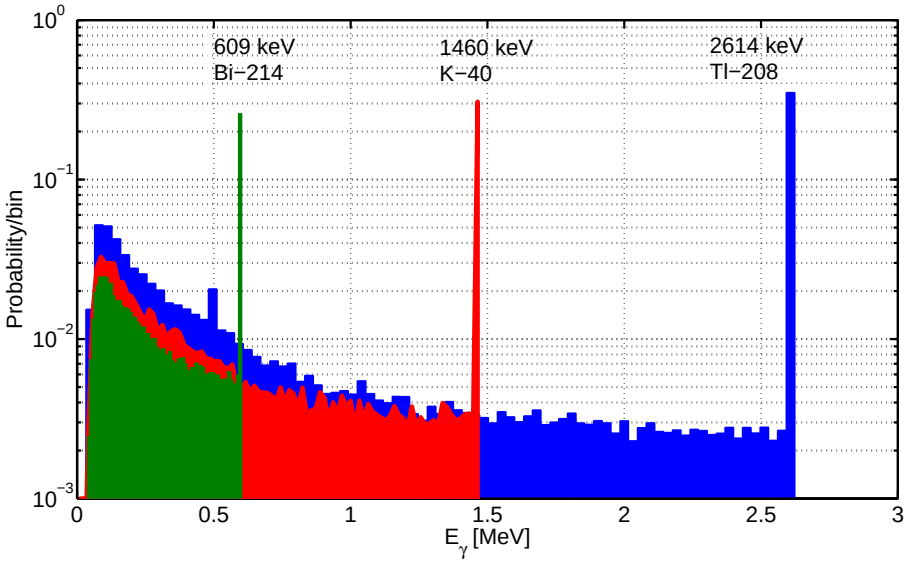

Figure 6.10: Monte Carlo probability distribution of the photon flux energy in air at 5 m from a radiative concrete slab of 0.5 m thickness for the 609, 1460 and 2614 keV primary photons. Each spectrum contains one hundred bins.

6.8 Summary

The shielding needed for the GERDA experiment depends on the intensity of the external radiation. The γ-ray flux at the GERDA experimental site has been determined for the first time in 2004 with a collimated spectrometer. The flux had to be remeasured in 2007 after the reconstruction of the Hall A. An HPGe detector was used to perform these measurements with and without a collimator. The collimator

was used in 2004 for angular flux distribution measurements. The detector response was determined with Monte-Carlo simulations. The detector sensitivity was found to be almost isotropic, which allowed simple flux calculations.
The spectra in Hall A were measured and the fluxes were calculated. The 2614 keV photon flux is $(362 \pm 12)\,\mathrm{m^{-2}s^{-1}}$. The flux of the photons from the ceiling is two times higher than the flux from the walls and the floor. It was found that the intensity of the γ-flux from thorium was 20% higher in 2007 than in 2004. The difference could be explained by the absorption in the massive iron parts of the OPERA experiment stored there in 2004.
The flux was also determined with a simple model of a uniform source distribution in the rock, and using measured concentrations of ^{238}U,^{232}Th and ^{40}K. The calculated flux is similar to the numbers given by the direct measurements, but the accuracy of the calculated flux is limited by the high uncertainty on the measured radioactivity concentrations.
Based on the flux measured with the collimated and uncollimated detector, the contribution of the GERDA background index for the external γ-radiation has been calculated as $1.1 \cdot 10^{-5}$ $[\mathrm{keV\,kg\,y}]^{-1}$ [72]. Details of the external GERDA shielding were optimized based on these measurements. A lead shield, which was originally conceived to reduce the radiation from the concrete floor and ceiling, could for example be omitted.

Chapter 7

Characterization of the HdM and IGEX detectors for GERDA Phase I

The enriched diodes from the past HdM and IGEX experiments were produced in the period from 1990 to 1995. Because the detector parameters might change with time, all the enriched detectors have been characterized prior to the refurbishment for GERDA. Leakage current, counting characteristic and energy resolution have been measured as a function of the applied bias voltage. The active mass of the GERDA Phase-I enriched detectors, which defines the sensitivity of the experiment, has been determined. This chapter summarizes the operations and measurements carried out with the enriched detectors in the GERDA underground detector laboratory (GDL) in preparation for GERDA Phase I.

7.1 Overview

The five HdM and the three IGEX detectors have been kept underground at LNGS and at Canfranc laboratory since the end of the experiments. The detectors were then moved to GDL for maintenance and characterization. Subsequently the cryostats were opened and the diodes were taken out. The dimensions and the masses of the diodes as well as the dimensions of the cryostats have been measured. The diodes were stored under vacuum in special containers and were transported to the High Activity Disposal Experimental Site (HADES), Geel, Belgium, in which the Institute for Reference Materials and Measurements (IRMM) operates a laboratory 233 m below ground. In preparation for GERDA Phase I, the enriched diodes are being reprocessed to the Canberra type, which have more reliable contacts than the ORTEC ones. The detectors were reprocessed at Canberra Semiconductor NV, Olen, near HADES. During the refurbishment process, the diodes were stored underground in HADES in between the refurbishment steps.
The active mass of a germanium detector is the mass of the volume within which

energy depositions result in detector signals. A p-type HPGe detector has the n^+-contact on its outer side, which is a thick ($\sim$1 mm) conductive layer, insensitive to radiation, also known as the dead layer. This contact is created by diffusion of lithium on the surface of the germanium crystal. During extended storage at room temperature, the lithium diffuses into the germanium, increasing the dead layer thickness and reducing the active mass of the detector. Detection efficiency was measured with sources and the results were compared to Monte-Carlo simulations. Based on these results, the active masses have been determined and compared to the previous values.

7.2 Operations and measurements

7.2.1 Spectrometry parameters

The leakage current, the count rate in the full energy peaks and the energy resolution were measured as a function of the applied bias voltage (HV). The HdM and IGEX detectors were equipped with resistive feedback charge sensitive preamplifiers CANBERRA Model 2002C and Princeton GammaTech Model RG11, respectively. A simplified scheme of the first stage of the preamplifier (Fig. 7.1) shows how the leakage current I_d can be derived from the test point voltage (TPV) measurements as follows,

$$I_d = \frac{TPV(HV) - TPV(0)}{R_f}, \tag{7.1}$$

where R_f is the resistivity of the feedback resistor (2 GΩ).

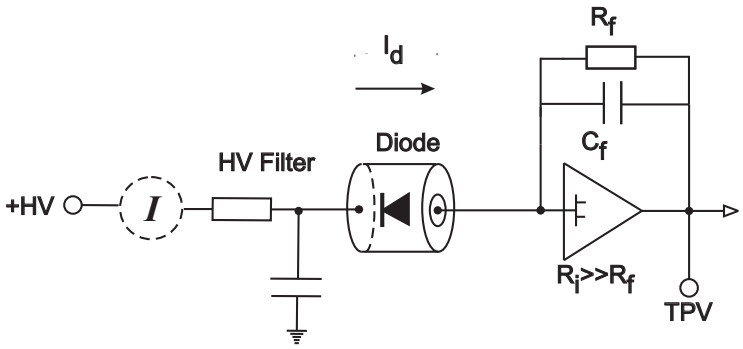

Figure 7.1: A simplified scheme of the diode connection to the first stage of resistive feedback charge sensitive preamplifier. The TPV depends linearly on the feedback resistor R_f and the detector current I_d. An amperemeter was used optionally.

The leakage current was also measured directly. This was done with a precision of $\pm$10 pA using an amperemeter, connected to the HV side of the diode (see Fig. 7.1).

Calibration Source	Certified Activity kBq (01.06.1990)	Activity kBq (08.02.2005)	Uncertainty 3σ
^{60}Co (1173.2, 1332.5 keV)	419.9	61.44	3%
^{133}Ba (80, 356 keV)	454	172.2	5%

Table 7.1: Activities of the ^{60}Co and ^{133}Ba calibration sources used for detector characterization.

The picoamperemeter was made of a commercial voltmeter placed in a case with HV isolation from the ground, which was reading the voltage drop on a 100 MΩ resistor. The leakage currents measured with both methods provided comparable results, but the TPV measurements are more accurate (±2 pA).
The operational voltage of the detectors has been determined. The operational voltage is the voltage to be applied to obtain saturated peak count rate with the best energy resolution. In order to obtain good energy resolution, the leakage current must be as low as possible ($\lesssim$100 pA) to minimize the shot noise of the detector.
ORTEC model 659 high voltage power supplies, model 672 amplifiers, and model 919 Multichannel Buffer ADC modules were used for the measurements. Data were recorded and analyzed with the GAMMA VISION program.
^{60}Co and ^{133}Ba sources were used for efficiency and dead layer measurements. The sources were enclosed in plastic cases of 1 mm thickness. The parameters of the sources are presented in Table 7.1.

7.2.2 Using heating and pumping cycles for cryostat vacuum restoration

Sometimes an HPGe detector shows high leakage current and consequently deteriorated energy resolution. The reason is often poor vacuum in the detector cryostat. In order to improve the spectroscopic performance of such detectors, thorough heating and simultaneous pumping of the cryostat is recommended as a common practice for HPGe detectors. The pumping station, including a PFEIFFER oil free forepump and a turbo pump, was assembled and tested. The heating was performed using boiling water. This procedure allows to keep the temperature of the cryostat constant, while avoiding its overheating. Several heating-pumping cycles have been performed with all IGEX detectors and the ANG1 detector. The dipsticks of the IGEX cryostats were put into the boiling water. The cryostat of the ANG1 detector was heated with boiling water inside the dewar. The heating process was continued until the vacuum stabilized at a pressure of typically 10^{-6} mbar. After each pumping-heating cycle, the detectors were cooled with liquid nitrogen for at least two days before measuring the detector parameters.

7.3 HdM detectors

The original parameters of the HdM enriched detectors are presented in Table 7.2. The detectors were produced by EG&G ORTEC, Tennessee, USA. They are named historically as ANG – "angereichert" – and numbered from 1 to 5. From 1990 to 1995, the five detectors were installed in the HdM experiment setup at LNGS. Between 1995 and 2006 all HdM detectors stayed underground.

	ANG1	ANG2	ANG3	ANG4	ANG5
Crystal grown at EG&G ORTEC	11.04.90	07.02.91	21.03.91	11.11.93	06.10.93
Diode completed	12.07.90 *	13.02.91	19.07.91	12.01.94	10.11.93
Serial Number	b8902	P40239A	P40270A	P40368A	P40496A
Diameter, mm	58	80	78.5	75	78.8
Length, mm	68	108	93.5	100.5	105.7
Hole Diam., mm	8	8	9	8	8
Hole Length, mm	43	94	81.5	88.9	93.5
Total Mass, g	980	2905	2447	2400	2781
Enrichment ^{76}Ge	85.9±1.3%	86.6±2.5%	88.3±2.6%	86.3±1.3%	85.6±1.3%
FWHM (1332 keV)	1.99 keV	1.99 keV	1.99 keV	1.99 keV	2.29 keV
Operating Bias, V	+4000	+4000	+3500	+3000	+2500
Leakage Current	no info	138 pA	7 pA	301 pA	8 pA
Impurities/cm^3	no info	no info	$0.5 \div 1.3 \cdot 10^{10}$	$4.1 \div 9.8 \cdot 10^9$	$1.4 \cdot 10^9$
Installed in LNGS	07.90; 01.91	09.91	08.92	01.95	12.94
Moved to GDL	29.09.04	29.09.04	29.09.04	29.09.04	29.09.04

Table 7.2: History and original parameters of the HdM detectors prior to the handover to the GERDA collaboration [29, 31, 32, 33, 34]. (*) Detector ANG1 was completed at Canberra Semiconductor NV.

All diodes were transported from USA to Germany by ship to minimize the cosmic ray exposure. ANG1 crystal ingot was pulled in April, 1990. After two trials, the ANG1 diode was completed at Canberra Semiconductor NV, in July, 1990. In both trials the detector was transported by plane. Total irradiation time in flight was 24 hours [30]. The measured ANG1 diode mass in GDL is 968.7 g, which is 11.3 g less then was reported by ORTEC (Table 7.2). The difference is due to the additional machining of the diode at Canberra Semiconductor NV in 1991 after the damage of the detector cryostat [31]. The ANG2 diode mass measured in GDL is 2878.3 g, which is 26.7 g less then was reported by ORTEC (Table 7.2). The reason for this difference is unknown. All the other detectors have masses within one gram of the ones reported by ORTEC.
On September 29, 2004, the enriched detectors were handed over from HdM to GERDA and transferred to the LUNA1 underground experimental site at LNGS, where their spectrometric parameters and leakage currents have been measured. Unlike the other HdM detectors, ANG1 was handed over warm, without liquid nitrogen in its cryostat dewar. After cooling down, ANG1 showed a high leakage current (∼0.8 nA) and deteriorated energy resolution (∼4 keV FWHM at 1332 keV). Normal resolution and leakage current were measured with ANG2-5(∼2–3 keV). The

ANG2 detector showed sporadic jumps of the full energy peak position of ±10 keV. During the period from December 2004 to November 2005, the detectors were moved three times between the LUNA1 and the LENS sites because of the transformation of the LENS site into the GDL. After each relocation of the detectors, measurements of their spectrometric parameters were repeated. As of February 2005, the HdM detectors were permanently located in the GDL. The instability of the peak position of ANG2 was not observable anymore. To reduce the leakage current of ANG1, a

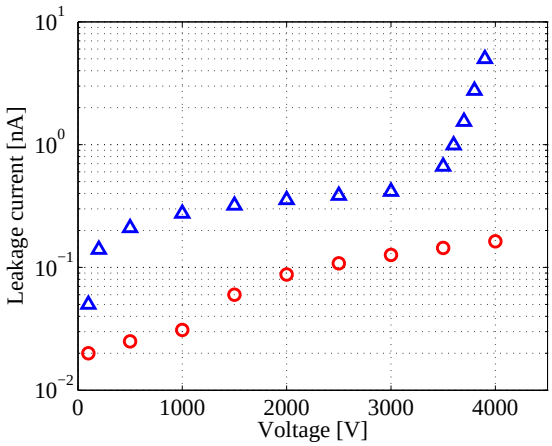

Figure 7.2: Leakage current for ANG1 detector before (△) and after (○) heating and pumping procedure.

heating-pumping cycle was performed. After 10 hours of heating and 24 hours of pumping, the leakage current decreased as shown in Fig. 7.2 and an energy resolution of 2.5 keV FWHM at 1332 keV has been obtained. In April 2006, ANG1 diode was dismounted from its cryostat, its dimensions and mass were measured and it was stored in a special container. Then, on August 18, ANG1 was tested in the radon free

Date Location Detector, FWHM	1995 HdM setup [34] [keV]	30.09.04 LUNA1 [keV]	12.02.05 LENS(GDL) [keV]	18.12.05 GDL [keV]
ANG1	**2.2**	4.0 (3000 V)	2.7 (3000 V)	**2.5**
ANG2	**2.4**	2.4	2.3	**2.3**
ANG3	**2.7**	3.1	2.5	**2.9**
ANG4	**2.2**	2.4	2.5	**2.5**
ANG5	**2.6**	2.9	2.8	**2.6**

Table 7.3: The chronology of the energy resolution (FWHM) at 1332 keV of the HdM detectors measured prior to their refurbishment at Canberra Semiconductor NV. The measurements were performed at the operating voltage (Tab. 7.2) at different locations at LNGS. The standard error of FWHM is 5%.

test bench of GDL. It was mounted in the new low mass holder and inserted in liquid argon. The leakage current, ∼1 nA at 3000 V, increased up to 3 nA within two days.

An energy resolution (FWHM) at 1332 keV of 3.76 keV was measured at reduced (3000 V) bias. The operational voltage (4000 V) was not reached because of a steep increase of the leakage current. Finally, on August 21, ANG1 was transported in 26 hours by a courier car to HADES underground laboratory for the refurbishment at Canberra Semiconductor NV.
In November 2006, the spectroscopic parameters of ANG2,3,4 and 5 detectors were measured for the last time before the opening of the cryostats. Table 7.3 summarizes the energy resolution FWHM history of the HdM detectors. Figure 7.3 shows the detector leakage currents, the 1332 keV peak count rates and the energy resolutions as a function of the applied bias for ANG1-5 detectors. The peak count rate is normalized to one. The detectors leakage currents at the operational bias ranged from 0.2 to 1.2 nA and FWHM ranged from 2.3 to 2.9 keV. As expected, the high leakage current ($\sim$1 nA) of the ANG3 detector causes an increase of FWHM due to the higher shot noise contribution.

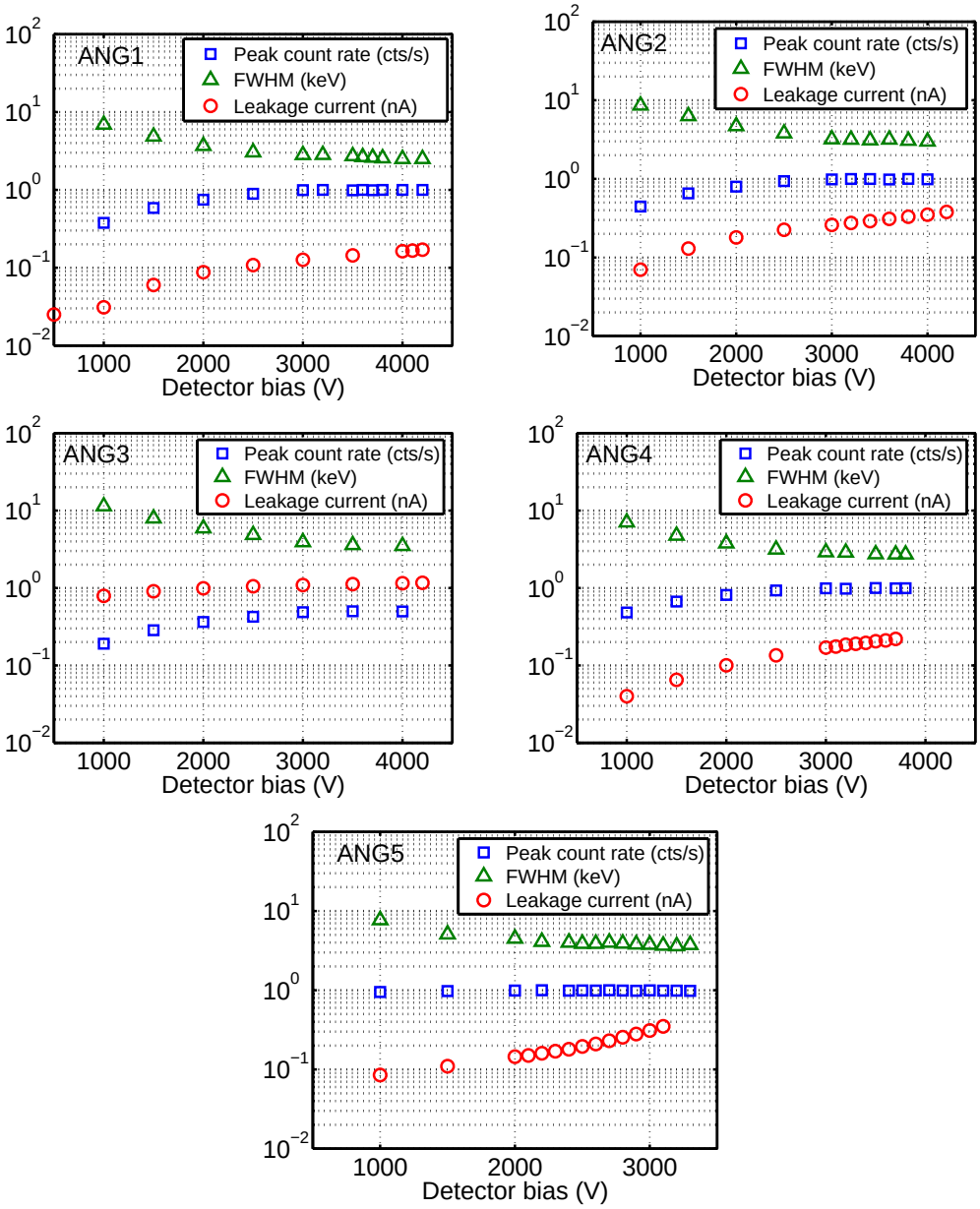

Figure 7.3: The leakage current, the energy resolution (FWHM) and the count rate of 1332 keV peak of the HdM detectors vs. HV bias. Measurements were performed in GDL at LNGS.

7.4 IGEX detectors

Three enriched IGEX detectors were transported in 19 hours by a courier car from Canfranc underground laboratory, Spain, to the LNGS on November 18, 2005. The activation of the germanium crystals by cosmic rays was negligible (the cosmic ray activation rate of Ge at sea level is ∼1 nucleus/day/kg [63, 64]). The detectors were stored underground in the GDL, immediately after arriving at the LNGS. The history and the specification of the IGEX detectors are presented in Table 7.4.

	RG1	RG2	RG3
Crystal grown at Oxford Inc., Oak Ridge, USA	25.09.93	16.02.94	01.12.94
Detector completed	02.11.93	10.05.94	15.04.95
Serial Number	28005-S	28006-S	28007-S
Diameter and Length, mm	77.6; 84.3	78.6; 84.0	79.2; 82.5
Total Mass, g	2149.9	2194.0	2121.0
Dead Layer, μm	∼800	∼800	∼500
FWHM at 1332 keV, keV	2.16	2.37	2.13
Operating Voltage, V	+5000	+4000	+3800
Installed in Homestake	09.11.93	22.05.94	N.A.
Removed from Homestake	15.06.97	27.12.96	N.A.
Installed in Canfranc	15.07.97	25.01.97	10.05.95
Moved from Canfranc to GDL at LNGS	18.11.05	18.11.05	18.11.05

Table 7.4: History and specifications of the three IGEX detectors [61].

The IGEX detectors were stored without cooling for a prolonged period of time (∼2 years) in the Canfranc underground laboratory. The vacuum levels in the cryostats were unknown. Therefore, before cooling the detectors at LNGS, a thorough heating and simultaneous pumping of the cryostats was needed. After the first pumping-heating cycle, the vacuum in the cryostats of RG1 and RG3 was stable at $4{\cdot}10^{-6}$ mbar and the detectors showed good energy resolution. On the other hand, RG2 detector showed degraded energy resolution (∼10 keV FWHM at 1332 keV). Using a PFEIFFER helium leak detector, a leak through the cryostat's cap flange was found. After tightening the copper bolts on the flange and performing a heating-pumping cycle, the vacuum became stable at $5{\cdot}10^{-6}$ mbar. Table 7.5 summarizes the chronology of the energy resolution at 1332 keV for the IGEX detectors. An improvement of the energy resolutions after the heating-pumping cycles was obtained. The leakage current of RG2 was significantly higher than in RG1 and RG3, however the resolution is practically the same within ±0.1 keV. Finally, the energy resolutions of all IGEX detectors were restored close to their original values. Figure 7.4 presents the leakage current, the energy resolution and the count rate of IGEX detectors as a function of the applied bias voltage.

Detector, FWHM	Operating bias [V]	1993-94 [keV]	25.11.05 [keV]	04.12.05 [keV]	10.12.05 [keV]	24.12.05 [keV]
RG1	4800	**2.16**	2.6	2.34	2.38	**2.21**
RG2	4000	**2.37**	10	7.94	3.01	**2.31**
RG3	3800	**2.13**	4.7	2.74	3.9	**2.26**

Table 7.5: The chronology of the energy resolution (FWHM) at 1332 keV of IGEX detectors prior to their dismounting from cryostats.

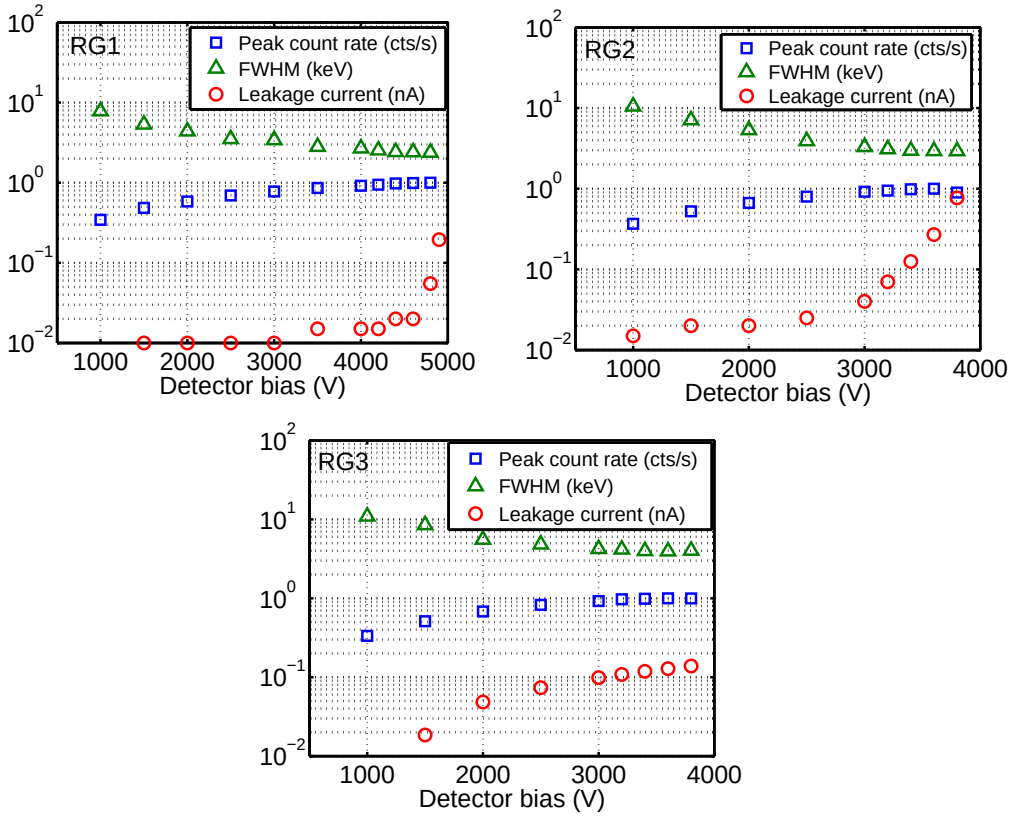

Figure 7.4: The leakage current, the energy resolution (FWHM) and the count rate of 1332 keV peak for the IGEX detectors vs. HV bias measured in GDL, LNGS, 10.12.05.

7.5 Dismounting of diodes and dimension measurements

From April 2006 to November 2006, the eight enriched diodes were dismounted from their cryostats in the clean room environment of the GDL. The dimensions of the diodes were measured (see Fig. 7.5) using a sliding gauge made of plastic to avoid scratches of the crystal surface during measurements. The accuracy of the dimension measurements is ±0.1 mm. The borehole is covered with a thin boron implantation layer. Because of the sensitivity of this layer, the diameter and the length of the well were measured approximately, without touching the surface. Therefore, the

accuracy of the hole measurement is within ±1 mm.

Table 7.6 gives the dimensions and the masses of the detectors. Each HdM and

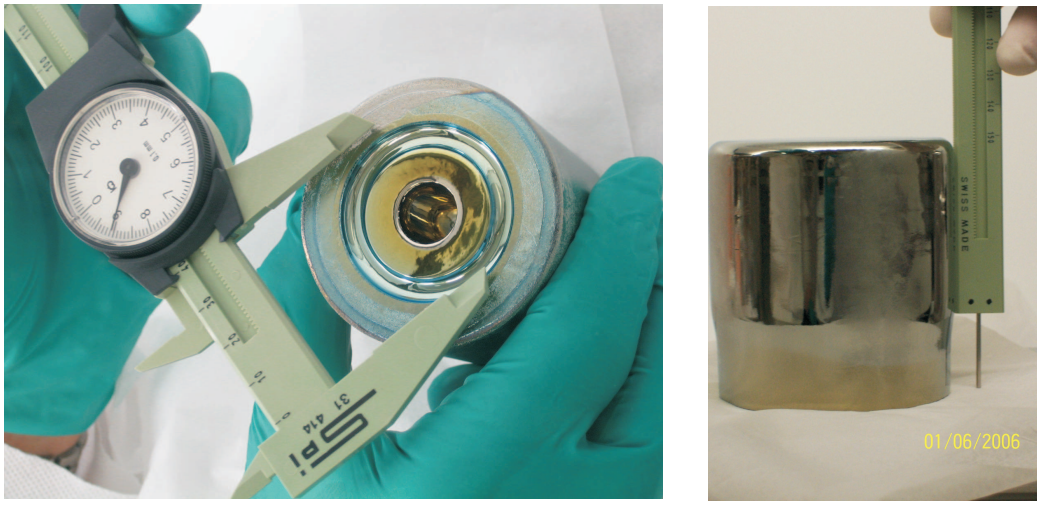

Figure 7.5: The enriched detectors ANG1 (left) and RG3 (right) after opening of the cryostats and detectors holders. Dimensions measurements were performed on the Class 10 clean bench in GDL at LNGS.

IGEX crystal has a specific shape which is slightly different from a cylinder. In addition, the cryostats have been measured (Fig. 7.6). The dimensions of the cryostats were verified with previous drawings and then used for a Monte Carlo simulation.

Detector	Mass Measured [g]	Mass Manufacturer [g]	Crystal Diameter [mm]	Crystal Length [mm]	Hole Diameter [mm]	Hole Depth [mm]
ANG1	968.7	980	58.3	68.2	11	51
ANG2	2878.3	2905	79.3	107.4	10	93
ANG3	2446.5	2447	78.1	93.3	11	81
ANG4	2401.2	2400	75.0	100.3	11	88
ANG5	2782.1	2781	78.3	105.5	10	93
RG1	2152.3	2149.9	78.5	84.0	12	32
RG2	2194.2	2194.0	78.5	84.5	10	74
RG3	2120.9	2121.0	79.8	82.6	12	77

Table 7.6: Masses and dimensions of the HdM and IGEX crystals measured after the dismounting from their cryostats in 2006. The error in the masses is 0.1 g. Diameter and length of crystals are measured with an accuracy 0.1 mm. The holes were measured with an uncertainty 1 mm.

Finally, crystals were stored in stainless steel containers under vacuum and transported to HADES for their refurbishment at Canberra Semiconductor NV.

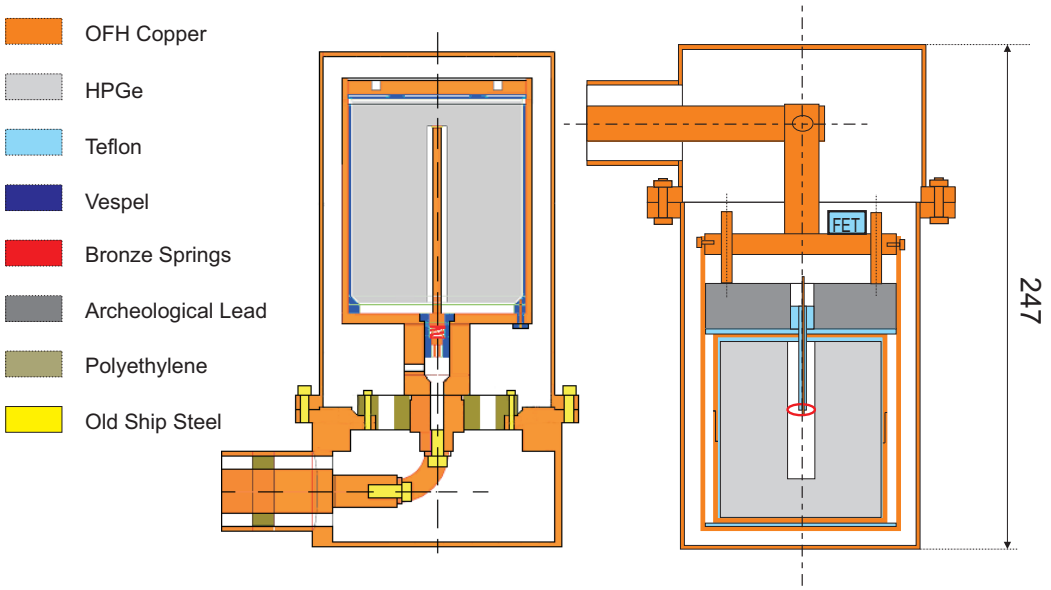

Figure 7.6: Scaled schematic diagram of the HdM(left) and IGEX(right) cryostat heads and detector holders.

7.6 Active mass determination

7.6.1 Motivation and method

The active mass of the HPGe detector is affected by the dead layer and incomplete charge collection. The latter is assumed to be negligible in a fully depleted germanium detector. The HdM and IGEX enriched detectors are fully depleted at their operational biases. Because the IGEX and some of HdM detectors have been stored for a prolonged period without cooling, their dead layers have likely increased. Therefore, measurements of detection efficiency and dead layer thickness were performed. The results were compared with the results of Monte Carlo simulations and the active masses and dead layers were determined. Another motivation for active mass study was the discrepancies between the measured and previously reported detector masses for ANG1 and ANG2 diodes (Table 7.6).

7.6.2 Experimental setup and measurements

The active masses of the HPGe detectors were determined using measurements with ^{60}Co and ^{133}Ba sources. One detector (RG1) was scanned with a collimated ^{133}Ba source to check variation of the dead layer. The dimensions of the cryostat parts and their relative positions were measured with an accuracy of 0.05 mm and 0.5 mm respectively, giving a precision of $\pm$0.1 mm for the dead layer thickness determination. To measure their performance parameters and the background, the HdM detectors were placed in a lead shield as shown in Fig. 7.7. The measurements with the IGEX

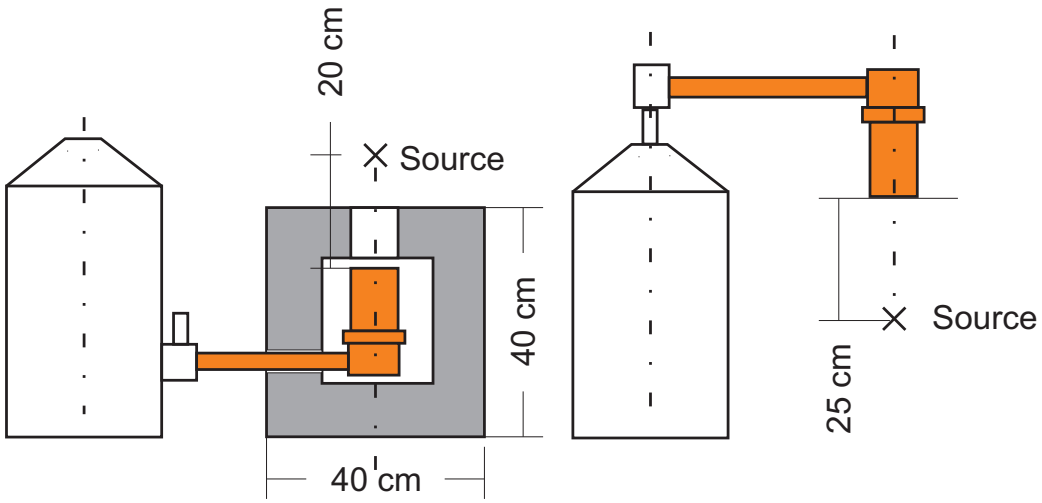

Figure 7.7: The HdM (left) and IGEX (right) detectors and the source setups. The HdM detectors were shielded with 10 cm of lead with a window for the source.

detectors were performed without a shield. The ^{60}Co source was placed ∼20–25 cm away from the detector copper cap. The time normalized background spectra were subtracted from the spectra measured with the source for each detector. The intensity of the summation peak at 2505 keV was 0.07% of the 1173 and the 1332 keV peak intensities. The statistical uncertainty of the measurements was better than 0.5%. The systematic uncertainty of the source activity was 3% (3σ). The activity of the ^{60}Co source was also verified using a ^{226}Ra source with 3% (3σ) uncertainty. The variations of the dead layers thickness were measured with a collimated ^{133}Ba source. The 81 keV gamma-rays were collimated by a 30 mm thick copper collimator with a 2 mm diameter hole. The collimator was moved along the RG1 cap diameter in 5 mm steps. The setup and the count rate profile of the 81 keV ^{133}Ba line are shown in Fig. 7.9. To determine the average dead layer thickness the measurements with the ^{133}Ba source were carried out without a collimator. The ^{133}Ba source was placed ∼20 cm from the center of the cryostat copper cap (Fig. 7.7). The ^{133}Ba 81 keV peak was measured with an accuracy of 10%. A simulation was performed for several values of the dead layer thickness with EGSnrc code. The measured and simulated ^{133}Ba spectra are presented in Fig. 7.8.

7.6.3 Monte Carlo simulation

Monte Carlo simulations were performed using two independent MC codes: MaGe framework [82] based on Geant4 (ver. 4.6.2) and EGSnrc simulation code [83]. Detailed geometry models were developed for the HdM and IGEX detectors based on the measurement of the crystals and cryostats dimensions. The cryostat schematic drawings are presented in Fig. 7.6. The dead layer thickness was a parameter of the simulation geometry. The Monte Carlo simulation results were verified by comparing the results of two codes for two detectors, ANG3 and ANG5 (Tab. 7.7). The angular correlation of the ^{60}Co photons was not implemented in the Geant4 and EGSnrc codes. The angular correlation can contribute up to 10% of the summation effect, which itself was measured to be as small as 0.07% of the 1332 keV peak. The results of the simulation and the measurement for the summation peak agree within statistical errors. The error in the summation peak is too big ($> 10\%$) to observe the angular correlation effect. The simulations with Geant4 were performed without including the lead shield in the geometry model. Therefore, the backscattering peak in the simulation spectra was absent. The lack of backscattering in the shield also affects the low energy part of the spectrum (< 300 keV), as seen in Fig. 7.8.

7.6.4 Results and comparisons with MC simulation

Table 7.7 presents the simulated and measured efficiencies for the ^{60}Co 1332 keV peak and for the integral count rate in energy range 400-1100 keV. The simulations were performed using the dead layer thicknesses provided by the manufacturer. The results of the simulation and the measurement agree within 3-6% for ANG1-4 and RG2. The results of simulations for ANG5, RG1, and RG3 are $\sim$10% higher than the measurements.
Figure 7.8 shows the ^{60}Co and ^{133}Ba spectra measured with ANG3 detector in the lead shield. As expected, the backscattering peaks at 216 keV and 149 keV from ^{60}Co and ^{133}Ba respectively are not observed in the simulations. The scan of RG1 with the collimated ^{133}Ba source (Fig. 7.9) shows that variations of the dead layer thickness are within 10%.

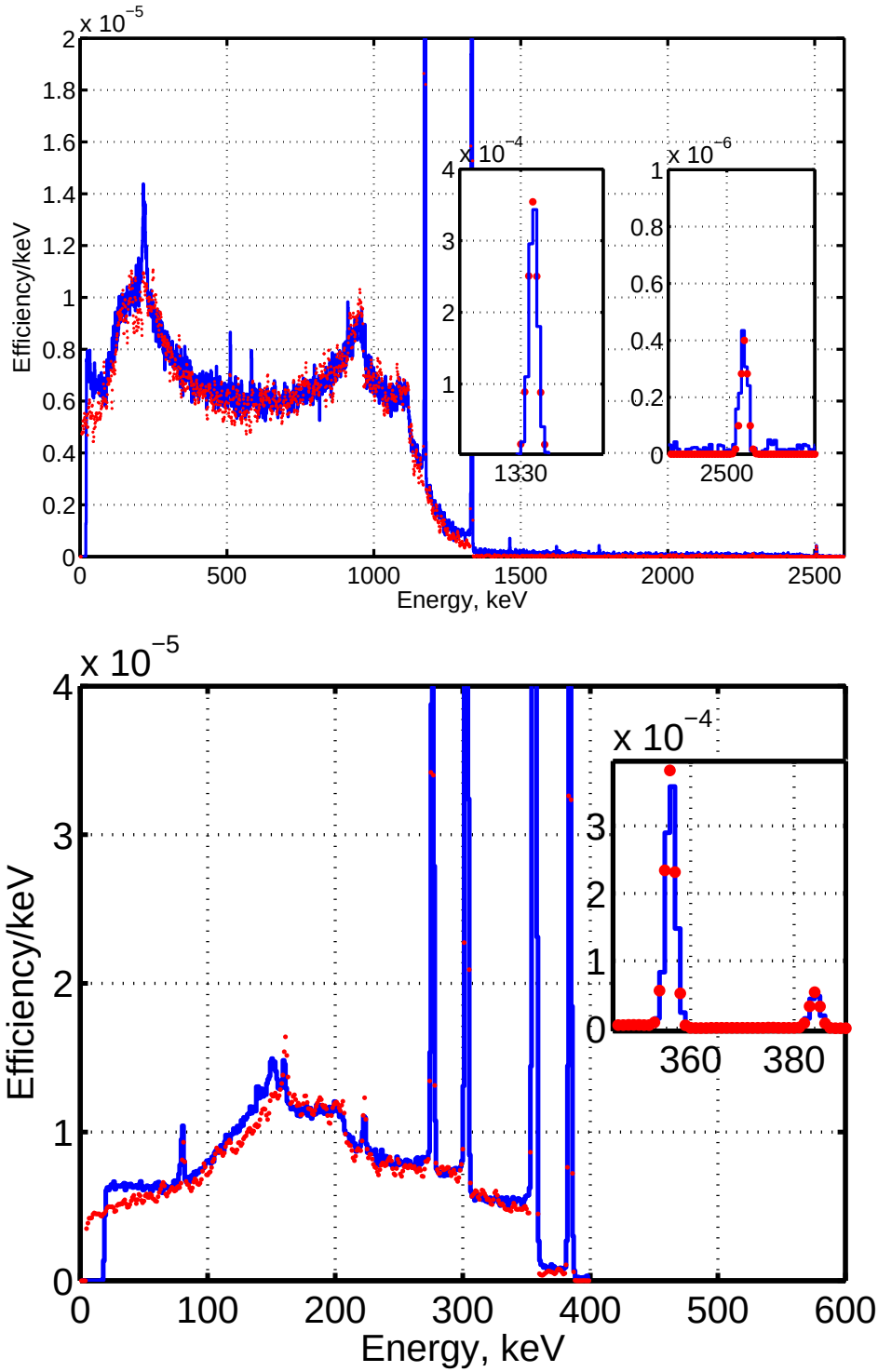

Figure 7.8: ^{60}Co (top) and ^{133}Ba (bottom) spectra measured with the ANG3 detector in the lead shield (solid line) and Monte Carlo simulation (red dots). The MC simulations were performed without a lead shield, therefore backscattering peaks at 216 and 149 keV from ^{60}Co and ^{133}Ba respectively are not observed in the simulation spectra.

Detector	Dead layer, manufac. [mm]	Distance, to source [cm]	Meas. Eff. ^{60}Co peak E=1332 keV ϵ_m, [10^{-3}]	Simul. Eff. ^{60}Co peak E=1332 keV ϵ_s,[10^{-3}]	δ, $\frac{\epsilon_m-\epsilon_s}{\epsilon_m}$ [%]	Meas. Eff. Contin. 400-1100 keV ϵ_m, [10^{-3}]	Simul. Eff. Contin. 400-1100 keV ϵ_s,[10^{-3}]	δ, $\frac{\epsilon_m-\epsilon_s}{\epsilon_m}$ [%]	Simulation code	Active mass, calcul. [g]
ANG1	0.7	19.5	0.473	0.461	2	2.85	2.80	2	Geant4	921
ANG2	0.7	19.7	1.16	1.18	-2	5.14	5.24	2	Geant4	2765
ANG3	0.7	21.4	0.97	1.03	-6	4.50	4.59	-2	Geant4	2338
ANG3	0.7			0.99	-2		4.36	3	EGS4	
ANG4	0.7	19.9	0.94	0.97	-3	4.42	4.31	2	EGS4	2292
ANG5	0.7	19.9	1.08	1.18	-9	4.88	5.30	-8	Geant4	2662
ANG5	0.7			1.20	-10		4.74	3	EGS4	
RG1	0.8	25.0	1.00	1.11	-11	3.82	3.58	7	EGS4	2043
RG2	0.8	25.0	1.06	1.08	-2	3.94	3.74	5	EGS4	2082
RG3	0.5	25.0	1.02	1.11	-9	3.81	3.62	6	EGS4	2054

Table 7.7: Results of measurement and simulation of the detection efficiency for HdM and IGEX detectors. The ^{60}Co source was positioned at distance R from the detector's copper cap. Efficiency for the 1332 keV peak and the Compton continuum sum in the energy range from 400 keV to 1100 keV are presented. The simulation for ANG3 and ANG5 was performed by two codes for simulation verification. Active masses and efficiencies have a $\sim 1\%$ error.

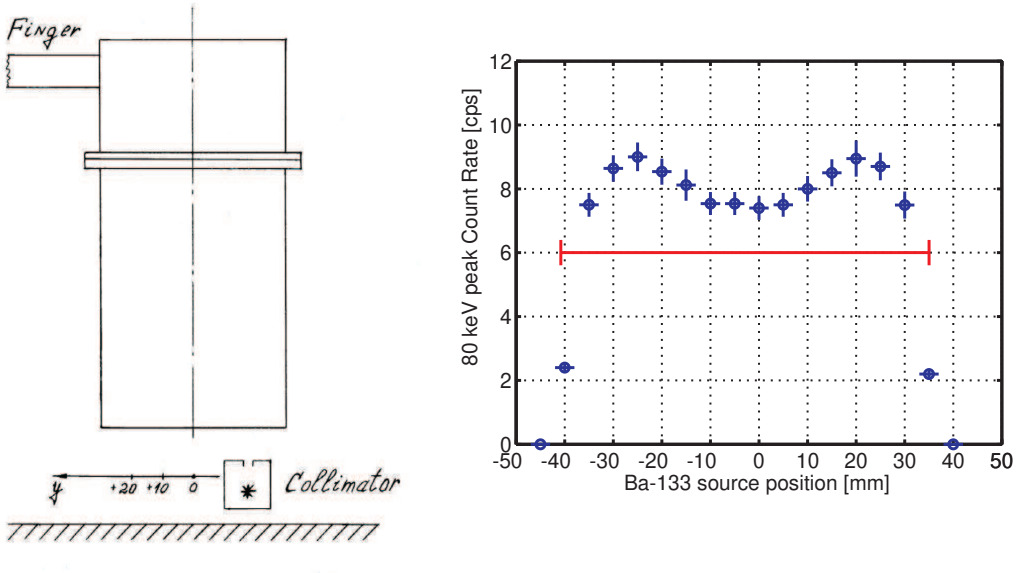

Figure 7.9: Left: schematic diagram of the setup for the dead layer measurements with a collimated source. Right: 81 keV peak count rate measured along the RG1 detector diameter with the collimated ^{133}Ba source. The crystal diameter is shown below the data points.

Detector	^{76}Ge [%]	^{74}Ge [%]	^{73}Ge [%]	^{72}Ge [%]	^{70}Ge [%]	ρ [g/cm^3]
ANG1	85.92	13.06	0.25	0.46	0.31	
ANG2	86.44	13.32	0.12	0.08	0.04	
ANG3	88.15	11.58	0.10	0.10	0.06	5.5
ANG4	86.3	na	na	na	na	
ANG5	85.6	na	na	na	na	
RG1						
RG2	87.43	12.51	0.05	0.005	0.005	5.5
RG3						
Natural Ge	7.76	36.54	7.76	27.43	20.52	5.3

Table 7.8: Isotopic content of the HdM and IGEX diodes. The uncertainty is $\sim 1\%$ for ^{76}Ge [29, 32].

7.6.5 Discussion of results

The 10% deficit of efficiency for ANG5, RG1 and RG3 detectors compared to the simulations can be explained by an increase in the detector dead layer by a factor of two. The difference can also result from incorrect dimensions in the detector model. Using the current measurements, one centimeter uncertainty in the source position results in 10% efficiency error. The dimensions of the detectors were verified to exclude systematic errors in the simulation. The cryostats were opened again and the dimensions were compared with previous measurements. No discrepancies in the dimensions were found.

Detector	Dead layer, manufac. [mm]	Dead layer ^{133}Ba meas. [mm]
ANG1	0.7	$\leq$0.2
ANG2	0.7	0.9$\pm$0.3
ANG3	0.7	0.4$\pm$0.3
ANG4	0.7	$\leq$0.8
ANG5	0.7	0.5$\pm$0.3
RG1	0.8	0.9$\pm$0.2

Table 7.9: The dead layer thicknesses provided by the manufacturers and determined with the ^{133}Ba source and MC simulations (Fig. 7.10).

The average dead layer thickness was determined using measurements with a ^{133}Ba source. To exclude the systematic uncertainty of the ^{133}Ba source activity the ratio of peak intensities was used instead of the absolute intensity of the peak. The peak ratio is also less sensitive to the uncertainty of the source position. The measured ratio of 80.9 keV and 356 keV ^{133}Ba peaks was used for comparison with the simulation results. The dependence of the peak ratio on the dead layer thickness is presented in Fig. 7.10. The dead layer thicknesses for the closed end surface of the detectors were determined and are presented in Table 7.10. The obtained values are in agreement (68% c.l.) with those stated by the manufacturer, except for ANG1, for which the dead layer thickness upper limit is 0.2 mm (68% c.l.). An investigation of the ANG1 detector history revealed an additional grinding of the surface of the detector in 1991, when the detector was broken [31, 62]. The thin dead layer and the reduced mass of the ANG1 detector both can be explained by the $\sim$ 0.7 mm layer of germanium, which had been removed from the closed end part of the diode. The dead layers of the ANG5 and RG1 detectors are found in agreement with the values provided by the manufacturer (0.7 mm and 0.8 mm, respectively), the observed 10% efficiency reduction for these two detectors cannot be explained. The dead layer on the closed end of the detector is not necessarily the same as the rest of the surface, therefore additional measurements of the dead layer on the side surface are recommended.
Kirpichnikov et al.[65] used a different approach to determine the active masses. The distributed sources of natural radioactivity in the surrounding rock are utilized

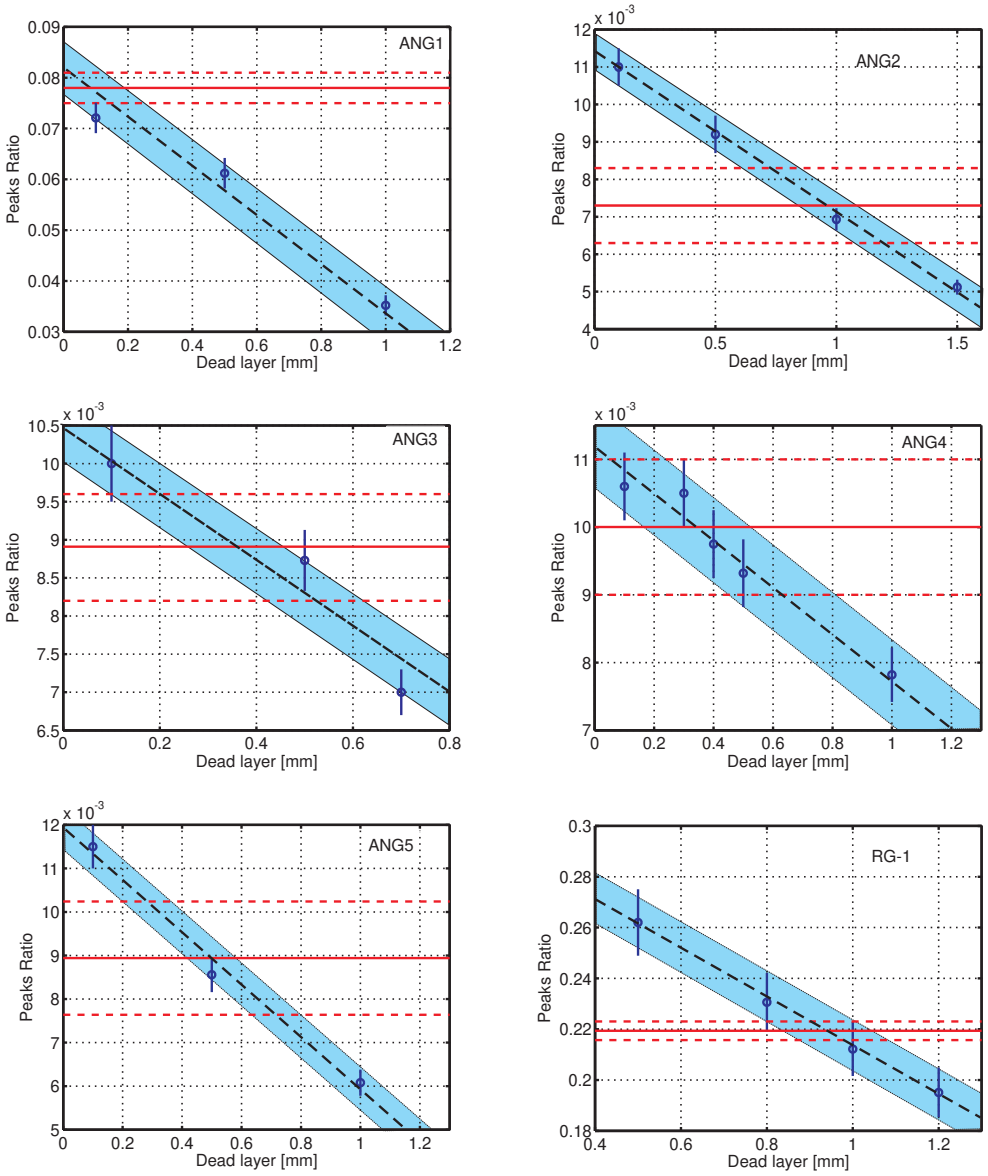

Figure 7.10: Ratio of the 81 keV and 356 keV ^{133}Ba peaks simulated as a function of the dead layer thickness for the ANG1-5 and RG1 detectors. The measured ratio is shown as the horizontal band with 1σ error.

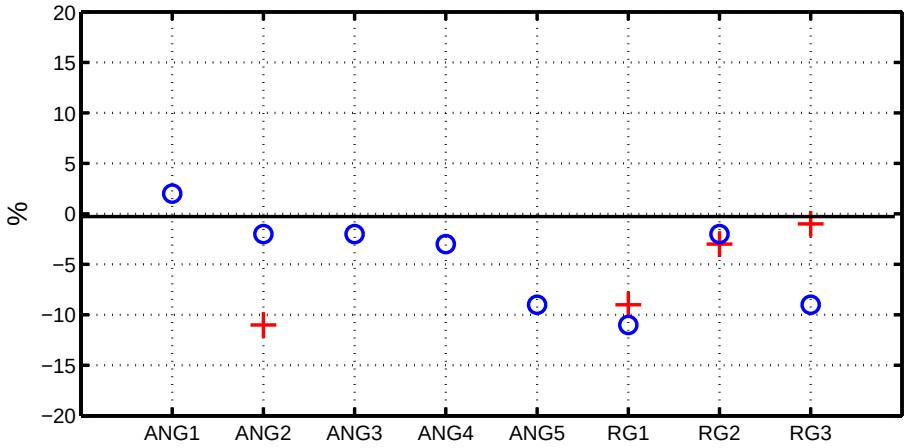

Figure 7.11: The relative deviations of measured and calculated active masses. (○) - measured with ^{60}Co source, (+) - determined with background measurements [65]. The errors are within the size of the symbols.

instead of artificial point sources. One of the detectors has to be assigned as reference detector for the relative measurements. The measurements have to be carried out at the same place and at the same time to be comparable. The active masses of RG1-3 and ANG2 were determined using background measurements in GDL. The RG3 was selected as the reference detector. The active masses of RG1 and RG2 were found in agreement with the source measurements, but ANG2 and RG3 are 10% off (Fig. 7.11). The uncertainty of $\pm 5\%$ for the active mass is a reasonable estimate.

The active mass is decreasing if the detector is not fully depleted. However, the measurements were performed at operating bias, when count rate is saturated, as shown in previous sections, and therefore this effect can be excluded. Another possibility is the presence of high concentration of the charge traps in some parts of the detector volume. The trapping effect is possible to diagnose using detailed detector scanning with a collimated source.

Table 7.9 gives the active masses of the detectors.

The active masses were calculated using the dead layer thickness given by the manufacturers with 10% uncertainty, which was determined using the collimated ^{133}Ba source measurements.

7.7 Summary

The GERDA Phase I detectors from HdM and IGEX experiments were maintained and their performance parameters characterized between September 2004 and November 2006. The main spectrometric and working parameters such as energy resolution,

Detector	Measured mass [g]	Calculated active mass, [g] $\rho^* = 5.5$ g/cm^3	Previously Reported active mass, [g] (Tables 7.2, 7.4)	Active mass, % of measured
ANG1	**968.7±0.1**	**921±9**	920	95±1
ANG2	**2878.3±0.1**	**2756±28**	2758	96±1
ANG3	**2446.5±0.1**	**2338±23**	2324	96±1
ANG4	**2401.2±0.1**	**2292±23**	2295	96±1
ANG5	**2782.1±0.1**	**2662±27**	2666	96±1
RG1	**2152.3±0.1**	**2043±20**	∼2000	95±1
RG2	**2194.2±0.1**	**2082±21**	∼2000	95±1
RG3	**2120.9±0.1**	**2054±21**	∼2000	97±1
Total	**17944.2±0.3**	**17148±56**	—	95.5±0.3

Table 7.10: The active mass of HdM and IGEX detectors calculated using the measured dimensions from Tab. 7.6. (*) The specific density of enriched germanium (86% ^{76}Ge) is slightly higher than the natural germanium density, $\rho_{^{76}Ge} = 5.5$ g/cm^3, $\rho_{natGe} = 5.3$ g/cm^3.

operation voltage and leakage current have been measured. The ANG1 and RG2 detectors initially showed deteriorated energy resolution and high leakage current. To restore their parameters, heating and pumping operations have been performed. Finally, all the detectors demonstrated parameters which correspond to the specifications at the time of production.

Measurements of detector efficiencies with a ^{60}Co source were performed for all the enriched detectors. The measured efficiencies were compared with Monte Carlo simulations. For the verification of the simulations, two independent codes were used: Geant4 and EGSnrc. The two codes produce results within statistical errors. Using the efficiency and the dead layer values the active masses of the enriched detectors for the GERDA Phase I were determined. The obtained active masses were compared with those provided by the manufacturer and were found to agree. The deterioration of the dead layers were found to vary by less than 0.2 mm from the values provided by the manufacturers. The total and active masses of the GERDA Phase I detectors before their refurbishment are 17944.2±0.3 g and $17.2^{+0.1}_{-0.8}$ kg respectively.

Afterwards, the enriched diodes were dismounted from their cryostats and sent to Canberra Semiconductor NV, Olen, Belgium, in preparation for GERDA Phase I.

Chapter 8

Searching for Neutrinoless Double Electron Capture of ^{36}Ar

Double electron capture ($2EC$) is a process inverse to double beta decay. This chapter presents a search for the neutrinoless mode of the double electron capture ($0\nu 2EC$) in ^{36}Ar. The decay of ^{36}Ar has not been investigated yet and no measured limits of the half-life exist in the literature. Measurements with a bare HPGe detector in liquid argon were performed in the GERDA underground detector laboratory (GDL) at LNGS during a long term stability test of the detector parameters. The measured background spectra were analyzed and the first limit for the radiative mode of the $0\nu 2EC$ decay in ^{36}Ar is reported.

8.1 Introduction to radiative $0\nu 2EC$ decay in ^{36}Ar

The study of the $0\nu 2EC$ decays could give additional information about mechanisms of the lepton number violation (see e.g. [75]). In the process of $2EC$, the two atomic electrons are absorbed by the nucleus:

$$e^- + e^- + A(Z) \Rightarrow A(Z-2) + (2\nu) + Q. \tag{8.1}$$

In the two neutrino $2EC$ decay, the energy is carried away by two neutrinos (neglecting atom's recoil) and X-rays. In the neutrinoless case, the momentum-energy conservation requires that the energy has to be released somehow. There are various $0\nu 2EC$ decay modes with emission of e^+e^- pairs, internal conversion electrons or photons. The latter mode is a radiative $0\nu 2EC$ decay. The bremsstrahlung photon is emitted by one of the captured electrons. The capture of the two K-shell electrons in the $0^+ \rightarrow 0^+$ transition with emission of one photon is forbidden by the conservation of the angular momentum, therefore, one of the electrons has to be captured from the L shell. The detailed discussion of the $2EC$ processes with emission of photons can be found e.g. in [78, 79].
Natural argon contains the isotope ^{36}Ar with an abundance of 0.336%, which is expected to be unstable undergoing the double electron capture [74]. The energy

levels of the $A = 36$ isobar triplet are shown in Fig. 8.1 [28]. The energy of the ^{36}Ar decay is 433.5 keV. Therefore, the radiative and the internal conversion modes of the $0\nu 2EC$ decay are energetically allowed. The search of the radiative $0\nu 2EC$ decay can be performed with a gamma-ray detector.

The amplitude of the $2EC$ transition with the energy release Q close to the $2P$–$1S$

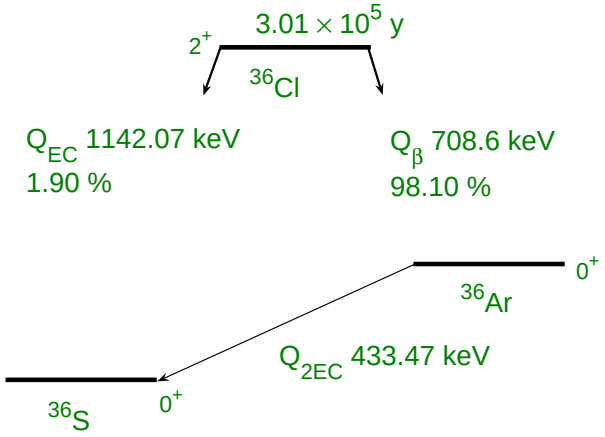

Figure 8.1: Lowest energy levels of isobar triplet A=36 with double electron capture decay of ^{36}Ar [28].

atomic level difference could be resonance enhanced, as was shown in [81]. In the case of ^{36}Ar, the daughter ^{36}S has no excited states available for the $2EC$ transition. Therefore, the $2EC$ decay must be a ground-state-to-ground-state transition ($0^+_{g.s.} \rightarrow 0^+_{g.s.}$). One electron is captured from the $K, L...$ shells and the other from the $L, M...$ shells. Theoretical calculations have been carried out for the two neutrino $2EC$ decay mode with the half-live in the order of 10^{29} years [76]. A preliminary estimate of the neutrinoless mode gives a half-live in the order of 10^{35} years [77], which is far beyond the current experimental sensitivity.

The expected decay of ^{36}Ar will produce three photons with energies: $E_K = 2.47$ keV, $E_L = 0.23$ keV and $E_\gamma = 430.8$ keV given the $Q_{2EC} = 433.5$ keV. The experimental signature is the monochromatic photon with the energy of $E\gamma = Q - E_K - E_L = 430.8$ keV, which is detected with a high-purity germanium (HPGe) detector submerged in liquid argon. In addition, the two X-rays of the daughter atom could give a coincidence trigger, if the liquid argon scintillation light is detected.

Experimental parameter	Value
Volume of liquid argon	70 ± 7 liters
Mass of liquid argon	100 ± 10 kg
Detector diameter and length	75 mm, 69 mm
Measurement live-time	237 hours
Energy resolution (FWHM) at 430.8 keV	4.1±0.5 keV
Full energy peak efficiency at 430.8 keV	0.26±0.03 %
^{36}Ar abundance	0.336 %
^{36}Ar 2EC reaction Q value	433.5 keV
^{36}S Binding energy E_K, E_L [28]	2.47 keV, 0.23 keV

Table 8.1: Experimental parameters and values used for analysis.

8.2 Experimental setup in the GERDA detector laboratory

The measurements were performed in the GERDA underground detector laboratory (GDL) located at LNGS. The laboratory is equipped with a radon-reduced clean bench mounted to a dewar system. It is designed to operate bare germanium detectors submerged in liquid argon or nitrogen. For the past two years, the leakage current, the energy resolution and the detector stability have been investigated in this setup. Table 8.1 gives the experimental parameters and the values used for the present measurement. The experimental setup is shown in Fig. 8.2. A 300 cm^3 high-purity germanium diode was mounted in the GERDA Phase I low mass holder to provide suspension, high voltage and signal contacts. The holder made of copper, silicon and PTFE was suspended on 80 cm long Kevlar strings. The strings were attached to a dewar flange on which a warm FET preamplifier (CANBERRA 2002) was installed. The detector was positioned in the center of a 70 l dewar. The moderate shield of the test bench consisted of 2.5 cm of lead surrounding the dewar. It slightly suppresses the external radiation by a factor around 10. The dewar was refilled with liquid argon every four days. Between fillings 14 l of argon evaporates. The ORTEC spectrometry amplifier and Maestro multichannel analyzer (MCA) were used to collect spectra continuously between fillings. A ten day background spectra were acquired during a long term stability test ordinarily performed with a ^{60}Co source. The resolution of the ^{40}K 1460.8 keV background line was 4.56 keV (FWHM). The energy calibration was performed using a ^{60}Co source and the background peaks. The energy resolution dependance on energy was fitted by the function: $FWHM(keV) = \sqrt{15 + 0.0039 \cdot E_\gamma}$, where E_γ is the energy in keV. For example, the energy resolution of the expected peak at 430.8 keV from the radiative $0\nu 2EC$ decay is 4.1 keV. The detector parameters, energy resolution and leakage current, were stable during the measurement.

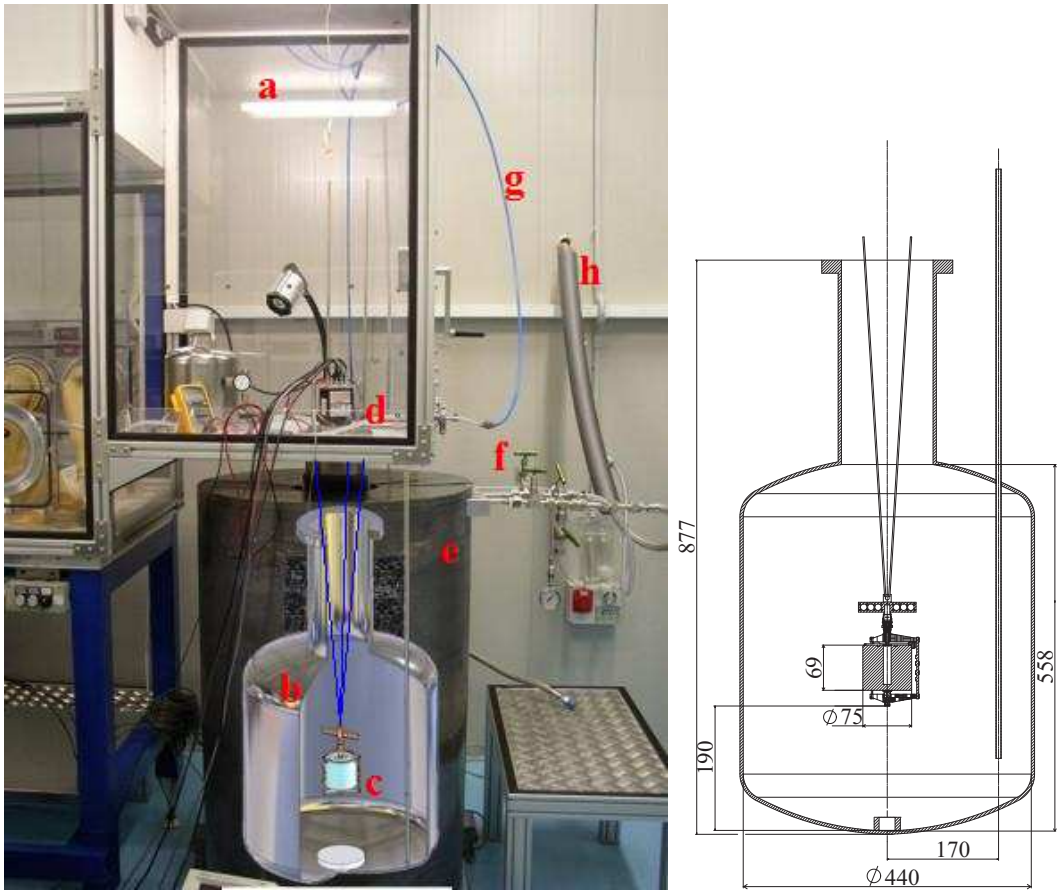

Figure 8.2: The experimental setup for measurements with a bare HPGe detector in liquid argon. On the left, the detector test bench of GDL in which a bare HPGe detector is operated in liquid argon. On the right, a detailed view of the detector assembly in the dewar. The figure shows: a) the radon free detector test bench, b) the 70 liter dewar, c) the HPGe detector in LAr suspended on Kevlar strings, d) the warm FET preamplifier, CANBERRA 2002, e) the lead shield barrel, f) the liquid argon filling/venting lines, g) the nitrogen gas flushing line, h) the line to the external refilling dewar.

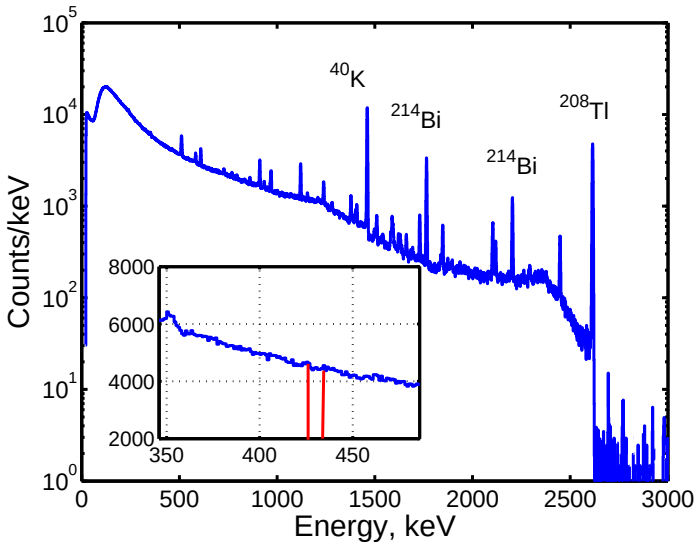

Figure 8.3: The measured background spectrum of a bare HPGe detector operated in liquid argon over a 10.0 days. *In the inset*: Low energy part of the spectrum together with the region of interest around Q-value of the $0\nu 2EC$ decay of ^{36}Ar.

8.3 Results and analysis

Three measured energy spectra with respective live times of 70.4, 96.6 and 70.0 hours were individually calibrated in energy and then summed together. Fig. 8.3 displays the resulting spectrum and the region of interest around 430 keV. In the region of interest the background index amounts to 440 counts/(keV·day). The spectrum shape is dominated by the γ-rays from the external natural radioactivity. The intensity and the resolution of the major peaks are shown in Table 8.2. The simulation codes EGSnrc [83] and TEFF [84] were used to determine the full energy peak (FEP) efficiency ε of detection for the photons emitted in the liquid argon

Measured energy [keV]	FWHM [keV]	Peak area
609.4	4.32	6656±260
1120.5	4.33	7906±187
1461.1	4.56	55850±261
1764.7	4.68	15589±146
2204.2	4.98	5850±100
2614.5	5.05	25664±161

Table 8.2: The intensity and the resolution of the major peaks in the background spectrum measured with the HPGe detector in liquid argon for 237 hours.

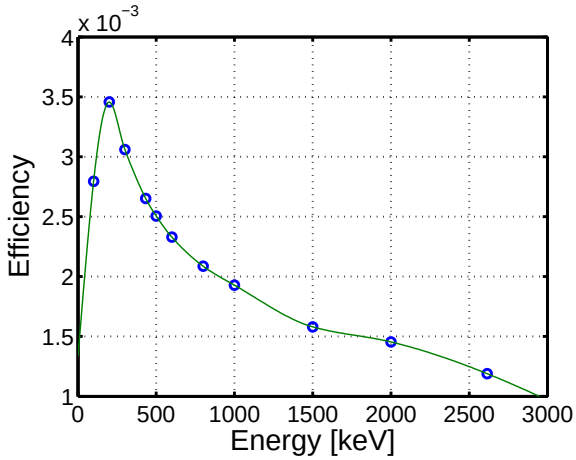

Figure 8.4: Calculated full energy peak efficiency of the 300 cm^3 HPGe detector in the 70 liter dewar filled with argon. Simulated γ-rays are uniformly distributed in the argon volume.

volume. The energy dependence of the FEP detection efficiency is shown in Fig. 8.4. The spectrum in the energy range of 350–500 keV is essentially featureless, as seen on the inset of Fig. 8.3. The lower half-life limit is expressed as a function of the upper limit for counts in the peak ($\lim S$) at a given confidence level:

$$\lim T_{1/2} = \ln 2 \cdot N \cdot \varepsilon \cdot \frac{\Delta T}{\lim S}, \quad N = N_A \cdot \frac{a \cdot M}{A}, \tag{8.2}$$

where N is the number of the $2EC$ source nuclei, ε is the FEP efficiency, ΔT is the measurement time, a is the isotopic abundance of the isotope, M is the total mass of the argon source material, N_A is the Avogadro number, and A is the molecular weight of the source material. The upper limit on the number of counts in the expected peak was obtained by fitting the experimental energy distribution with the sum of a Gaussian and a linear background slope. The Gaussian mean and standard deviation are fixed to 430.8 keV and 1.84 keV, respectively. The amplitude of the gaussian and the parameters of the linear continuum were free parameters of the least square fitting in the energy interval of 410–450 keV (Fig. 8.5).
In the region between 410 and 450 keV, assuming a linear background, the best fit yields a negative number of counts under the peak $-376 \pm 230(382)$ counts at 68%(90%) C.L. The resulting upper bound on the number of candidate events in the $0\nu 2EC$ decay peak is a 1σ statistical fluctuation S of background counts in the energy window ΔE=5 keV, $S = \sqrt{B \cdot \Delta E} = \sqrt{4500 \cdot 5}$=150 at 68% C.L. The resulting lower limit on the half-life is computed according to (Eq. 8.2): $T^{0\nu}_{1/2}(^{36}\mathrm{Ar}) = \geq (1.85 \pm 0.25(\mathrm{syst}) \pm 0.01(\mathrm{stat})) \cdot 10^{18}$ y (68% C.L.). The systematic uncertainties reside in the source mass, efficiency calibration and background spectral shape. The main factors influencing the limit are the uncertainty in the source mass (±10%) and the efficiency of detection (±10%). The quoted 68% C.L. lower bound was computed using the best value, 430 keV. There is a small dip in the data centered at

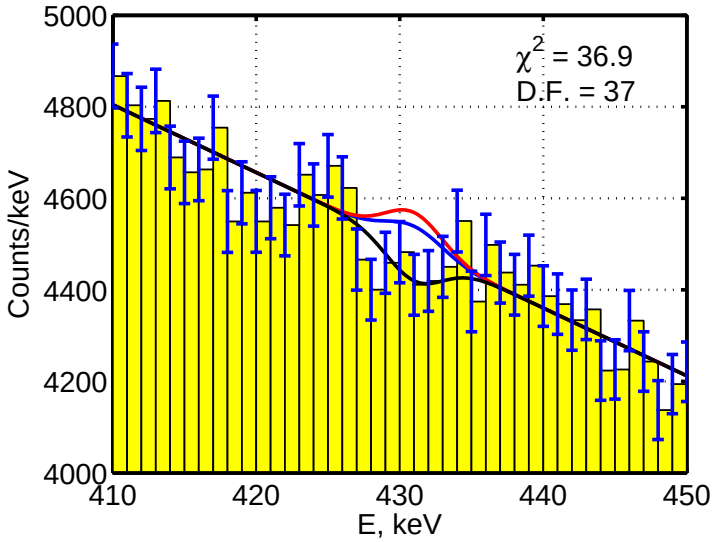

Figure 8.5: The fit of the measured energy spectrum of the HPGe detector in the region of interest around the Q-value of the $0\nu 2EC$ decay of ^{36}Ar. The sum of a Gaussian and a linear slope (black curve) fitted to the measured energy spectrum. The blue and red lines are the 68% and 90% C.L. bounds on the peak counts, respectively.

430 keV as shown in Figure 8.5. This has been treated as a statistical fluctuation. With Eq. 8.2 and the values given in Tab. 8.1, the half-life limit for the radiative $0\nu 2EC$ decay of ^{36}Ar with emission of single photon is:

$$T_{1/2}(0^+ \rightarrow g.s.\ with\ emission\ of\ single\ \gamma) \geq 1.85 \cdot 10^{18}\ y\ (68\%\ C.L.). \quad (8.3)$$

The obtained half-live limit is comparable to recent results from dedicated experiments, which are summarized in Tab. 8.3. The half-life limits for most of $0\nu 2EC$ decay experiments are in the range of 10^{16}–10^{19} years. The best limit ($\sim 10^{21}$ y) was achieved with an enriched ^{78}Kr [88].

Isotope	Abundance [%]	Mode	$T_{1/2}$ limit [y] (C.L.)	Reference
^{36}Ar	0.336	0ν2EC	$1.85 \cdot 10^{18}$ (68%)	this work [98]
^{50}Cr	4.345	$(0\nu+2\nu)$ECβ^+	$1.3 \cdot 10^{18}$ (95%)	Bikit et al. (2003) [85]
^{64}Zn	48.63	0ν2EC	$4.1 \cdot 10^{18}$ (68%)	Belli et al. (2008) [86]
		0νECβ^+	$6.1 \cdot 10^{20}$ (68%)	–"–
^{74}Se	0.89	0ν2EC	$6.4 \cdot 10^{18}$ (90%)	Barabash et al. (2006) [87]
		$(0\nu+2\nu)$ECβ^+	$1.9 \cdot 10^{18}$ (90%)	–"–
^{78}Kr	0.35	2ν2EC	$1.5 \cdot 10^{21}$ (90%)	Gavriljuk et al. (2006) [88]
^{106}Cd	1.25	2ν2EC	$4.8 \cdot 10^{19}$ (90%)	Stekl et al. (2006) [89]
^{108}Cd	0.89	0ν2EC	$2.5 \cdot 10^{17}$ (68%)	Danevich et al. (2003) [90]
^{112}Sn	0.97	$(0\nu+2\nu)$ECβ^+	$1.5 \cdot 10^{18}$ (68%)	Kim et al. (2003) [91]
^{120}Te	0.09	2ν2EC	$9.4 \cdot 10^{15}$ (90%)	Kiel et al. (2003) [92]
^{130}Ba	0.106	0νECβ^+	$2.0 \cdot 10^{17}$ (90%)	Cerulli et al. (2004) [93]
^{136}Ce	0.185	2ν2EC	$4.5 \cdot 10^{16}$ (68%)	Belli et al. (2003) [94]
^{138}Ce	0.251	2ν2EC	$6.1 \cdot 10^{16}$ (68%)	–"–
^{180}W	0.12	0ν2EC	$1.3 \cdot 10^{17}$ (68%)	Danevich et al. (2003) [95]

Table 8.3: Recent results of half-life measurements for $2EC$ and $EC\beta^+$ processes with transition to ground state.

8.4 Outlook

The sensitivity of the experiment presented here is limited by the radiation from the outside of the setup, which is not designed for ultra low-background measurements. The GERDA-LARGE facility, which will be used to test the backgrounds of the Phase I detectors prior to their operation in GERDA, will provide improved limits. External radiation will be suppressed by a massive passive shield, the mass of argon will increase to approximately one ton and up to nine detectors could in principle be operated simultaneously. The sensitivity will then be limited by the bremsstrahlung of ^{39}Ar beta decays (Q = 565 keV, $T_{1/2}$ = 269 y). The Monte-Carlo simulation gives a count rate which is on the order of 3 counts/(keV·y·kg) in the HPGe detectors at 430 keV [97]. An additional source of background is the $2\nu\beta\beta$ decay of ^{76}Ge. For enriched detectors this background is ∼1.5 counts/(keV·y·kg) in the region of interest, which is comparable to the ^{39}Ar background. The background can be reduced by an order of magnitude using detectors made of natural germanium. For one year of measurements, the expected sensitivity is in the range of 10^{22}–10^{23} years. If the X-ray scintillations in liquid argon can be detected with a reasonable efficiency, an X-ray – gamma coincidence could be exploited as an additional signature to reduce the ^{39}Ar bremsstrahlung background. The ultimate sensitivity will be achieved in GERDA with the operation of 40 kg of HPGe detectors in Phase I and Phase II.

8.5 Summary

An experiment to search for double electron capture with the emission of one photon in ^{36}Ar was proposed and carried out in the GERDA underground detector laboratory at LNGS using a bare HPGe detector submerged in liquid argon. For the first time a limit on the neutrinoless double electron capture decay of ^{36}Ar has been determined from the experimental data with $T_{1/2} \geq 1.85 \cdot 10^{18}$ yr at 68% C.L.. The given limit is comparable to those for different isotopes obtained in dedicated experiments. The sensitivity in the LARGE setup and the limiting backgrounds of ^{39}Ar bremsstrahlung and $2\nu\beta\beta$ have been estimated.

Chapter 9

Conclusions

The thesis focuses on the search for neutrinoless double beta ($0\nu\beta\beta$) decay of ^{76}Ge with HPGe detectors. The germanium detectors are proven to be an excellent instrument for double beta decay searches because they have superior energy resolution and very high purity of the detector material. Because ^{76}Ge acts both as the source and the detector, high detection efficiency is reached. Presently the best limits on $0\nu\beta\beta$ decay come from germanium experiments: Heidelberg-Moscow and IGEX. Their sensitivities reach about 0.3 eV of the effective neutrino mass $m^{\nu}_{\beta\beta}$. Both collaborations have reported almost the same lower limit on the $0\nu\beta\beta$ decay half-life of $\sim 1.6 \cdot 10^{25}$ y (68% C.L), corresponding to an effective neutrino mass upper limit range of 0.33 to 1.3 eV (68% C.L).

Two different experiments located at LNGS - HdM and GERDA, both using enriched HPGe diodes but with different operating techniques, were presented. The first one, HdM experiment, has operated from 1990 to 2003 and had provided new results on double beta decay search. The second one, GERDA, is now under construction in Hall A of LNGS, and will search for $0\nu\beta\beta$ decay with higher sensitivity, using bare germanium detectors submerged in liquid argon. The liquid argon will serve as a shield against external radioactivity as well as a cooling medium.

This thesis presents improved analysis of the HdM raw data collected in the period from 1990 to 2003. More accurate energy calibration was performed resulting in better energy resolution of the summed spectrum. The fitted background spectrum gives accurate peak positions and widths. The energy resolution determines the sensitivity of the experiment. 20% improvement in the energy resolution was obtained which led to 10% increase in sensitivity. This improvement led to publications [14, 15], which claim 4.2σ evidence of $0\nu\beta\beta$ decay.

A new background model of the HdM spectrum was developed using measurements with sources and MC simulations. The model accounts for the ^{226}Ra ^{232}Th and ^{60}Co contaminations, the muon induced neutrons and the $2\nu\beta\beta$ decay. The model deviation from the HdM spectrum is within 1% in the energy interval 250-2800 keV. The background continuum in the region of interest around $Q_{\beta\beta}$ value was determined using the model. The obtained value of the background is (11.8±0.5) counts/keV, which is higher than the background used in publication [14] – (10.0±0.3) counts/keV.

The model is still not accounting for all data in the full range of energies (e.g. ^{207}Bi, ^{125}Sb, ^{134}Cs). However, it accounts for contributions from ^{232}Th, ^{238}U, ^{226}Ra, ^{60}Co and muon induced neutrons to the region of interest around $Q_{\beta\beta}$ value. The fit of the HdM spectrum with the model background gives better agreement of the ^{214}Bi lines intensities. The intensity of the $\sim$2039 keV peak, (15$\pm$12) counts for 71.7 kg y, is less significant than the published value, (28.8$\pm$6.9) counts [14] which was obtained before the model was developed in 2006. The corresponding half-life of the $0\nu\beta\beta$ decay is $2.2 \cdot 10^{25}$ y and the 68% C.L. interval is $(0.4 - 4.0) \cdot 10^{25}$ y, the sensitivity of the HdM experiment for $0\nu\beta\beta$ decay is $4.6 \cdot 10^{25}$ y (68%, C.L.). The effective neutrino mass is 0.32 eV within (0.19-0.45) eV 68% C.L. interval using the nuclear matrix elements reported in [37].

The GENIUS-TF setup with four HPGe detectors immersed in liquid nitrogen was presented. The author's work covers the first year of operation, including the detector assembly, at the Gran Sasso underground laboratory. The measurements performed during the first year shown that the detectors and the electronics were highly sensitive to environmental interferences (vibrations in liquid nitrogen, electromagnetic pickups and infrared radiation). Techniques were applied to reduce these interferences and an acceptable energy resolution was obtained ($\sim$4 keV). An analysis of the GENIUS-TF background after the completion of the shield was presented. The contribution to the background coming from the ^{222}Rn decay chain was identified.

During one year, the four bare HPGe detectors operated in liquid nitrogen were biased at their nominal voltage and their parameters were stable. No deterioration of their energy resolution and leakage current was observed. It shows the principal feasibility of the GERDA experiment, which will use bare germanium detectors in liquid argon.

The shielding needed for the GERDA experiment depends on the intensity of the external radiation. The γ-ray flux at the GERDA experimental site has been determined for the first time in 2004 with a collimated γ-spectrometer. The flux had to be remeasured in 2007 after the reconstruction of Hall A. An HPGe detector was used to perform these measurements with and without a collimator. The collimator was used in 2004 for angular flux distribution measurements. The detector response was determined with Monte-Carlo simulations. The 2614 keV photon flux is (362$\pm$12) $\mathrm{m^{-2}s^{-1}}$. The contribution to the GERDA background index from external γ-radiation has been calculated as $1.1 \cdot 10^{-5}$ $[\mathrm{keV\,kg\,y}]^{-1}$. Details of the external GERDA shielding are optimized based on these measurements.

The GERDA Phase I enriched detectors from HdM and IGEX experiments were maintained and their performance parameters characterized in the period from September 2004 to November 2006. The main spectrometric and working parameters such as energy resolution, operation voltage and leakage current have been measured. Detector efficiency measurements with a ^{60}Co source were performed for all the enriched detectors. The dead layers of most detectors were determined and compared to previous values. After more than ten years, the increase in dead layer is negligible. The measured efficiencies were compared with Monte Carlo simulations.

With the efficiency and the dead layer values, the total active mass of all enriched detectors were determined to be $17.2^{+0.1}_{-0.8}$ kg.
An experiment to search for double electron capture with the emission of one photon in ^{36}Ar was proposed and carried out in the GERDA underground detector laboratory at LNGS using a bare HPGe detector submerged in liquid argon. For the first time a limit on the neutrinoless double electron capture decay of ^{36}Ar has been determined from the experimental data with $T_{1/2} \geq 1.85 \cdot 10^{18}$ yr at 68% C.L. The given limit is comparable to those for different isotopes obtained in dedicated experiments. The sensitivity in the LARGE setup and the limiting backgrounds of ^{39}Ar bremsstrahlung and $2\nu\beta\beta$ have been estimated.

Acknowledgments

It was a pleasure for me to work with all the wonderful people here in Heidelberg. First of all, I would like to thank Karl-Tasso Knöpfle for being a great advisor. His tremendous support had a major influence on this thesis. He spend a lot of time helping me as well as all the other people in our lab. I would like to thank him for his "Scientific Writing" introduction. I would like to thank Stefan Schönert for reviewing my thesis. I am happy to have such a supportive supervisor. I enjoyed his interest in my research as well as the fruitful discussions.
My thanks to my friends and colleagues for the great time I had in our group. I enjoyed the atmosphere, their friendship, and their support. My thanks to: Marik Barnabe-Heider, Claudia Tomei, Tina Pollmann, Andrey Vasenko, Sergey Vasiliev, Dushan Budjas, Grzegorz Zuzel, Mark Heisel, Werner Maneschg, Peter Peiffer, Alexander Merle, and Alexander Dietz for the great collaboration over the years. It was a pleasure to work with all these people and to benefit from their knowledge. Especially, I would like to thank Marik Barnabe-Heider and Konstantin Gusev for the interesting and fruitful discussions, for the great collaboration on GERDA, and for the cool time we had in Gran Sasso.
Special thanks to Herbert Strecker and Ute Schwan for their help on different technical problems.
My thanks to Marik Barnabe-Heider for proof-reading of thesis and for providing helpful suggestions for improving this manuscript. Any "linguistic crimes" are mine alone.
My thanks to Askhat Gazizov for his helpful insights on the subject.
My thanks to Vladimir Tretyak for providing me his code on spectra relocation and delightful discussions on double beta decay subjects.
My thanks to Prof. H. V. Klapdor-Kleingrothaus for being open-minded in discussions.
My thanks to Frau Anja Berneiser, Frau Brigitte Villaumie and Frau Ruth Häfner for help on administrative matters.
Last but not least, I wish to thank my family who have always supported me, Maryna and Maxim, and most of all Natalia for enjoying life together with me.
This thesis has been supported by Max-Planck Gesellschaft (MPG) and Max-Planck-Institut für Kernphysik. Their support is gratefully acknowledged.

Bibliography

[1] J. D. Vergados, Phys. Rep., 361 (2002);
P. Vogel, arXiv:hep-ph/0611243.

[2] F. Boehm, P. Vogel, "Physics of massive neutrinos", second ed. 1992, Cambridge University Press.

[3] M. C. Gonzalez-Garcia, M. Maltoni, Phys. Rep, 460 (2008) 1;
H. A. Nunokawa, S. B. Parke, J. W. F. C. Valle, Progress in Particle and Nuclear Physics, 60 (2008) 338.

[4] S. R. Elliott and J. Engel, J. Phys. G 30 (2004) R183;
Y. Zdesenko, Review of Modern Physics 74 (2002) 663.

[5] E. Fiorini et al., Phys. Lett. B 25 (1967) 602.

[6] F. T. Avignone III et al., Phys. Rev. Lett. 50 (1983) 721.

[7] J. J. Simpson et al., Phys. Rev. Lett. 53 (1984) 141.

[8] E. Bellotti et al., Phys. Lett. B 146 (1984) 450.

[9] H. Ejiri et al., Nucl. Phys. A448 (1986) 271.

[10] D. Caldwell, J. Phys. G: Nucl. Part. Phys. 17 (1991) S137.

[11] P. Fisher et al., Phys. Lett. B 218 (1989) 257.

[12] A. Morales et al., J. Phys. G: Nucl. Part. Phys. 17 (1991) S211,
J. Busto et al., Nucl. Phys. A513 (1990) 291.

[13] A. A. Vasenko et al., Mod. Phys. Lett. A 5 (1990) 1299;
I. V. Kirpichnikov, Preprint ITEP 91-91 (1991).

[14] H. V. Klapdor-Kleingrothaus, A. Dietz, I. V. Krivosheina and O. Chkvorets, Nucl. Instr. Meth. A 522 (2004) 371.

[15] H. V. Klapdor-Kleingrothaus, I. V. Krivosheina, A. Dietz and O. Chkvorets, Phys. Lett. B 586 (2004) 198.

[16] C. E. Aalseth et al., Phys. Rev. D 65 (2002) 092007.

[17] J. Schechter and J. W. F. Valle, Phys. Rev. D 25 (1982) 2951.

[18] G. Heusser, Ann. Rev. Nucl. Part. Sci. 45 (1995) 543.

[19] H. V. Klapdor-Kleingrothaus, J. Hellmig and M. Hirsch, GENIUS-Proposal, MPI-K, 1997.

[20] H. V. Klapdor-Kleingrothaus et al., Nucl. Instr. Meth. A 481 (2002) 149.

[21] Yu. G. Zdesenko, O. A. Ponkratenko, V. I. Tretyak, J. Phys. G27 (2001) 2129.

[22] R. Schuch et al., Advances in Quantum Chemistry 53 (2008) 67;
S. Rahaman et al., Phys. Lett. B 662 (2008) 111.

[23] H. V. Klapdor-Kleingrothaus, Proposal, MPI-1987-V17, September 1987.

[24] H. V. Klapdor-Kleingrothaus, O. Chkvorets, I. V. Krivosheina, C. Tomei, Nucl. Instr. Meth. A 511 (2003) 335.

[25] M. Günther et al., Phys. Rev. D 55 (1997) 54.

[26] H. V. Klapdor-Kleingrothaus et al., Eur. Phys. J. A 12 (2001) 147, hep-ph/0103062.

[27] Ch. Dörr, H. V. Klapdor-Kleingrothaus, Nucl. Instr. Meth. A 513 (2003) 596.

[28] L. P. Ekström and R. B. Firestone, WWW Table of Radioactive Isotopes, database version 2/28/99 from URL http://ie.lbl.gov/toi/index.htm.

[29] J. Echternach, Dipl. Thesis, Univ. Heidelberg, 1991 (unpublished).

[30] K. Zuber, Dissertation, 1992, Univ. Heidelberg.

[31] A. Müller, Dissertation, 1993, Univ. Heidelberg.

[32] B. Maier, Dissertation, November 1995, MPI-Heidelberg.

[33] F. Petry, Dissertation, November 1995, MPI-Heidelberg.

[34] J. Hellmig, Dissertation, November 1996, MPI-Heidelberg.

[35] A. Dietz, Dissertation, June 2003, MPI-Heidelberg;
A. Dietz, Dipl. Thesis, Univ. Heidelberg, 2000 (unpublished).

[36] Ch. Dörr, Dipl. Thesis, Univ. Heidelberg, 2002 (unpublished).

[37] A. Staudt et al., Eur. Lett. 13 (1990) 31;
K. Muto et al., Z. Phys A 334 (1989) 184.

[38] F. Šimkovic et al., Phys. Rev. C77 (2008) 045503.

[39] G. F. Knoll, "Radiation Detection and Measurement", second ed. 1989, John Wiley & Sons.

[40] G. Gilmore, J. D. Hemingway, "Practical Gamma-Ray Spectrometry", 1995, John Wiley & Sons.

[41] D. W. Scott, Biometrika, 66 (1979) 605.

[42] O. Helene, M. Moralles, Nucl. Instr. Meth. A 378 (1996) 624.

[43] V. I. Tretyak, Preprint KINR-90-35, Kiev (1990) 23.

[44] W. H. Press et al., Numerical Recipes in C, 2ed., Cambridge University Press.

[45] Ph. R. Bevington, D. K. Robinson, "Data Reduction and Error Analysis for the Physical Sciences", (1992), McGraw-Hill, Inc., New York, second ed., 328 p.

[46] D. E Groom et al., Particle Data Group, Eur. Phys. J. C 15 (2000) 1.

[47] G. J. Feldman, R.D. Cousins, Phys. Rev. D 57 (1998) 3873.

[48] J. A. Aguilar-Saavedra, Comp. Phys. Comm. 130 (2000) 190.

[49] http://www.mathworks.com

[50] A. M. Bakalyarov et al. (Moscow group of the HEIDELBERG-MOSCOW collaboration), hep-ex/0309016.

[51] T. Kihm et al., Nucl. Instr. Meth. B 498 (2003) 334.

[52] H. V. Klapdor-Kleingrothaus, O. Chkvorets, I. Krivosheina, H. Strecker, C. Tomei, Nucl. Instr. Meth. A 511 (2003) 341.

[53] H. V. Klapdor-Kleingrothaus, C. Tomei, I. Krivosheina, O. Chkvorets, Nucl. Instr. Meth. A 530 (2004) 410.

[54] H. V. Klapdor-Kleingrothaus et al., Nucl. Instr. Meth. A 566 (2006) 472.

[55] I. V. Krivosheina, Phys. Scripta, T127 (2006) 52.

[56] C. Tomei, Dissertation, L'Aquila University, 2004.

[57] A. Strumia, F. Vissani, arXiv:hep-ph/0606054 (2006).

[58] P. Eulgem, ORTEC AMETEC GmbH, private communication, 2008.

[59] B. Freudiger (BOREXINO Collaboration), Progress in Particle and Nuclear Physics, 48 (2002) 23.

[60] D.-M. Mei and A. Hime, arXiv:astro-ph/0512125.

[61] F. T. Avignone, 2005, private communication.

[62] H. Strecker, 2007, private communication.

[63] H. Miley et al., Nucl. Phys. B(Proc. Suppl.) 28A, (1992), 212.

[64] F. T. Avignone et al., Nucl. Phys. B(Proc. Suppl.) 28A, (1992), 280.

[65] I. Kirpichnikov et al., Nucl. Phys. 61 (1998) 1338;
GERDA Technical report, I. Kirpichnikov et al.

[66] E. Bellotti, Nucl. Instr. Meth. A 264, (1988), 1.

[67] E. Bellotti, M. Buraschi, E. Fiorini, and C. Liquori, New measurement of rock contamination and neutron activity in the Gran Sasso tunnel, Preprint INFN/TC-85/19, 1985.

[68] W. Hampel, 2007, private communication.

[69] A. Bassignani et al., Radiation Measurements 28, (1997), 609.

[70] H. Wulandari et al., Astroparticle Physics 22, (2004), 313.

[71] Pandola, L. et al., Monte Carlo evaluation of the muon-induced background in the GERDA double beta decay experiment, Nucl. Instr. Meth. A 570 (2007) 149.

[72] I. Barabanov et al., GERDA collaboration report (Milan, Nov. 2006).

[73] Letter of Intent to LNGS, see also: hep-ex/04040390, GERDA Proposal to LNGS(2004), http://www.mpi-hd.mpg.de/ge76/home.html.

[74] V. I. Tretyak, Yu. G. Zdesenko, Atomic Data and Nuclear Data Tables 80 (2002) 83.

[75] M. Hirsch, et al., Z. Phys. A 347 (1994) 151.

[76] H. Nakada, T. Sebe, K. Muto, Nucl. Phys. A 607 (1996) 235.

[77] F. Šimkovic, privat communication.

[78] V. Vergados, Nucl. Phys. B 218 (1983) 109.

[79] M. Doi and T. Kotani, Prog. Theor. Phys. 89 (1993) 139.

[80] A. S. Barabash, Phys. At. Nucl. 67 (2004) 438.

[81] Z. Sujkowski, S. Wycesh, Nucl. Instr. and Meth. B 235 (2005) 81;
Z. Sujkowski, S. Wycesh, Phys. Rev. C70:052501, (2004).

[82] M. Bauer et al., J. Phys.: Conf. Ser. 39 (2006) 362.

[83] D. W. O. Rogers, I. Kawrakow, J. P. Seuntjens, B. R. B. Walters, and E. Mainegra-Hing, NRC User Codes for EGSnrc, Technical Report PIRS-702(RevB), National Research Council of Canada, Ottawa, Canada, 2003.

[84] V. I. Tretyak, TEFF – program for efficiency calculation in the system source+screen+detector,(c)VIT, 1990, 1997.

[85] I. Bikit et al., Phys. Rev. C 67 (2003) 065801.

[86] P. Belli et al., Phys. Lett.,B 658 (2008) 193 H. Kiel et al., Nucl. Phys. A 723 (2003) 499;

F. A. Danevich et al., Nucl. Instr. Meth. A 544 (2005) 553;

H. J. Kim et al., KEK Proc. 2003-6, p.205.

[87] A. S. Barabash et al., hep-ex/0610046.

[88] Yu. M. Gavriljuk et al., Yadernaya Physika 69 (2006) 2169.

[89] H. Kiel et al., Nucl. Phys. A 723 (2003) 499;

F. A. Danevich et al., Phys. Rev. C 68 (2003) 035501;

V. B. Brudanin et al., Izvestiya RAN, ser. fiz. 70 (2006) 275 (in Russian);

I. Stekl et al., Czech. J. Phys. 56 (2006) 505.

[90] H. Kiel et al., Nucl. Phys. A 723 (2003) 499;

F. A. Danevich et al., Phys. Rev. C 68 (2003) 035501.

[91] H. J. Kim et al., KEK Proc. 2003-6, 205.

[92] H. Kiel et al., Nucl. Phys. A 723 (2003) 499.

[93] R. Cerulli et al., Nucl. Instr. Meth. A 525 (2004) 535.

[94] P. Belli et al., Nucl. Instr. Meth. A 498 (2003) 352.

[95] F. A. Danevich et al., Nucl. Phys. A 717 (2003) 129.

[96] P. Peiffer et al., Nucl. Phys. B (Proc. Supp.) 143 (2005) 511.

[97] H. Simgen, GERDA Scientific and Technical Report, GSTR-06-020.

[98] O. Chkvorets, M. Barnabe Heider, K. Gusev, S. Schönert, GERDA Scientific and Technical Report, GSTR-06-019.